Winter 2007

Analysis of Ultraviolet Energy Distribution in UV Disinfection Systems Using Monte Carlo Ray -Trace method

Khoi Trung Nguyen
Old Dominion University

ANALYSIS OF ULTRAVIOLET ENERGY DISTRIBUTION IN UV DISINFECTION SYSTEMS USING MONTE CARLO RAY-TRACE METHOD

by

Khoi Trung Nguyen

B.S., Chemical Engineering, May 1989, Virginia Tech
B.S., Civil Engineering, May 1990, Virginia Tech
Master of Engineering, May 1995, Old Dominion University

A Thesis Submitted to the Faculty of
Old Dominion University in Partial Fulfillment of the
Requirements for the Degree of

DOCTOR OF PHILOSOPHY

ENVIRONMENTAL ENGINEERING

OLD DOMINION UNIVERSITY
December 2007

Approved by:

_____
Jaewan Yoon (Director)

_____
A. Osman Akan (Member)

_____
Sebastian Bawab (Member)

ABSTRACT

ANALYSIS OF ULTRAVIOLET ENERGY DISTRIBUTION IN UV DISINFECTION SYSTEMS USING MONTE CARLO RAY TRACE METHOD

Khoi Trung Nguyen
Old Dominion University, 2007
Director: Dr. Jaewan Yoon

Determination of fluence rate in ultraviolet (UV) disinfection systems is a crucial part in evaluating disinfection efficiency of the systems. A robust Monte Carlo Ray Trace (MCRT) method has been developed to determine fluence rates in three-dimensional space of the systems. This is a statistical sampling method in which millions of random light energy bundles are simulated from the axis of each UV lamp and traced through the system until their energies reduce to a minimum threshold level. Inherent phenomena including refraction through quartz tubes, specular reflection at quartz tube surfaces, and absorption by quartz and water, along with specific geometric factors of model systems, are addressed in the MCRT algorithm. Each time the MCRT algorithm is executed, millions of independent random samples are recorded. In spite of the inherent randomness of the simulation process, consistent fluence rates throughout the UV systems under study were obtained. Fluence rate data in the radial direction from modeled lamps compared well with observed experimental data obtained from two independent sources and with results from the Point Source Summation model. Based on data obtained from the MCRT simulations for modeled UV systems with multiple rows of low pressure UV lamps, fluence rates in the space between lamps located inside the lamp bank are significantly higher than those in space located outside the lamp bank and

along channel walls. This is primarily due to the energy contributions of surrounding lamps. The results also suggest that the effects of reflections from quartz tube surfaces and changes in lamp spacing to the distribution of fluence rates in the systems under study are insignificant, primarily due to the fact that fluence rates of each individual lamp drop significantly at the radial distance beyond a few centimeters from the quartz tube surface closer to the surface

Research Committee Members: Dr. A. Osman Akan
Dr. Sebastian Bawab

This dissertation is dedicated to:

My beloved wife, Van T. Thanh Dinh,

My beloved son, Francis Quang-Minh Nguyen, and

My beloved daughter, Felicia Van-Thao Nguyen.

ACKNOWLEDGMENTS

I would like to express my greatful appreciation to my advisor, Dr. Jaewan Yoon, for his support, encouragement, and invaluable guidance throughout this research. This research would not have been completed without his support.

I wish to specially thank Dr. A. Osman Akan and Dr. Sebastian Bawab for serving in my research committee and providing me invaluable comments, guidance, and support for the completion of this research. I would like to thank Dr. Surendra Tiwari for previously serving in my research committee. Even though he did not serve in the last stage of this research because of his illnesses, his invaluable guidance and support were important to this work.

I would like to thank Dr. Gary Schafran, Dr. Mujde-Erten Unal, Dr. Isao Ishibashi, Dr. Duc Nguyen, and Dr. David Basco with the Department of Civil and Environmental Engineering at Old Dominion University for their guidance, instructions, and support during this research process.

I would like to thank Dr. James R. Bolton with Bolton Photosciences Inc. and Dr. Michael R. Sasges with Trojan Technologies Inc. for providing experimental data used in this study. I would like to thank John Nehring for his support during the last stage of this work.

I would like to give thanks to my parents, and special thanks my wife, Van, and my children, Francis and Felicia for their constant encouragement, supports, prayers, and patience during this prolonged study. My wife made it possible for me to complete this work.

Last, but not least, I would like to thank my Heavenly Father for making my dream come true.

TABLE OF CONTENTS

Page

CHAPTER

LIST OF TABLES

LIST OF FIGURES

CHAPTER 1

INTRODUCTION

1.1 OVERVIEW OF UV DISINFECTION SYSTEMS

Ultraviolet light (UV) has been used in disinfection of pharmaceutics, food, beverages, storm water, combined sewer overflows, wastewater effluent for reuse, and drinking water since the early 1900's, especially in Europe. In the United States, UV has been used to disinfect wastewater effluents in the secondary treatment process in the past few decades. The use of UV to disinfect drinking water has become increasingly popular only recently, due to demands for alternative disinfection methods to replace chlorine. These demands were in response to concerns about the formation of disinfection by-products (DBPs), many of which are suspected human carcinogens, from the use of chlorine as a chemical disinfectant (Hunter, 1998; Cairn and MacDougall, 1995)[1].

UV disinfection mechanism is based on the fact that the UV light emitted from lamps is absorbed by deoxyribonucleic acid (DNA) in microorganisms (bacteria and protozoan) and by either DNA or ribonucleic acid (RNA) in viruses. Consequent reactions within these elements of microorganisms and viruses prevent them from further reproduction. Nucleic acids are the most important UV absorbers in microorganisms in the UV range of 240 to 280 nm (Jagger, 1967). DNA is a nucleic acid polymer in a double-stranded helix linked together by a sequence of four constituent bases, consisting of adenine, cytosine, guanine, and thymine, that constitute the genetic code. These form "base pairs" (adenine with thymine and cytosine with guanine) held together by hydrogen

[1] Journal model found in the journal *Water Research* was used for documentation.

bonds. This is the "glue" that holds the two "strands" of DNA together. Of these four bases, thymine undergoes a unique photochemical reaction. The UV light absorption causes photochemical reactions to occur that form covalent dimmers from two adjacent thymines (in DNA) or uracils (in RNA). The dimmer formation disrupts the replication process of the microorganism so that the organism cannot reproduce, and thus cannot cause disease (Bolton, 1999).

There are several ultraviolet light classes based on their wavelength such as vacuum UV (with wavelength ranging from 100 to 200 nanometers (nm)), UVC (200 nm to 280 nm), UVB (280 nm to 315 nm), and UVA (315 nm to 400 nm). Among them, UVC is generally considered to be the germicidal range, with the most effective germicidal wavelength of 254 nm (Bolton, 1999).

In addition, four general types of UV lamps are generally used in water, wastewater, and air disinfection systems including low pressure (LP), medium pressure (MP), high pressure (HP), and pulsed UV. Low pressure lamps emit a high percentage of germicidal wavelengths (35 to more than 80 percent) whereas medium pressure lamps emit much lower percentages of germicidal wavelengths (10 to 15 percent) (Bolton, 2000). Pulsed UV lamps emit high intensity at the germicidal wavelength in a very short period of time. The majority of older UV systems have LP lamps. However, medium pressure lamps are becoming more popular due to the reduced number of lamps required per reactor and reduced head loss. The pulsed UV technology is recently developed and may have significant applications in the treatment of drinking water in the future (Wolfe, 1990).

UV reactors are generally designed for both open channel flows (common in wastewater systems with a rectangular cross-sectional area) and tubular flows (common in water systems). Flow rates of UV systems range from less than 1 million gallons per day (MGD) to more than 100 MGD. Each reactor contains anywhere from a few UV lamps to hundreds of lamps, depending on lamp orientation and types of lamps. Typical UV lamps have diameters of approximately 2.5 centimeters and lengths of more than 50 cm, and adjacent lamps are placed from a few centimeters to more than 10 cm apart (Bolton, 2000; Iranpour *et al.*, 1999).

The number of UV installations at water and wastewater treatment plants has increased steadily in the past few years. From 1984 through 1999, the number of wastewater treatment facilities with UV systems increased from a few to more than 500 in the United States, and over 1500 installations were completed at wastewater treatment facilities in North America. Many new UV installations at water and wastewater treatment plants are currently expected in the current decade (Qualls and Johnson, 1985; Hunter, 1998).

1.2 NEEDS FOR UV TREATMENTS AND RELATED STANDARDS

In December 1998, the United States Environmental Protection Agency (USEPA) published the Stages 1 and 2 Disinfectants/Disinfection By-products (D/DBP) Rule mandating that water treatment facilities where chemical disinfectants are used comply with new standards for D/DBP concentrations by 2001. In addition, the Surface Water Treatment Rule requires 99.9 percent removal of Giardia and 99.99 percent removal of viruses in treated water (Code of Federal Regulations, 40 CFR 141.600-141.629, 1998).

The standards for D/DBP are represented by Maximum Contaminant Levels (MCLs) for trihalomethanes (THMs), consisting of chloroform ($CHCl_3$), bromodichloromethane ($BrCHCl_2$), dibromochloromethane (Br_2CHCl), and bromoform ($CHBr_3$) and also haloacetic acids (HAAs) consisting of monochloroacetic acid, dichloroacetic acid, trichloroacetic acid, monoacetic acid, and dibromoacetic acid (Pontius and Diamond, 1999). To meet the new standards, it is necessary for water treatment facilities to use alternative chemical disinfectants including ozone (O_3), chloramines (NH_2Cl, $NHCl_2$), and chlorine dioxide (ClO_2) or to modify their treatment processes in minimizing formation of DBPs in drinking water to meet the D/DBP standards.

Several limitations associated with these alternative chemical applications for drinking water disinfection still exist. Ozone is known to form DBPs, including bromate and aldehydes, and the use of this chemical demands higher capital and operating costs compared to those associated with other treatment methods such as the use of chlorine. Chloramines have been known to form trihalomethanes, typicaly DBPs, under certain pH conditions, are largely ineffective against virus and protozoan cysts when used alone, and may promote nitrification within drinking water distribution systems. Meanwhile, chlorine dioxide (ClO_2) has been known to dissipate rapidly in water making it difficult to measure the required residual for compliance demonstration purposes. This chlorine dioxide disinfectant also has the potential to form chlorite and chlorate, which are also DBPs, and causes cat-urine like odors in the drinking water distribution systems if the disinfection treatment step is followed by free chlorine disinfectant (White, 1999).

Several water and wastewater treatment facilities have preferred UV to chemical disinfectants in the effort to minimize or eliminate DBP formation. The use of UV

technology eliminates the needs for chemical storage, results in substantial reduction in space requirements, and has relatively low operating costs, compared with those corresponding to chemical disinfection systems (Wicke and Coffey, 2000; EPA, 1999; Wolfe, 1990). Using UV also results in disinfection efficiency equivalent to chlorine disinfection (Oppenheimer *et al.*, 1997). Recent successes by Clancy *et al.* (1998) in using UV at cost-effective doses to disinfect *Cryptosporidium parvum* oocysts have reinforced and boosted interest in UV where *Cryptosporidium parvum* is a major pathogenous microbial species known to resist most chemical disinfectants. Such successes in UV disinfection of these oocysts and additional *Giardia muris* cysts, which are other challenging major pathogen associated with chemical disinfection, were subsequently reported by other investigators (Craik *et al.*, 2001; Danielson *et al.*, 2001; Hayes *et al.*, 2001). Thus, UV has clearly emerged as a very attractive and viable alternative disinfection technology for the drinking water treatment industry in terms of its effectiveness both in cost and efficiency.

The United States Environmental Protection Agency (EPA) has considered UV an allowed disinfection technology for future federal Safe Drinking Water Act (SDWA) regulations (Stage 2 Microbial and Disinfection Byproducts Rules) (Schmelling, 2000). In January 2006, the agency published UV dose requirements for target pathogens including Cryptosporidium, Giardia, and viruses for achieving up to 99.9 percent inactivation of *Cryptosporidium parvium* and *Giardia lamblia* and up to 99.99 percent inactivation of viruses (National Primary Drinking Water Regulations, 40 CFR 141.720(d)(1) (2006)). Most recently, the agency published the Ultraviolet Disinfection Guidance Manual for the Final Long Term 2 Enhanced Surface Water Treatment Rule in

November 2006 to provide technical guidance on the design and operations of UV disinfection systems to treat drinking water used by the public. Further, each state has established UV treatment standards that are equal to or more stringent than those of the federal regulations.

1.3 MOTIVATION AND OVERVIEW OF STUDY

There are different ways to determine UV dose, also known as fluence and defined as the energy level believed to be absorbed by microorganisms passing a flow system. This level corresponds to disinfection efficiency (for a specific type of microorganism) in disinfection systems when designing a UV disinfection system and monitoring compliance with UV treatment standards. Such determination can be based on testing (including lab-scale tests, pilot tests, and full-scale tests using surrogated chemicals or microorganisms); continuous monitoring (direct measurement of UV irradiance); and computational models.

Testing is usually time-consuming and expensive, and test results could be subject to uncertainties due to constant changes in water quality and other treatment processes in the treatment train. Continuous monitoring of fluence rates provides historical field data, but proper adjustments to the monitored data are necessary due to progressive fouling of quartz tubes and detector covers. In addition, sensors used in monitoring UV energies receive the energies through directions limited by the physical scopes of their lenses and apertures. Therefore, sensor data are not representative of the reality of UV systems, where UV energies at any location in the systems come from all directions. Limited space available for mounting sensors presents further limitations in using sensors in

obtaining UV energy data at any location throughput a UV systems. Accurate determination of UV dose remains a challenge to UV professionals due to the above limitations, coupled with uncertainties in hydrodynamic aspects of flow systems.

UV computational models, once verified, validated and properly calibrated, could potentially provide useful tools in the determination of UV dose and fluence rates (the latter term is defined as the energy level at a location from all directions). A well developed computational model could be used as a tool to confirm test results, explore alternative design scenarios such as those related to lamp arrangements, lamp aging, changes in water qualities, and other design and operational parameters.

Even though many computational models have been developed in the past few decades to estimate UV energy distribution in UV disinfection systems, many research gaps still exist. Phenomena inherent in a radiation system including reflection, absorption, scattering, remission, wavelength dependency, and randomness of light emission have not been addressed in most of these computational models. In particular, effects of reflection by quartz surfaces in multiple lamp systems have not been addressed. Further, because all of these models are deterministic, the random nature of light emitting, in direction and energy distribution, cannot be described in the models.

In this study, the Monte Carlo Ray-Trace (MCRT) method is developed using a probablistic approach in lieu of an analytical solution to a problem to obtain an outcome that may be expected to be the same as that of the analytical solution. The use of Monte Carlo (MC) methods was first documented in 1944 for the development of the atomic bomb during World War II and in several decades after that for other engineering applications, particularly in the field of radiation heat transfer (Modest, 1993; Siegel and

Howell, 2001; and Mahan, 2002). The Monte Carlo Ray-Trace method is believed to be robust and more advantageous than other numerical methods in radiation heat transfer analysis (Mahan, 2002). The usefulness of the MC method is recognized by professionals in UV disinfection; however, application of the MC method in determining fluence rate distributions in UV disinfection systems is not found in the available UV literature.

In using the MCRT method, radiation power of a UV lamp is uniformly divided into a large number of discrete light sources, each emitting a large number of discrete energy bundles. Each energy bundle is traced from its emission point through a series of reflections and refractions at quartz tubes until it is finally absorbed by a surface element or volume element in the system or exits the system. The MCRT method can be used to determine UV fluence rates in a full three-dimensional environment, taking into account the wavelength dependency of the UV distribution. Therefore, with a given discrete exposure time, estimated UV fluence rates can then be used to determine and optimize UV dose and the disinfection efficiency of the UV system of interest.

Details of the literature review and specific objectives of this study are discussed in Chapter 2. A detailed description of the MCRT formulation including a discussion of applicable radiation theory and algorithm is provided in Chapter 3. Chapter 4 describes the implementation of the theories discussed in Chapter 3 in computer programming and simulations of the MCRT simulation methods. Chapter 5 describes the validation of the MCRT by comparing MCRT simulation results with measurement data from two independent sources along with comparison with a well recognized UV computational model. Chapter 6 presents MCRT simulation results in the study of effects of lamp

reflections and spacing on the distributions of fluence rates in multiple lamp systems with two to 25 low pressure lamps. Chapter 7 provides conclusions of this study and recommendations for future research related to determination of UV energy distributions. A printout of typical MCRT program outputs is provided in Appendix A.

CHAPTER 2

LITERATURE REVIEW, RESEACH NEEDS, AND OBJECTIVES

2.1 LITERATURE REVIEW

Increased popularity of UV treatments in the past two decades has resulted in numerous theoretical and practical studies. The primary objective of these studies has been to better determine UV doses, which was the main factor in demonstrating treatment efficiencies and compliance with regulatory standards. This important UV dose is expressed as a function of UV fluence rate and exposure time. The first independent variable for the function, UV fluence rates can be obtained by conducting biodosimetry testing (using a surrogate microorganism in a flow system), actinometry testing (using a surrogate chemical in a flow system), field measurements using UV sensors, or using computational methods. The second independent variable for the function, UV exposure time can be obtained by conducting a tracer test to determine residence time distributions or using a computational fluid dynamic model. Since this study concentrates on UV fluence distributions in UV systems by means of computational modeling, the literature review is focused on existing computational models in the UV literature.

One of the well-recognized UV fluence models is the Point Source Summation (PSS) model introduced by Jacob and Dranoff in 1970. This model is based on the Beer-Lambert absorption law that describes the absorption of light energy by the media through which light is transmitted (Jacob and Dranoff, 1970). Based on this model, the fluence rate received at a point in a reactor is expressed with the summation of irradiance contributed by all independent point sources that make up the lamp. In addition, irradiance from a point source is reduced with the inverse of the squared distance from

that source. This model has been used by different investigators in flow model development (Qualls and Johnson, 1985; Chiu *et al.*, 1999a; and Lynn *et al.*, 1999). However, the model does not account for the effects of the reflection and refraction that occur at multi-phased interfaces of air/quartz/water and air/water. Jacobs and Dranoff suggested that such effects would result in light rays to bend inward toward the reactor; thus, actual irradiance rates would be higher than those calculated by the model.

Contrary to the PSS model, Iraxoqui, Cerda, and Cassano (1973) developed the Extense Source (ES) model to estimate radiant energy emitted from a three-dimensional UV light source that is composed of elementary volume sources. Here, each elementary volume emits the same discrete amount of energy independent from other elementary volumes. The radiant energy flux received at a point in a reactor is the sum of light energy received from the number of volume sources described in the spherical coordinate system. Each volume source consists of a number of point sources. The ES model does not account for the effects of reflection/refraction and absorption of the quartz tube and water, assuming that the spectral distribution of lamp emissions also disregards such factors. According to the authors, the model tends to underestimate irradiance in the radial direction.

Severin *et al.* (1983) proposed the Infinite and Finite Line Source (ILS/FLS) emission models for estimating average light intensity within UV reactors. Both the ILS/FLS models assume that a lamp is a line source that consists of a series of point sources of equal size and intensity. The infinite line source model assumes that light is emitted from each point source in only the radial directions perpendicular to the lamp axis. The finite line source assumes that light is emitted spherically (i.e., in all

directions) from each point source; thus, some energy is assumed to be lost at the top and bottom of the reactor. The ILS and FLS models are primarily based on the Beer-Lambert absorption law for one-dimensional and three-dimensional cases, respectively.

Blatchley (1997) developed the Line Source Integration (LSI) model by integrating the Point Source Summation model over the entire length of a line source and consequently maximizing the number of point sources (n) to infinitive. Due to the increased number of point sources represented by the LSI model, the accuracy of this model is expected to be higher than that provided by the PSS model. However, there is an intrinsic uncertainty in this LSI model in predicted irradiance for the area closer to the source.

Bolton (2000) developed a model for calculating the average UV fluence rate for an annular reactor. This calculation method is primarily based on the multiple point source summation approximation and the Beer-Lambert absorption law. The model also takes into accounts the effects of reflection and refraction occurring at the air/quartz and quartz/water interfaces when a ray of light is transmitted through these interfaces. However, reflections from an adjacent quartz tube are not accounted for in this model.

Kowalski (2001) developed a UV model called the Ultraviolet Germicidal Irradiation (UVGI) model for disinfection of an air-flow system using a single lamp. The author used a radiation view factor (also called a configuration factor), which represents the fraction of diffuse radiation energy emitted by one surface that is absorbed by another surface, to determine the distribution of UV fluence rate in a square-shaped air flow system. Unlike the other fluence models described above, UV fluence rate determined by the UVGI model for any location in the system is the sum of energy directly emitted from

the lamp and that reflected by all surrounding surfaces. Accounting for reflected energy is believed to represent the UV distribution in a more realistic way. Determination of the view factor is relatively easy for simple geometry of the air-flow system being studied. However, for a multiple lamp system, this method is very difficult to apply.

Sasges et al. (2007) discussed a Lambertian model describing changes of irradiance along a horizontal circular arc with respect to a lamp mid-point. A comparison with other existing computational models including the Point Source Summation Model and Radial Model indicated that these models did not address such changes.

Table 2-1 provides a summary of the main characteristics of the irradiance models described in this section.

2.2 RESEARCH NEEDS

Based on the literature review, the absorption of UV energy by the medium in which UV light travels is addressed by most models. Combined effects of light reflection and refraction are addressed in the Bolton model. Phenomena including randomness of the light emitted and reflection of light by quartz surfaces surrounding a lamp in a multiple-lamp system have not been fully described in the current literature related to UV treatment. UV computational models that can statistically describe the random nature of radiation while addressing the other inherent phenomena including reflection, refraction, absorption, emitting/reemitting, scattering, and wavelength dependency would be useful in representing three-dimensional energy distribution in UV systems. A review of radiation literature indicated that the Monte Carlo Ray Trace method that has been widely recognized in the field of radiation heat transfer (Modest, 1993; Siegel and Howell 2001;

and Mahan 2002) and could potentially be applied in the field of UV radiation to obviate shortcomings in existing UV fluence models if robust modeling procedures are developed.

Table 2-1. Summary of Existing UV Computational Models

Model Characteristic	Irradiance Models (*)						
	PSS	ES	FLS/ILS	LSI	B	K	S
Based on Beer-Lambert's absorption law	X		X	X	X		X
Lamp as a line with point sources	X		X	X	X		X
Lamp as volume sources		X					
Light emitted in all directions and angles	X	X	X (FLS)	X	X	X	X
Light emitted in radial direction perpendicular to lamp axis			X (ILS)				
Receptors are points	X	X	X	X			X
Receptors are area or volume					X	X	
Reflection and refraction at air/quartz/water interface					X		
Reflection from surrounding surfaces						X	X

(*) PSS = Point Source Summation (Jacob and Dranoff, 1970); ES = Extense Source (Iraxoqui *et al, 1973.*); FLS = Finite Line Source (Severin, 1983); ILS = Infinite Line Source (by Severin, 1983); B = Bolton (Bolton, 2000); K = Kowalski (Kawalski, 2001); Sasges (Sasges et al., 2007)

"X" indicates applicability.

2.3 RESEARCH OBJECTIVES

The objective of this study is to develop robust statistical methods for rigorously determining UV energy distribution in three-dimensional space in UV disinfection systems, taking into account the basic inherent factors of a typical radiation system including random emission, reflection, refraction, and absorption by the water medium and quartz tubes. Specific objectives of the study are as follows:

1. Formulating UV system equations, computation methods and algorithms applying Monte Carlo Ray-Trace (MCRT) techniques and radiation principles for determination of fluence rates in a single lamp system and multiple lamp systems with low pressure lamps.
2. Developing computer programs in Fortran 90 for the proposed MCRT methods for the above systems. These programs can be executed on a personal computer and provide the flexibility for changing lamp size, spacing, and the number of lamps with minimum effort.
3. Applying and verifying the MCRT methods to study effects of various system conditions, especially those related to lamp spacing and reflections from surrounding quartz tubes and other surfaces, on UV fluence distribution within the systems.

CHAPTER 3

FORMULATION OF THE MCRT METHOD

3.1 OVERVIEW

The term Monte Carlo, named after the principality of Monte Carlo in the south of France, is generally referred to as a statistical approach in which sampling techniques for specific problems are carried out to produce outcomes to a certain degree of accuracy in lieu of analytical solutions, that may be impossible to obtain. A definition of the Monte Carlo method is provided by Herman Kahn (Siegel and Howell, 2001) as follows:

> "The expected score of a player in any reasonable game of change, however complicated, can in principle be estimated by averaging the results of a large number of plays of the game. Such estimation can be rendered more efficient by various devices which replace the game with another known to have the same expected score. The new game may lead to a more efficient estimate by being less erratic, that is, having a score of lower variance, or by being cheaper to play with the equipment at hand. There are obviously many problems about probability that can be viewed as problems of calculating the expected score of a game. Still more, there are problems that do not concern probability but are nonetheless equivalent for some purposes to calculation of an expected score. The Monte Carlo method refers simply to the exploitation of these remarks."

Following the above definition, Siegel and Howell (2001) suggest that what must be done for a specific problem is to set up a game or model that has the same behavior, and

is therefore expected to produce the same outcome as the physical problem that the model simulates, make the games as simple and fast to play as possible; use any available methods to reduce the variance of the average outcome of the game, then play the game many times and find the average outcome.

Problems in UV radiation distribution are particularly well suited to solution by a Monte Carlo Ray-Trace (MCRT) technique. Energy travels in discrete bundles along a straight path before interacting with matters it comes across. Determination of UV fluence rates involves tracing the history of a statistically meaningful random sample of energy bundles (photons) from their points of emission (light source), through a series of reflections, to their points of absorption in a medium such as water or air. Physical constraints of the system and the laws of probability are used in determining a random sample that is directly related to the number of energy bundles emitted from a light source, the direction of emission and reflection of a bundle, and the absorption and re-emission of the bundle. Thus, the need to determine UV fluence rates and supplemental intrinsic difficulties in analytical solutions in determining UV fluence rates prompted development of the MCRT concept developed in this study.

The MCRT methods are developed to estimate fluence rate distribution in three-dimensional space of single- and multiple-lamp systems with lamps placed vertically or horizontally to water/wastewater and air distribution systems. The methods can be applied to systems with low pressure lamps that emit UV light mostly with the wavelength of 254 nm and potentially applied to the determination of medium pressure lamps that emit UV lights with wavelengths ranging from 185 nm to 400 nm.

The basic radiation theory used to develop the MCRT methods is presented in Section 3.2. Detailed description of the MCRT methods is provided in Section 3.3.

3.2 BASIC THEORY AND RAY TRACING APPROACH

Light energy is often referred to as the form of concentrated units of photons in quantum theory. Based on this theory, when an electron in an atom moves from one energy level to another, it emits or absorbs a corresponding amount of energy, called quantum, from the atom. The amount of energy (E) emitted or absorbed is associated with a frequency of light and is described as the factor of the Planck's constant (h = 6.6237 x 10^{-34} J.s) and frequency (γ), or $E = h\gamma$.

The energy can also be expressed in terms of wavelength as $E = hc/\lambda$ in which c is the speed of light (2.9979 x 10^{8} m/s) and λ is the wavelength. Wavelengths of the ultraviolet light range from 100 nm (nanometer) to 400 nm (this unit of wavelength is used throughput this report). This range of wavelengths is between that of X-rays (10^{-5} nm to 100 nm) and of visible light (400 nm to 700 nm). The UV wavelength of 254 nm is known to be the germicidal wavelength, at which disinfection is most effective.

The transmission of light is described as a "wave-like" phenomenon or a "ray-like" phenomenon. The wave description is based on electromagnetic theory developed by James Clerk Maxwell (1831-1879), in which the electric and magnetic fields are combined to establish electromagnetic energy that propagates as a wave at the speed of light. The wave nature of the transmission is represented by wave functions of the electromagnetic waves. A practical approach in describing transmission of light is to use ray, which represents the path followed by an energy bundle. The term "bundle" refers to

several parallel rays traveling together in the same direction. This term also implies the inclusion of a photon of different levels of energy as a function of wavelength λ. The ray approach is applicable when the wavelength of the radiation is short compared to the physical dimensions of the systems being studied (Mahan, 2002).

Objects such as quartz tubes, channel walls, and water surface in UV disinfection systems have curvatures that are much larger than the wavelength of a UV light. Therefore, using the ray description to describe light transmission in these systems is suitable. The basic radiation theoretical concepts related to the MCRT concept are discussed in the following sections.

3.2.1 Characterization of Emitting Sources

Light energy emitted from an UV lamp can be considered to originate from the lamp surface or axis. Figure 3-1 provides a simplified presentation of light bundles emitted from both locations. All existing UV models discussed in Chapter 2 use the center line emission approach. This approach is considered reasonable because the lamp emits energy in all directions, not just the hemispherical space above each element surface. Therefore, for computational purposes, the center line emission approach will be used in this study.

An emitting source could be a lamp or the element in the medium that emits light energy randomly in all directions. Each lamp is assumed to consist of a finite number of light-emitting point sources located along the lamp axis. These point sources are assumed to have equal emitting power and emit UV light independently and diffusely in all directions from the axis of the lamp. Let P_L be the rated radiant power of a lamp and

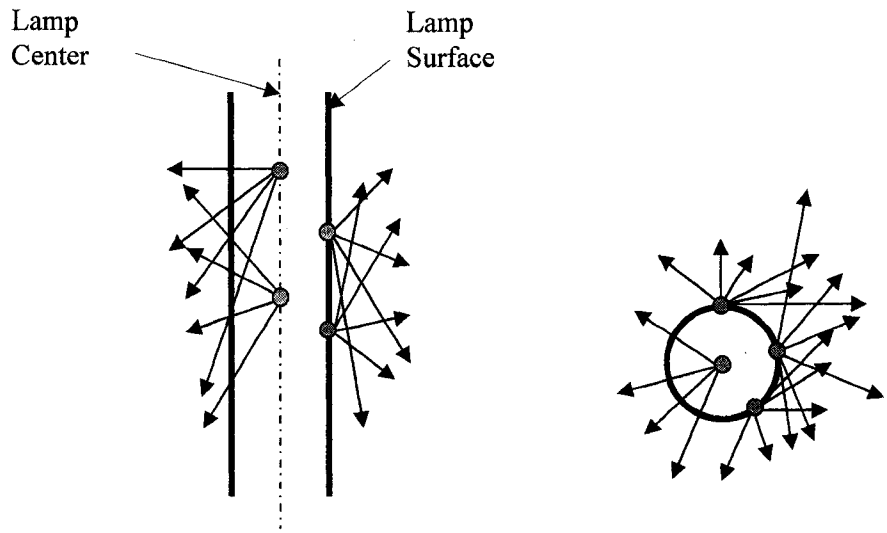

(a) Vertical View (a) Planar View

Figure 3-1. A Simplified Description of Light Bundles Emitted from Lamp Axis and Lamp Surface Elements

N_L be the total number of point sources, then the irradiance of each point source that emits light energy in all directions (i.e., 4π space) is defined by

$$E_i = \frac{P_L}{\pi r^2 N_L} \tag{3-1}$$

where the lamp power P_L is commonly expressed in watts or milliwatts (mW), and r is the radial distance from the point source to a point of interest in the 4π space in a non-absorbing medium. E_i is commonly expressed in mW/cm^2 or mJ/cm^2-s. In this study, the unit mW/cm^2 will be used.

For ray tracing purposes, a high number of energy bundles are randomly emitted from each point source. Each bundle carries an equal amount of energy from the point source given by

$$E_{Bi} = \frac{E_i}{n_i} \tag{3-2}$$

Where n_i is the number of bundles generated from each point source.

Intensity (I_i) is defined as the radiant energy of each point source passing through an area per unit of time, per unit of the projected area and per unit solid angle per unit wavelength (Howell and Siegel, 2001; Mahan, 2002) and is determined as

$$I = \frac{P_L}{4\pi N_L} \tag{3-3}$$

where the denominator represents the solid angle subtended by a sphere at a point source as the center of the sphere. The point source concept is commonly used in describing a UV emission source. Typical examples are the Point Source Summation model, Finite/Infinite Line Source Model, Line Source Integration model, and the model developed by Bolton. The intensity in a given direction is unchanged along that direction in a nonattenuating and nonemitting medium. However, the intensity changes when light transmits in an absorbing or attenuating medium.

The geometric factors in the definition of intensity and solid angle are illustrated in Figure 3-2. The solid angle is defined as the projected area of dA normal to the direction of light transmission divided by the squared distance from the light source to the area (Siegel and Howell, 2001).

Referring to Figure 3-2, the projected area of dA is $dA_p = dA\ cos\theta$ and the solid angle, ω, is (Modest, 1993):

$$\omega = \int_{A_p} \frac{dA_p}{S^2} = \int_{A} \frac{\cos\theta_0 dA}{S^2} \tag{3-4}$$

The differential form of the solid angle is

$$d\omega = \sin\theta d\theta d\phi \tag{3-5}$$

where φ is the azimuthal (circumferential) angle. The maximum value of the solid angle over a surface is 2π, resulting from integration of Equation 3-5 for φ ranging from 0 to 2π and θ ranging from 0 to $\pi/2$ in the hemispherical space above an emitting surface. The solid angle of 2π can be applied when an element surface of the lamp is considered to be a light source rather than a point source as mentioned above.

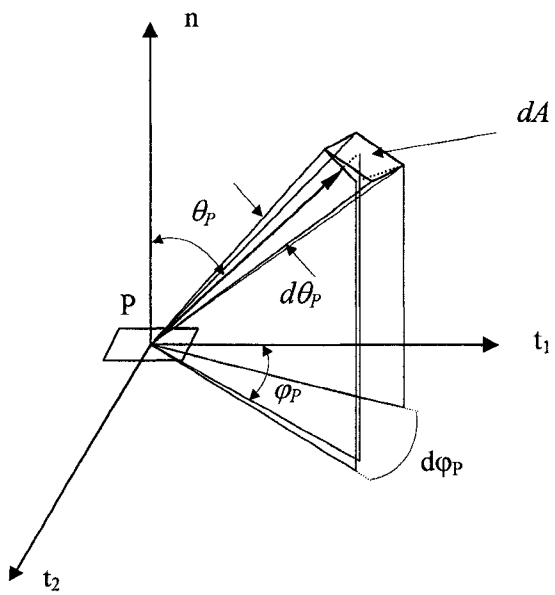

Figure3-2. Geometric Elements of Solid Angle

3.2.2 Reflection and Transmission of Light

Reflection of Light

Reflection of light is referred to as the change of direction of light transmission at the interface of two different media such that certain photons are reflected back to the medium in which the incident light travels. Refraction of light is referred to as the change of direction of light transmission relative to that of the incident bundle upon entering a new medium from the interface.

There are two general types of reflection, namely specular reflection and diffuse reflection. In specular reflection, a reflected ray is reflected at an angle equal to that of the incidence relative to the normal reflecting surface, and both rays lie in the same plane. This is a mirror-like reflection, and a specularly-reflecting surface is called an optically-smooth surface. This phenomenon is illustrated in Figure 3-2(a). In diffuse reflection, there are multiple reflected rays pointing in multiple directions unrelated to the direction of the incident bundle, and a diffusely-reflecting surface is usually associated with a "rough" surface. The diffuse reflection is illustrated in Figure 3-2(b). A real reflection surface may exhibit both modes of reflection with varying degrees of each.

A typical UV disinfection channel includes different interfaces of the following pairs of media: air and quartz (A-Q; the air medium represents a thin air layer between the lamp surface and the quartz tube); quartz and water (Q-W); quartz and ambient air ($Q\text{-}A_a$); water and ambient air (W-A, representing the free water surface); and water and channel wall ($W\text{-}W_w$). Reflections occurring at the A-Q interface, Q-W interface, and $Q\text{-}A_a$ interface can be assumed specular. This assumption implies that the quartz surfaces are not covered with fouling materials. The $W\text{-}A_a$ interface is subject to constant wave-

like motions due to flow, and reflection occurring at this interface is expected to be highly diffuse. The channel walls are assumed to absorb all incidence energy and provide no reflection at the W-W_w interface.

Light reflection in a specular mode is described by Fresnel's equation as follows (Modest, 1999):

$$\rho = \frac{1}{2}\left[\frac{\tan^2(\theta_1 - \theta_2)}{\tan^2(\theta_1 + \theta_2)} + \frac{\sin^2(\theta_1 - \theta_2)}{\sin^2(\theta_1 + \theta_2)}\right] \tag{3-6}$$

where ρ is the reflectivity, which is defined as the fraction of energy that is reflected. θ_1 and θ_2 are the angles of incidence and refraction, respectively, as illustrated in Figure 3-3. The relationship between angles θ_1 and θ_2 is described by Snell's law as follows:

$$n_1 \sin\theta_1 = n_2 \sin\theta_2 \tag{3-7}$$

where n_1 and n_2 are the refractive indices of media 1 (for incident bundle) and medium 2 (for refracted ray), respectively. A refractive index is the ratio of the velocity of light in vacuum to that in the medium under consideration. Referring again to Figure 3-4, the amount of light energy entering medium 2 by refraction at the interface is proportional to the factor of (1 - ρ).

Based on equations 3-6 and 3-7, the reflectivity (ρ) reaches zero when the angle of incidence relative to the normal interface is zero. On the other hand, when light travels from one medium to another medium with a smaller reflective index, as in the case of transmission from quartz to water, the angle of incidence may reach a critical value at or above which no light would be transmitted into the second medium. This phenomenon is called the total internal reflection. The internal total reflection angle of incidence, θ_t, is determined by

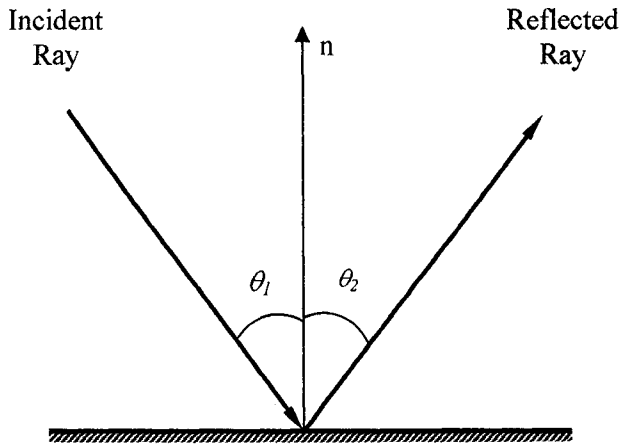

Optically Smooth Surface

(a) Specular Reflection

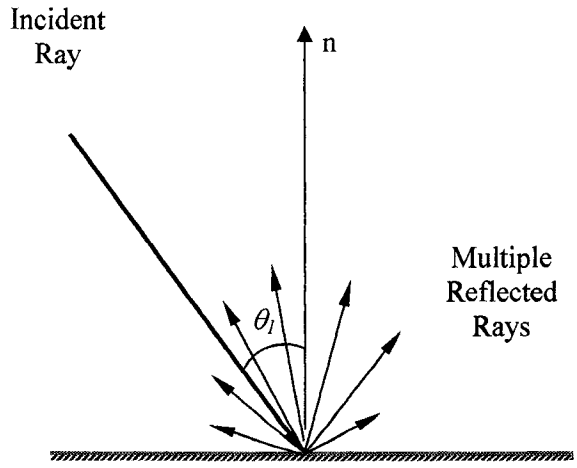

"Rough" Surface

(b) Diffuse Reflection

Figure 3-3. Two Modes of Reflection

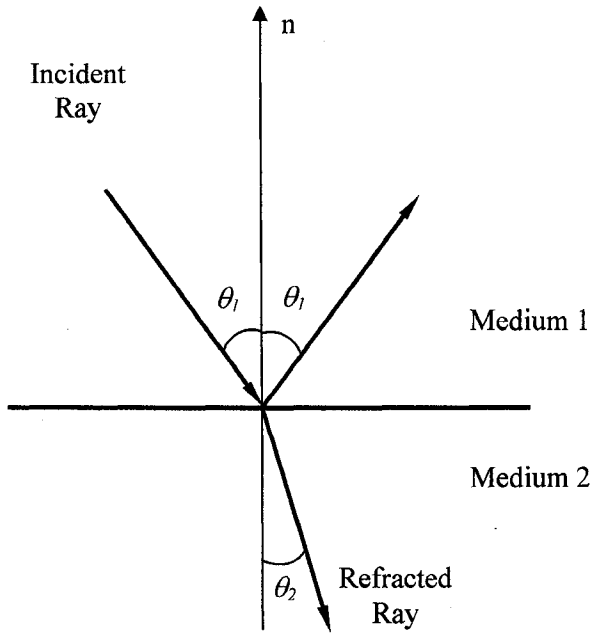

Figure 3-4. Specular Reflection and Refraction

$$\theta_{t,1-2} = \sin^{-1}\left(\frac{n_2}{n_1}\right) \tag{3-8}$$

Where n_2 and n_1 are the refractive indices of water and quartz, respectively, for an incident bundle approaching a quartz-water interface and those of air and water, respectively, for an incident bundle approaching a water-air interface.

Since the quartz tube absorbs UV energy, the absorption is accounted for in the following equation:

$$\tau = e^{-a_q d_Q} \tag{3-9}$$

where a_q is the absorption coefficient of quartz, and d_Q is the path length of the UV bundle traveling within the quartz. τ is also defined as the transmissivity for the path length in the quartz because, based on Kirchoff's law, the directional, spectral absortivity is equal to the directional, spectral emissivity. This law generally states that the amount of energy absorbed in a medium is equal to the amount of energy emitted from such medium.

Light Transfer in a Pane of Glass

When an incident bundle of energies approaches a pane of glass, a portion of the energies is reflected, and the other portion is transmitted and absorbed in the glass layer before being refracted outside the layer. These portions of energy are generally expressed as

$$A + R + T = 1 \tag{3-10}$$

in which *A, R, and T* represent the overall absorbance, reflectance, and transmittance, respectively. These terms are the functions of reflectivity and transmissivity defined in Equations 3-6 and 3-8, respectively. The above general equation is useful in modeling energy reflection and transfer through a layer of glass. Multiple reflections are expected through a pane of glass. The proportionality of specific light energies transferred portions as a result of the reflections are illustrated in Figure 3-5. As shown in this figure, the overall reflectance is provided by

$$R = \rho_{A-Q} + \rho_{Q-W}(1-\rho_{A-Q})^2\tau^2[1+\rho_{A-Q}\rho_{Q-W}\tau^2 + (\rho_{A-Q}\rho_{Q-W}\tau^2)^2 + ...] \tag{3-11}$$

The second and third terms in the bracket are significantly less than 1 and can be neglected, and the overall reflectance can be written as

$$R = \frac{\rho_{Q-W} + (1-2\rho_{A-Q})\rho_{Q-W}\tau^2}{1-\rho_{A-Q}\rho_{Q-W}\tau^2} \tag{3-12}$$

As shown in Figure 3-5, the overall transmittance and absorbance are written as

$$T = \frac{(1-\rho_{A-Q})(1-\rho_{Q-W})\tau}{1-\rho_{A-Q}\rho_{Q-W}\tau^2} \tag{3-13}$$

$$A = \frac{(1-\rho_{A-Q})(1+\rho_{Q-W})(1-\tau)}{1-\rho_{A-Q}\rho_{Q-W}\tau^2} \tag{3-14}$$

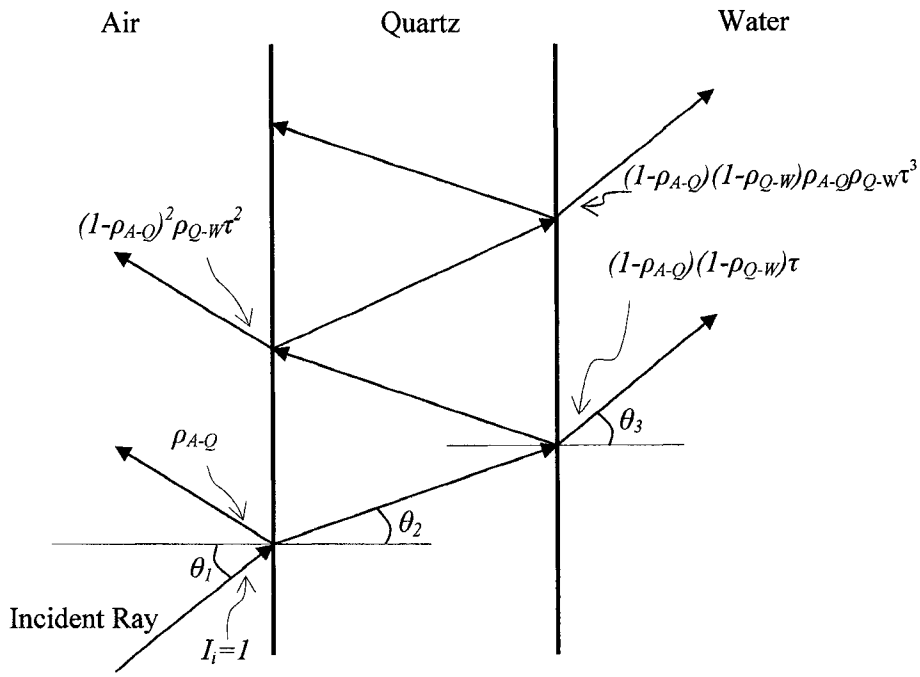

Figure 3-5. Light Energy Transfer Through a Glass Pane

Attenuation Of Light Energy in a Participating Medium

Light energy traveling through media such as quartz or water is absorbed and scattered (in different directions). Media that absorb light energy are commonly referred to as participating media. The combined effects of absorption and scattering cause the attenuation of light energy and are represented by the extinction coefficient K:

$$K(\lambda,T,P)=a(\lambda,T,P)+\sigma_s(\lambda,T,P) \tag{3-15}$$

where a and σ_s are the absorption coefficient and scattering coefficient, respectively. As shown in the above equation, these coefficients are theoretically dependent upon wavelength λ, temperature T, and pressure P. For the transmission of UV light through the quartz and water media, coefficient a is relatively independent of wavelength, and temperature and pressure have negligible effects. Light is potentially scattered when encountering small objects located in its pathway. In general, scattering effects in liquid water are considered very small compared to the absorbing effects in the medium (Modest, 1993). Light scattering effects in the air in the presence of particles such as ice or tiny water droplets are more pronounced than in pure liquid water.

The absorption coefficient appears in the law of absorption, which is commonly referred to as the Lambert's absorption law, as follows:

$$I_\lambda = I_{\lambda 0} e^{-aL} \tag{3-16}$$

where I_λ and $I_{\lambda 0}$ are the intensity at the light source and that at a point of interest, respectively, and a is the absorbing coefficient of the medium through which light transmits. The coefficient a can be replaced with the extinction coefficient κ when both absorbing effects and scattering effects are considered for a medium. The absorption

coefficient of water for UV light ranges linearly from 0.001 cm^{-2} at 400 nm to 0.08 cm^{-1} at 200 nm (Modest, 1993). This range may vary slightly depending upon water quality.

Light Energy Transfer In A Medium

Light energy in a participating medium or a surface is constantly absorbed and emitted by the medium, as a general principle of Kirchoff's law discussed in Section 3.2.3 (Reflection and Transmission of Light). The energy absorbed comes from surrounding light sources, including a lamp, a reflecting surface, or other volume elements in the medium. The absorption-emission phenomenon or a medium or surface element represents the reality of the light transferring process. When a bundle of light energy is absorbed in a volume element of a medium outside the lamp, the energy is immediately emitted from the same volume element to conserve energy for a medium in radiative equilibrium. In this regard, light energy could be distributed to locations blocked from a lamp by means of re-emission, scattering, and reflection from a surface in the enclosure.

3.2.3 General Approaches in Monte Carlo Ray Tracing

Effects of Optical Thickness on Ray Tracing Accuracies

Optical thickness, K_l, for a volume element is defined as the factor extinction coefficient, κ, and characteristic length of that volume, l. For the water medium, in which scattering effects are small and can be neglected, the absorption coefficient can be used in place of κ. The characteristic of a volume element, which is typically a cubic volume of water, is the length of each side.

When $K_l >> 1$, the path length l is considered optically thick, and when $K_l << 1$, the path length l is considered optically thin. If the optical thickness of a volume element is too thick, a smaller fraction of energy bundles generated from the element will be absorbed outside the volume element. This results in gross inefficiencies and inaccuracy of the MCRT simulations. If its optical thickness is too thin, a larger fraction of the energy bundle generated is expected be absorbed outside the volume element; thus, fewer samples from that volume can be collected, and the accuracy of the MCRT simulations will also decrease. To ensure accuracy of the simulations, the optical thickness should be roughly equal to 1 (Mahan, 2002).

Considering the UV absorption coefficient range of 0.001 to 0.08 cm^{-1} mentioned in Section 3.2.4, the corresponding characteristic length would be 1,000 cm and 12.5 cm. These characteristic lengths for volume elements appear to be too long for typical multi-lamp systems, in which lamp quartz tubes are normally separated by distances much closer than 12.5 cm. Selecting a characteristic length much less than 12.5 inches would compromise the accuracy of the MCRT modeling of re-emissions from volume elements. Therefore, for a UV system without space for reasonably sized volume elements for modeling purposes, re-emission from volume elements would be neglected in the modeling activities.

General MCRT Approaches

There are two general approaches used in Monte Carlo Ray-Tracing. The first approach involves the emission of energy bundles to an absorbing volume element in the medium, recording the number of bundles absorbed at the element as a distribution factor, re-emitting new energy bundle absorbed at that element, and tracing them until they exit the modeled system. In this approach, the emitting location on the lamp axis and the emitting direction of each bundle is randomly determined. The path length of each bundle within the participating medium before absorption by a volume element occurs is also randomly determined. The fluence rate at the volume element (E_j) can be calculated by the following equation for a one-lamp system:

$$I_j = \sum_{i}^{n} I_i D_{ij} \tag{3-17}$$

Where I_i is the irradiance of point source i from the lamp; D_{ij} is the distribution factor that represents the number of energy bundles emitted from light source i on the lamp and absorbed by the volume element j in the medium; n is the number of point sources on the lamp that contribute to the volume element.

When spectral emission (i.e., wavelength dependent emission) is considered, the distribution factor will be identified as D_{ijk} in which k represents the wavelength range. When more than one lamp is present, the fluence rate of the volume element is calculated by the following equation:

$$I_j = \sum_{l}^{L} \sum_{k}^{K} \sum_{i}^{n} I_{ikl} D_{jikl} \tag{3-18}$$

Where l represents the total number of lamps, and k represents the number of wavelength ranges. I_{ikl} represents the irradiance from point source element i on the lamp axis at

wavelength k on lamp l. The distribution factor D_{jikl} represents the portion of energy emitted from point source I_{ikl} from lamp l and point source i and absorbed at volume element I_j at wavelength k. The primary effort of an MCRT algorithm using the first approach is focused on accurately determining the distribution factor D_{ijkl} for each volume element in the system. This approach relies on the reasonable selection of the size of the volume element to accurately estimate distribution factors.

The second approach is the energy partitioning approach in which bundle energy is depleted along its path due to gradual attenuation. Each volume element through which a bundle travels depletes a certain amount of energy from the bundle, mostly by absorption. The cumulative amount of energy absorbed at each volume element will be updated as its fluence rate each time a bundle passes through the element. Correspondingly, calculation of a distribution factor for the purpose of determining the fluence rate is not necessary. Instead, the resulting fluence rates for a volume element can be used to estimate the corresponding distribution factors for the element. Further, the bundle is randomly generated from the light source, the emitting location and direction are randomly determined. However, unlike the first approach, the energy partitioning approach does not require determination of the path length of the bundle within the participating medium before absorption by a volume element occurs because the absorption is assumed to happen along the path of the bundle, beginning with the volume element in contact with the quartz tube of the lamp. In light of the discussion in Section 3.2.5, the energy partitioning approach is used in the MCRT modeling procedures described in detail in the following section.

In addition, the MCRT method calculates fluence rate at any volume element in a medium by summing the following two contributing components: a) the energy directly emitted from each lamp, and b) the energy reflected from the surrounding quartz tube surfaces and the water/air interface. If channel walls are made of reflective materials, the reflection from walls should also be included in the fluence rate calculations. An algorithm flowchart of MCRT methods developed in this study is given in Section 3.3 (The Monte Carlo Ray-Trace Method).

These two types of contributing energies are represented by two different bundles illustrated in Figure 3-6. As shown in this figure, Bundle 1 transmits energy directly from lamp 1 to a water volume element without undergoing any reflection. Bundle 2 is reflected from a quartz tube surface of another lamp (Lamp 2) before reaching the volume element. Each of the bundles is originally emitted from one or more point sources located on the axis of Lamp 1. Regardless of the number of reflections, the original point source of an energy bundle absorbed at the volume element will be recorded for fluence calculation purposes. The total fluence rate at a volume element is the summation of energies contributed from all bundles that hit the element. These bundles come from all surrounding lamps and reflecting interfaces by direct emission (as in the case of Bundle 1) or reflections (as in the case of Bundle 2).

3.3 THE MONTE CARLO RAY-TRACE METHOD

The MCRT method is developed in this study to determine the distribution of UV energy level in the three-dimensional space occupied by water/wastewater or air in a UV disinfection system. The ray tracing procedure first involves the random selection of the

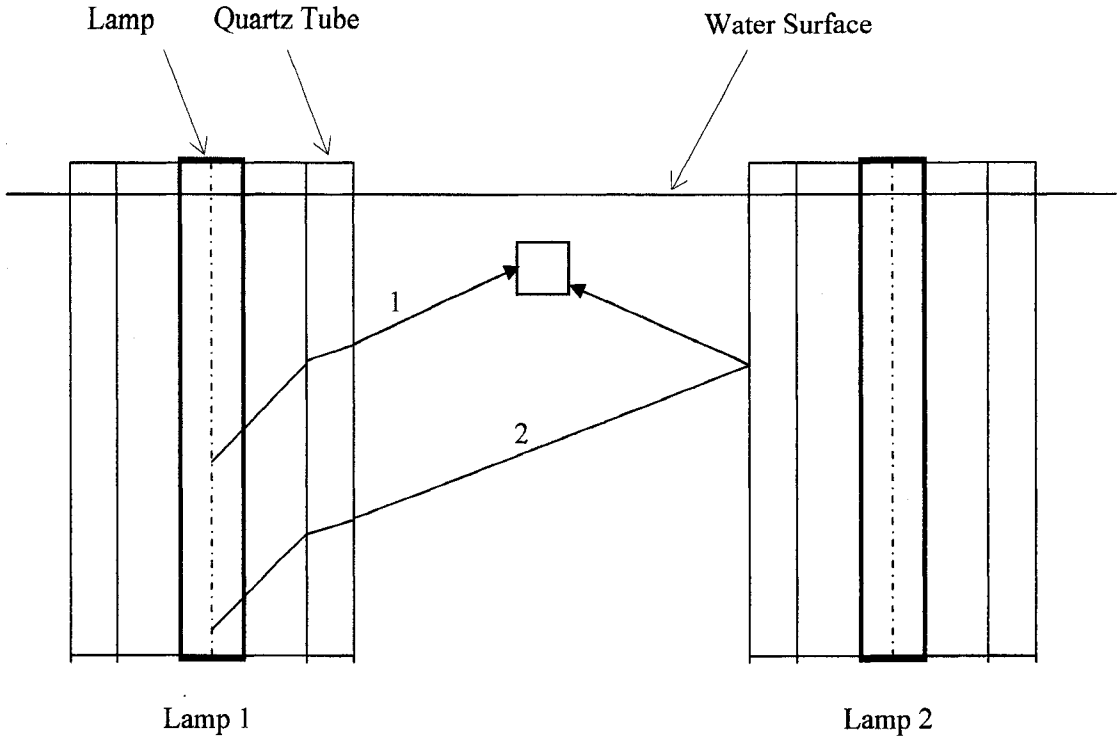

Figure 3-6 Representative Pathways of Contributing Bundles Emitted from a Lamp

emitting location and direction of an energy bundle from a point source on the lamp axis. The bundle is then traced through the refractions through the quartz tube to the quartz-water interface. From the quartz tube surface, the bundle is traced, based on its direction at that point, through the medium by determining whether it hits another quartz tube, water-air interface or a channel wall. The energy of the bundle absorbed by each volume element through which the bundle travels is recorded and updated as fluence rate at that location. The tracing of each bundle stops when its energy is absorbed below a threshold level considered to be negligible, and a new bundle from a point source on the lamp axis

is generated until the preset total numbers of bundles for each point source and the lamp are reached.

A logic block diagram outlining the above MCRT procedure is shown in Figure 3-7. Detailed discussion of each step labeled in the diagram is provided. The discussion is based on a vertical UV disinfection system configuration in contact with the water medium. However, the procedure and system equations presented in the discussion can be readily modified to describe fluence rate distribution in a horizontal water disinfection system configuration and an air disinfection system, as discussed in Chapter 4.

The entire algorithm is dependent upon the generation of random numbers in generating millions of random energy bundles each time the MCRT program is executed. In spite of the randomness of the energy emission, the transmission of the energies follow the principles of radiation and energy transfer such that when enough bundles of energy are generated, convergent results would demonstrate the distribution of energy in patterns that reflect the reality of the system. The Monte Carlo Ray-Trace concept discussed earlier in this section is simple in that repetitions of a process are primarily the main factor to achieve the statistically meaningful expect outcome. However, the application of this simple concept in determining fluence rates in a UV disinfection system requires the mathematical description of the geometry of the system in reference to the movements of each bundle through the system. Such description and related mathematical relationships are described in the following steps.

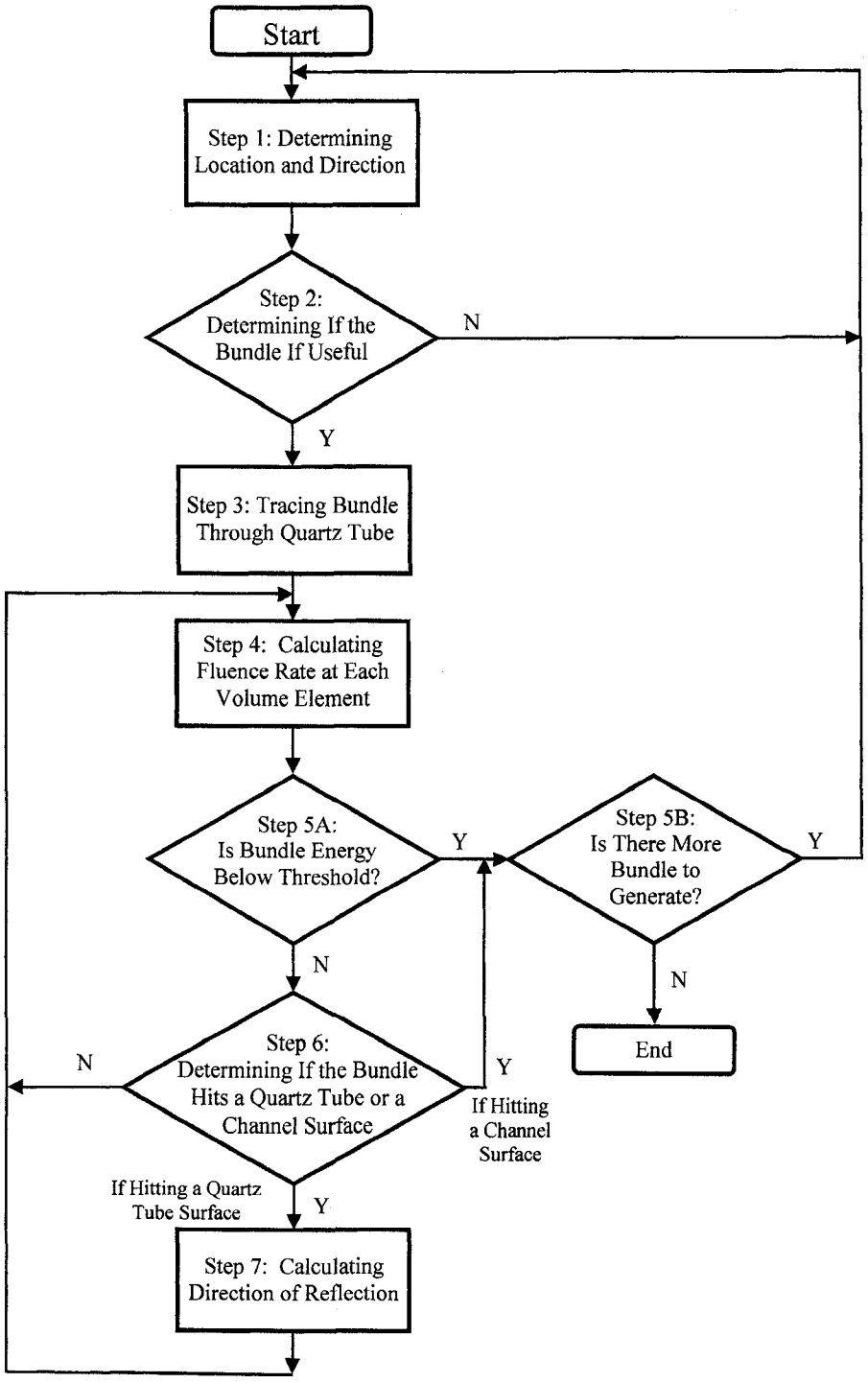

Figure 3-7. Simplified Block Diagram for the MCRT Simulation Procedure

3.3.1 Step 1: Determining Location and Direction of a New Bundle

Each lamp is assumed to consist of N_p component point sources located along the lamp axis. The modeled length of the lamp axis extends from the bottom of the channel to the water-air interface. The length of each subdivision containing the point source is given by

$$\Delta L = \frac{L}{N_p} \tag{3-19}$$

The global x and y coordinates of each point source are the same as those of the lamp axis, which are predetermined based on data of the modeled system. The z coordinate varies from zero at the bottom of the lamp to L at the top of the lamp, where L is the length of lamp.

Consider random emitting locations z on the lamp axis relative to the bottom of the channel. The frequency at which emission points originate from particular locations z on the lamp axis can be represented by an unknown frequency function $f(z)$ represented by a general frequency curve as shown in Figure 3-8. The probability density function that defines the average distribution of a position z can be defined by the following equation:

$$P(z) = \frac{f(z)}{\int_0^{Np} f(z)dz} \tag{3-20}$$

Where the denominator of the above equation represents the area under the frequency distribution curve shown in Figure 3-8. Np is the total number of point sources making up the lamp. Integrating the denominator of Equation 3-20 yields:

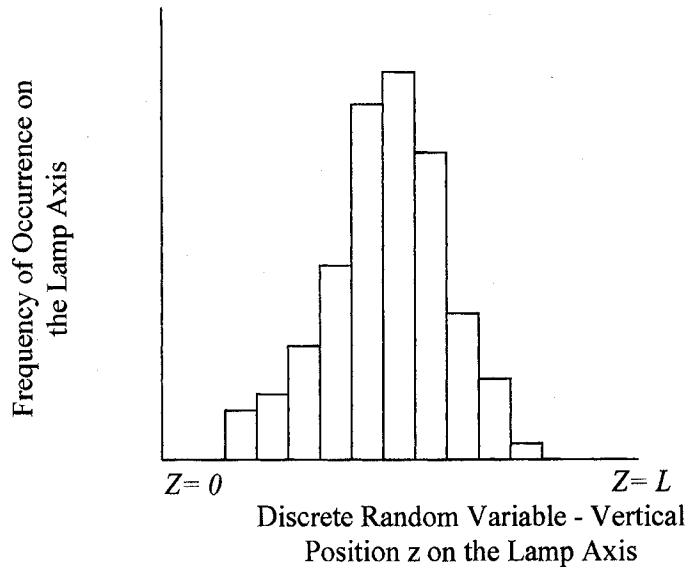

Figure 3-8. General Frequency Curve for Vertical Positions of Point Sources on the Lamp Axis

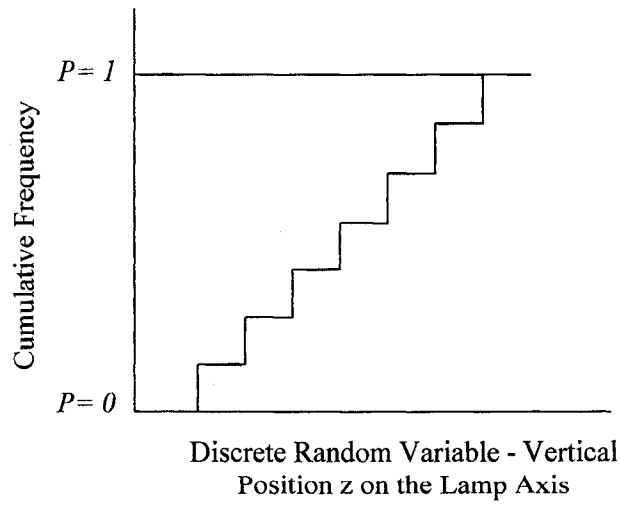

Figure 3-9. General Cumulative Distribution Curve for Vertical Positions of Point Sources on the Lamp Axis

$$P(z) = \frac{f(z)}{f(z)\sum_{1}^{Np} \Delta z} = \frac{1}{L} \tag{3-21}$$

The cumulative density distribution represented by the general curve shown in Figure 9 is given by

$$R(z) = \int_{o}^{z} P(z)dz = \frac{z}{L} \qquad 0 \le R(z) \le 1 \tag{3-22}$$

where *R(z)* is a random number that can be used to determine the value z.

From Equation 3-22, the emitting location can be estimated by

$$z = L \times R(z) \tag{3-23}$$

True random number generators do not exist in reality; rather, "random" numbers are computed using deterministic algorithms. Random numbers generated by a computer are actually pseudo-random numbers, and computer programs that generate such numbers are referred to as pseudo-random number generators. For programming and modeling purposes, mathematically generated numbers from International Mathematical and Statistical Library (IMSL) subroutines were used to generate pseudo-random numbers. Pseudo-random numbers used in MCRT simulations are assumed to be uniformly distributed between 0 and 1.

The direction of each new bundle emitted from a point source P is determined by the two following angles: cone angle θ_P and circumferential angle φ_P. The cone angle is the angle between the bundle and the vertical axis, which is also the lamp axis. The circumferential angle is the angle between the projection of the bundle on a reference plane and an arbitrarily chosen axis. These angles and the local x'-y'-z' system are illustrated in Figure 3-10. As shown in this figure, φ_P is the angle between the projection

of the x-y plane and the x' axis, measured in the direction from the positive x axis toward the positive y axis. The rest of the MCRT calculations rely on the values of angles θ_P and φ_P.

To determine the emitting direction of the bundle, two uniformly distributed random numbers $R_{\theta P}$ and $R_{\varphi P}$ are drawn. $R_{\theta P}$ represents the cumulative distribution function for angle θ_P, and $R_{\varphi P}$ represents the cumulative distribution function for angle φ_P. The functions are given by

$$R_{\theta P} = \frac{1}{2}\int_0^{\theta} \sin\theta d\theta = \frac{1}{2}(1-\cos\theta) \tag{3-24}$$

and

$$R_{\varphi} = \frac{\varphi}{2\pi} \tag{3-25}$$

From Equations 3-24 and 3-25, the cone angle and circumferential angle can be calculated by

$$\theta_P = \cos^{-1}(1-2R_{\theta P}) \tag{3-26}$$

$$\varphi_P = 2\pi R_{\varphi P} \tag{3-27}$$

The corresponding value of θ_P is between 0 and π and that of φ_P is between 0 and 2π.

An alternative way to randomly determine the emitting direction of a bundle is to generate three random numbers *R1*, *R2*, and *R3*. Subsequently, four new random numbers are calculated as follows using the three random numbers:

$$R1' = R1 + R1 - 1 \tag{3-28}$$

$$R2' = R2 + R2 - 1 \tag{3-29}$$

$$R3' = R3 + R3 - 1 \tag{3-30}$$

$$R4 = \sqrt{R1'^2 + R2'^2 + R3'^2} \tag{3-31}$$

The angles between the bundle and the x, y, and z axes are calculated by the following equations, respectively:

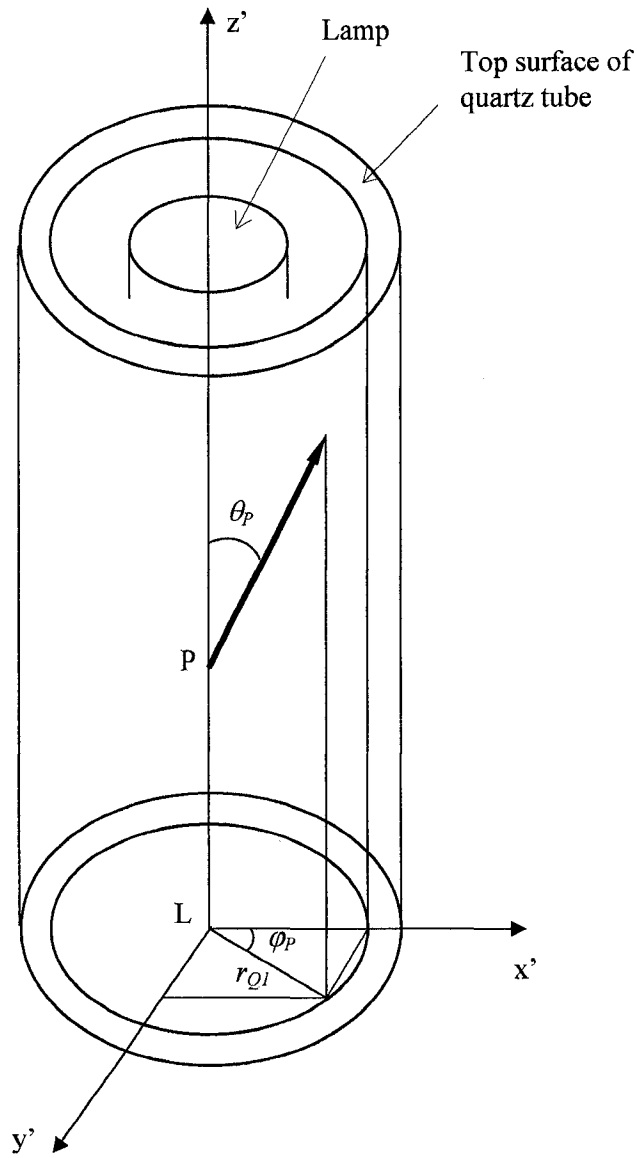

Figure 3-10. Angles Defining Emitting Direction of an Energy Bundle

$$\gamma = \cos^{-1}\left(\frac{R1'^2}{R4}\right) \tag{3-32}$$

$$\beta = \cos^{-1}\left(\frac{R2'^2}{R4}\right) \tag{3-33}$$

$$\theta = \cos^{-1}\left(\frac{R3'^2}{R4}\right) \tag{3-34}$$

Each time a new bundle is generated, the number of bundles for each point source (n_i) and the total number of bundles for the lamp (n_l) are updated. The numbers represent the number of useful simulated bundles, i.e., those that contribute energies to the medium. The useless bundles are determined in Step 2 and Step 3C. Both of the above numbers are used in Step 2A to determine if the MCRT simulation is complete. The total number of bundles generated from the lamp is the sum of the number of bundles generated from each point source.

The total number of bundles generated from a lamp is the factor of the number of point sources (N_p) and the number of bundles from each point source (N_B). Approximately 1000 point sources per lamp and 10,000 bundles for each surface emitting location were recommended by other investigators (Bolton, 2000; Mahan, 2002). In the current study, a convergence test is conducted for each modeled system as discussed in Chapter 4 to determine the number of bundles that need to be simulated to produce statistically meaningful samples. However, as illustrated in Chapter 4, the number of bundles needed to achieve stable results far exceeds the suggested numbers and is considered to be directly related to each specific system, its geometry, and related mathematical relationships built into the Monte Carlo application.

3.3.2 Step 2: Determining If the New Bundle Is Useful

This step is used to eliminate bundles that hit the top or bottom of the quartz tube because such bundles would not contribute energies to the medium. A useless bundle is confirmed by determining the angle it forms with the vertical axis.

Let θ' and θ" be the angle between a bundle that hits the outer edge of the top or bottom surface of the quartz tube, respectively. These angles can be determined by

$$\theta' = \tan^{-1}\left(\frac{r_{Q_1}}{L - z_P}\right) \tag{3-35}$$

$$\theta'' = \tan^{-1}\left(\frac{r_{Q_1}}{z_P}\right) \tag{3-36}$$

where r_{Q1} is the outer radius of the quartz tube, and z_P is the z coordinate of the point source. The geometric elements in Equations 3-31 and 3-32 are illustrated in 3- 11. Thus, any cone angle θ less than or equal to θ' (if the bundle is pointing upward) and θ" (if the bundle is point downward) would hit the top or bottom of the quartz tube and therefore be eliminated from ray tracing.

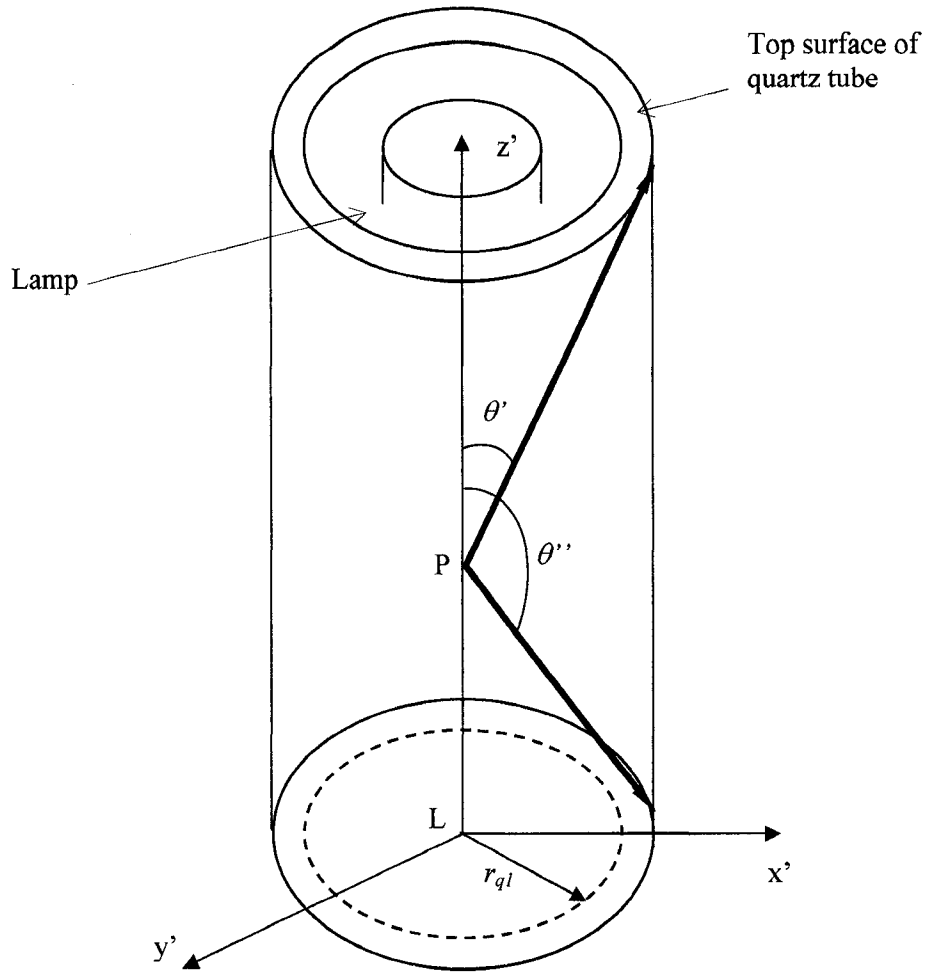

Figure 3-11. Limits of Useful Energy Bundles

Another case in which a bundle is determined to be useless is when the incidence angle of a bundle approaching the quartz-water interface reaches the internal reflection angle. Such determination is discussed in Step 3B. The number of useless bundles determined in the current step and Step 3B is deducted from the number of bundles generated from each corresponding point source and the total number of bundles generated from the lamp, both recorded in Step 1.

3.3.2 Step 3: Tracing the Bundle Through Quartz Tube

Step 3A: Determining the Intersections with Quartz Tube Surfaces

The cone angle (θ_P) and circumferential angle (φ_P) determined in Step 3A are useful in determining the first intersection point of the bundle with the inner surface of the quartz tube. This point is Point A in Figure 3-12(a). The x and y coordinates of Point A are determined by projecting the bundle on the local x'-y' plane, as shown in Figure 3-12(b). Thus, x_A and y_A are given by

$$x_A = x_L + r_{Q1}\cos\varphi_P \tag{3-37}$$

$$y_A = y_L - r_{Q1}\sin\varphi_P \tag{3-38}$$

where x_L and y_L are the global coordinates of the lamp axis, and r_L is the radius of the lamp. The z coordinate of point A is determined by

$$z_A = z_P + \frac{r_{Q1}}{\tan\theta} \tag{3-39}$$

where z_P is the z coordinate of the point source, and r_{QI} is the inner radius of the quartz tube. From the above coordinate data, the path length from Point P to Point A (directed segment PA) can be determined by

$$d_{PA} = \sqrt{(x_A - x_P)^2 + (y_A - y_P)^2 + (z_A - z_P)^2} \tag{3-40}$$

Where x_P, y_P, and z_P are the global coordinates of the point source. It is noted that x_p and y_p are the same as the x and y coordinates of the lamp, x_L and y_L, respectively. There is no need to determine the direction cosines of the bundle in this step, and it is assumed that UV energies of the bundle are not absorbed by the air gap between the lamp and the quartz tube.

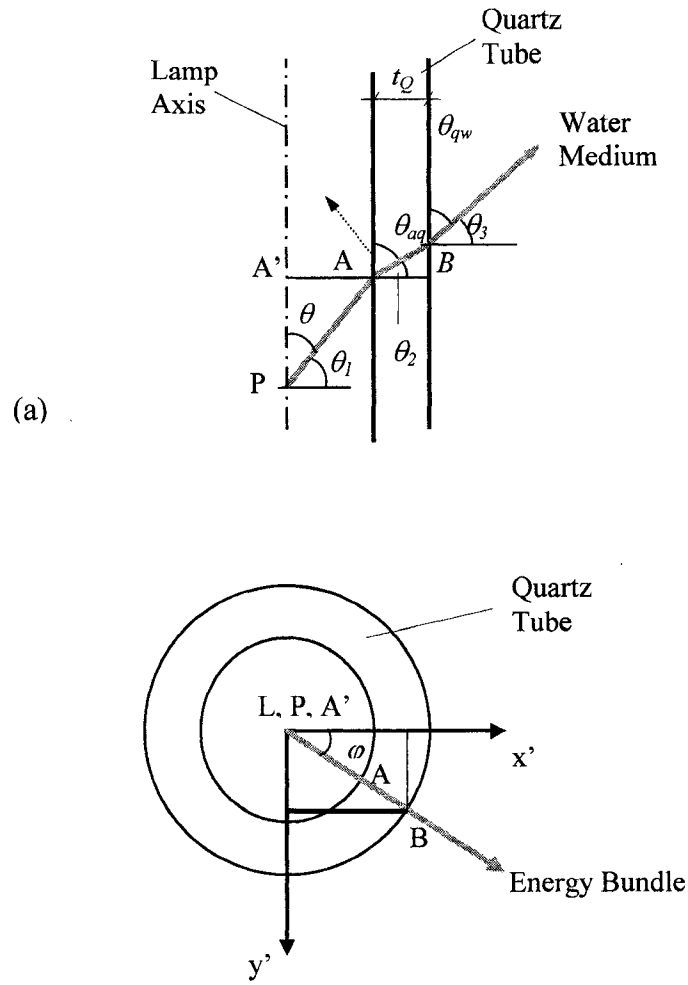

Figure 3-12. Geometric Elements for Determining Points of Intersection on Quartz Tube

Once the bundle hits the inner surface of the quartz tube, it produces a reflected bundle and a refracted bundle at that intersection point. The reflected bundle goes back to the lamp, and it will not be traced. The angles of refraction can be determined based on Snell's law, Equation 6. The following refraction indices of air, quartz, and water are useful for calculation purposes (Siegel and Howell, 2002):

$n_{ia} = 1.0003$ (at wavelength 589 nm)

n_{iq} = 1.52 – 1.68 (wavelengths 190 nm to 2,300 nm)

n_{iw} = 1.32 – 1.33 (wavelength 589 nm, temperature 15°C – 100°C)

Determining Cone Angles, Angles of Intersection, and Transmittance

In Step 3, the determination of cone angles θ_{aq} and θ_{qw} and angles of refraction θ_1, θ_2, and θ_3 (Figure 3-12(a)) is necessary for the calculation of the energy transmittance through the quartz tube and the coordinates of the intersection points on the quartz tube (Points A and B shown in Figure 3-12(b) and 3-12). The cone angles at the air-quartz interface and quart-water interface on the quartz tube are calculated based on one of the following cases:

For $\theta < 90^o$

$$\theta_{aq} = 90 - \sin^{-1}\left(\frac{r_{ia}}{r_{iq}} \times \sin(90-\theta)\right) \tag{3-40}$$

$$\theta_{qw} = 90 - \sin^{-1}\left(\frac{r_{iq}}{r_{iw}} \times \sin(90-\theta_{aq})\right) \tag{3-41}$$

For $\theta = 90^o$

$$\theta_{aq} = \theta_{qw} = \theta \tag{3-42}$$

For $\theta > 90^o$

$$\theta_{aq} = 90 + \sin^{-1}\left(\frac{r_{ia}}{r_{iq}} \times \sin(\theta-90)\right) \tag{3-40}$$

$$\theta_{qw} = 90 + \sin^{-1}\left(\frac{r_{iq}}{r_{iw}} \times \sin(\theta_{aq}-90)\right) \tag{3-41}$$

The corresponding angles of refraction are given by

For $\theta < 90^{o}$

$$\theta_1 = 90 - \theta \tag{3-42}$$

$$\theta_2 = 90 - \theta_{aq} \tag{3-43}$$

$$\theta_3 = 90 - \theta_{qw} \tag{3-44}$$

For $\theta = 90^{o}$

$$\theta_1 = \theta_2 = \theta_3 = \theta \tag{3-45}$$

For $\theta < 90^{o}$

$$\theta_1 = \theta - 90^{0} \tag{3-46}$$

$$\theta_2 = \theta_{aq} - 90^{0} \tag{3-47}$$

$$\theta_3 = \theta_{qw} - 90^{0} \tag{3-48}$$

If the incidence angle of the bundle going toward the quartz-water interface, which is equal to angle θ_1 determined in this step, is equal to or exceeds the total internal reflection angle θ_t discussed in Section 3.2.2, no refracted bundle into the water medium will be produced. If this is the case, the total number of simulated bundles from the corresponding point source and the total number of simulated bundles from the lamp are revised by deducting this useless bundle before generating a new bundle from the lamp axis. Using Snell's law (Equation 3-6, Section 3.2.2) and the refraction indices shown above, the total internal reflection angle applicable to incident bundles approaching the quartz-water interface from the quartz medium ($\theta_{t,Q\text{-}W}$) is given by

$$\theta_{t,q-w} = \sin^{-1}\left(\frac{n_{iw}}{n_{iq}}\right) = \sin^{-1}\left(\frac{1.32}{1.52}\right) = 61.04^{0} \tag{3-49}$$

The transmittance across the quartz tube, T_{Bi}, is calculated using Equation 3-13, and the reflectivity at each point of intersection on the quartz tube is given by Fresnell's equation (Equation 3-6). In using equation 3-13, it is necessary to calculate the transmissivity across the quartz tube given by Equation 3-9. The travel distance (d_2 in Figure 3-13) used in Equation 3-9 is given by

$$d_2 = \frac{t_q}{\cos\theta_2} \tag{3-50}$$

where t_q is the thickness of the quartz.

Determining Global Coordinates of the Points of Intersection

The coordinates of the air-quartz intersection point (Point A in Figure 3-13) are given by

$$x_A = x_c + \Delta x_A \tag{3-51}$$

$$y_A = y_c + \Delta y_A \tag{3-52}$$

$$z_A = z_P + \Delta z_A \tag{3-53}$$

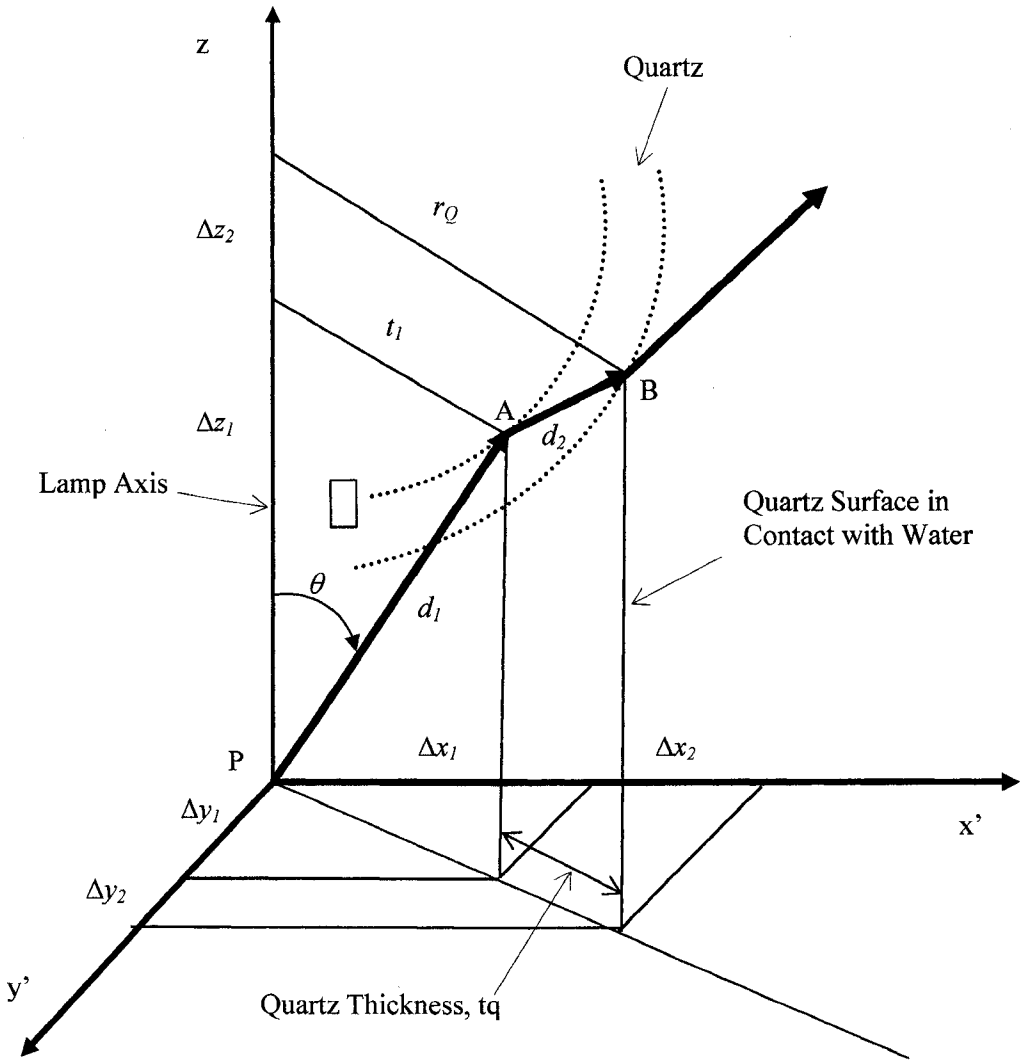

Figure 3-13. Additional Geometric Elements for Determining Points of Intersection on Quartz Tube

where

x_c, y_c = the x and y coordinates of the lamp axis

z_p = the vertical coordinate of point source P on the lamp axis

Δ_{xA}, Δ_{yA}, Δ_{zA} = changes in coordinates from point source P to Point A

Δ_{xA}, Δ_{yA}, Δ_{zA} are calculated using the following equations:

$$\Delta x_A = (r_l + t_a) \times \cos\varphi \tag{3-54}$$

$$\Delta y_A = (r_l + t_a) \times \sin\varphi \tag{3-55}$$

$$\Delta z_A = \frac{r_l + t_a}{\tan\theta} \tag{3-56}$$

where r_l = the radius of the lamp

t_a = the thickness of air layer between the lamp and the quartz surface

The coordinates of the air-quartz intersection point (Point A in Figure 3-13) are given by

$$x_B = x_A + \Delta x_B \tag{3-57}$$

$$y_B = y_A + \Delta y_B \tag{3-58}$$

$$z_B = z_P + \Delta z_A \tag{3-59}$$

Where x_A,y_A = the x and y coordinates of Point A

z_p = the vertical coordinate of Point A on the inner quartz surface

Δx_B, Δy_B, Δz_B = changes in coordinates from Point A to Point B

Δx_B, Δy_B, Δz_B are calculated using the following equations:

$$\Delta x_B = \frac{t_q}{r_l + t_a} \times \Delta x_A \tag{3-60}$$

$$\Delta y_B = \frac{t_q}{r_l + t_a} \times \Delta y_A \tag{3-61}$$

$$\Delta z_B = d_2 \cos\theta_{aq} \tag{3-62}$$

Step 3B: Determining Direction Cosines and Energy Level of the Bundle at the Quartz-Water Interface

Direction cosines are needed to determine the intersection of the bundles with other surfaces in the system, such as other quartz tubes, channel walls, and the water surface. Direction cosines of the bundle are defined as the cosines of the angles formed by the bundle and the global x, y, and z axis. The direction cosines of the bundle coming out from Point B relative to the x and y axes are determined by the following equations:

$$l_B = \cos\gamma_B = \frac{x_B - x_c}{d_3} \tag{3-63}$$

$$m_B = \cos\beta_B = \frac{y_B - y_c}{d_3} \tag{3-64}$$

Where angles γ_B, β_B, and distance d_3 are illustrated in Figure 3-14. The global coordinates of Point B are determined in Step 3A. The direction cosine of the bundle from Point B relative to the z axis (n_B) is the cosine of angle θ_{qw} calculated in Step 3A.

Calculating Energy Level of the Bundle at Point B

The UV energy level or fluence rate of the bundle at Point B on the quartz tube surface is calculated by the following equation:

$$E_{Qi} = E_{Bi} \times T_{Bi} \tag{3-65}$$

Where E_{Bi} = the fluence rate of each bundle, determined by Equation 3-2

T_{Bi} = the transmittance of UV energy carried by bundle from point source P to Point B, calculated in Step 3A.

This energy level represents the referenced level. Based on this level the tracing of a bundle may be terminated, as discussed in Step 5.

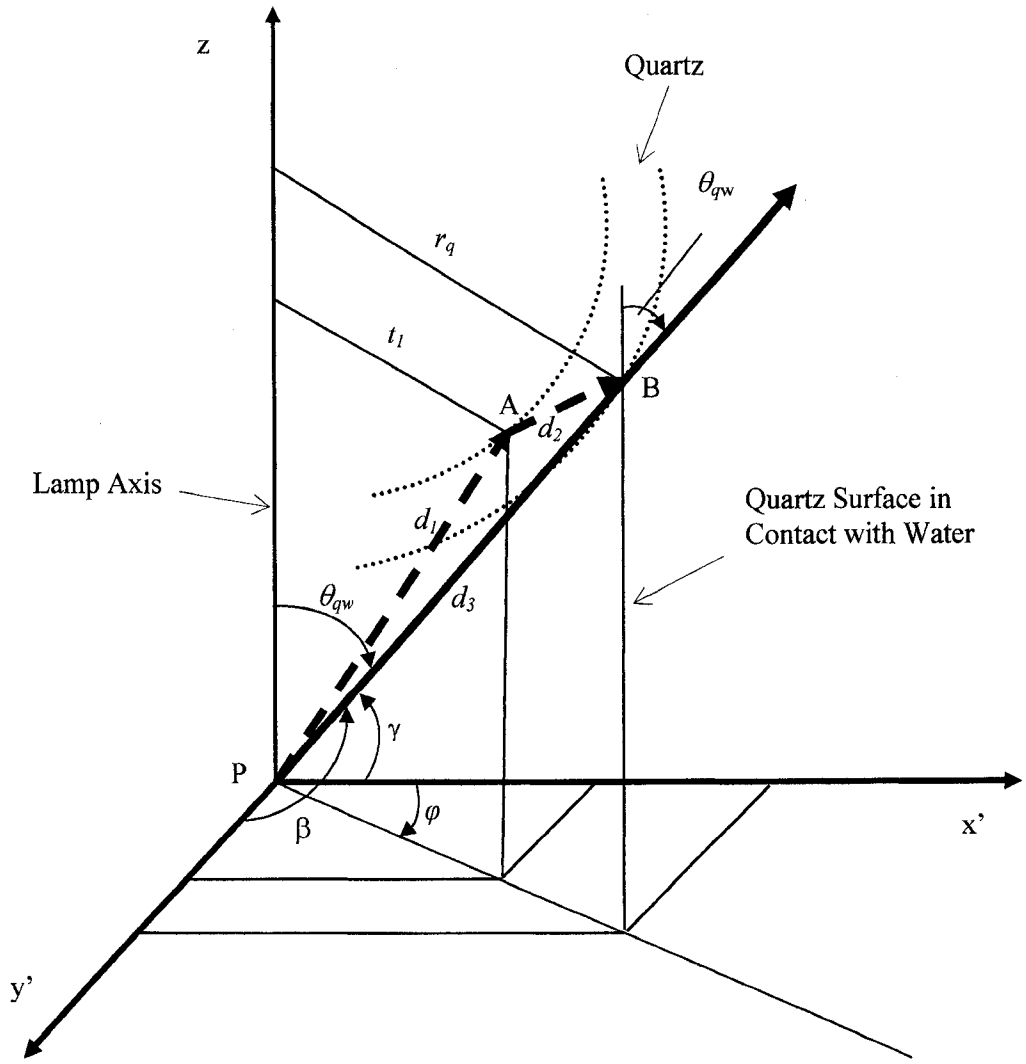

Figure 3-14. Direction Angles of Energy Bundle at Point B

3.3.4 Step 4: Calculating Fluence Rate for Each Volume Element

Each bundle emitting from the quartz tube surface brings with it UV energies that are absorbed by volume elements of water lying in its path. The water medium is discretized into cubic volumes of 1 cm^3 in size. This size is chosen for convenience because the units of measurement of UV fluence rate or irradiance are mW/cm^2 or

$mJ/s.cm^2$. The prior units are used throughout this report. Other volume element sizes can be used as long as they provide statistically meaningful sampling data.

The fluence rate of each volume element is the accumulated amount of energies absorbed at that location as a result of the transmission of energy bundles through that element. This fluence rate is determined by the following equation:

$$E_{j2} = \sum_i E_{ji} + E_{j1} \exp(-\kappa d_{1-2}) \tag{3-66}$$

Where the first term on the right hand side of the above equation is the cumulative fluence rate at the element prior to the passage of the new bundle. Subscript *j* represents the index of the volume element, and subscript *i* represents the index of the point source on the lamp axis from which the current bundle is generated, as shown in Figure 15(a). The second term on the right hand side of Equation 3-66 represents the new energy absorbed from the current energy bundle at that element. E_{j1} represents the bundle fluence rate at the preceding volume element before the bundle reaches volume element *j*; κ represents the extinction coefficient (or absorption coefficient if no scattering is considered in the modeling), and d_{1-2} is the path length of the bundle traveling from the point of entry into a volume element to the point of exit from the volume element, as shown in Figure 3-15(b).

Each face of the cubic volume element lies in the plane with one of the following six surface equations $x = x_i$, $x = x_{i+1}$, $y = y_j$, $y = y_{j+1}$, $z = z_k$, or $z = z_{k+1}$, as illustrated in Figure 3-15(c). Each cube is assigned a unique global address that corresponds to the above coordinates and cumulated fluence rate, as discussed in Chapter 4.

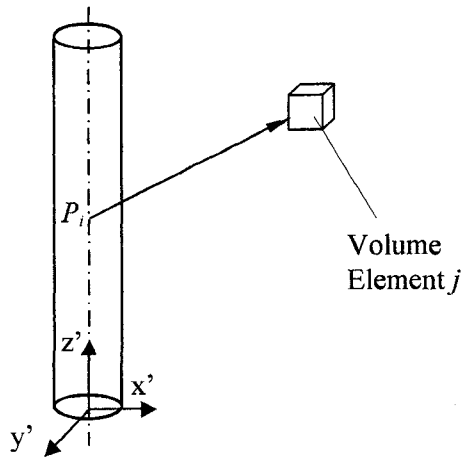

(a)

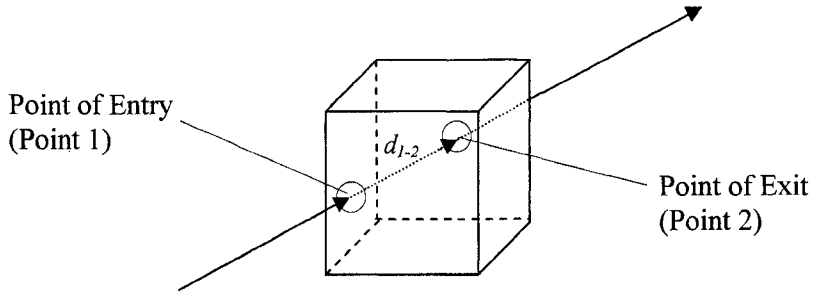

(b)

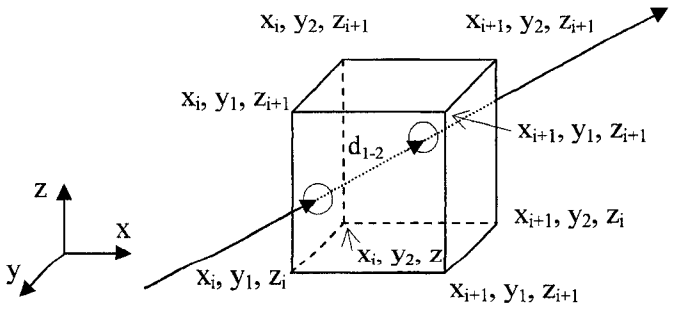

(c)

Figure 3-15. Geometric Elements of Volume Element

As a bundle leaves the quartz surface, it will hit one of the bounding surfaces of a volume element adjacent to the quartz tube and the succeeding volume element lying on the path of the bundle. As shown in Figure 3-15(c), the bounding faces that may potentially be hit by the bundle following its entry into the volume element are five faces other than the one containing the point of entry. However, if the direction cosines of the bundle are known, the number of bounding faces that may potentially be intersected by the bundle is reduced to three. Depending on values of the global direction angles γ, β, and θ, the bundle heads into one of eight directions listed in Table 3-1. Each direction listed in the table represents an octant in the three dimensional space.

Table 3-1. Eight Directions of Energy Bundles in Three-Dimensional

Case	Direction Angles					
	γ		β		Θ	
1	$< 90^{\circ}$		$< 90^{\circ}$		$< 90^{\circ}$	
2	$< 90^{\circ}$		$< 90^{\circ}$			$> 90^{\circ}$
3	$< 90^{\circ}$			$> 90^{\circ}$		$> 90^{\circ}$
4		$> 90^{\circ}$	$< 90^{\circ}$		$< 90^{\circ}$	
5		$> 90^{\circ}$		$> 90^{\circ}$	$< 90^{\circ}$	
6		$> 90^{\circ}$		$> 90^{\circ}$		$> 90^{\circ}$
7		$> 90^{\circ}$	$< 90^{\circ}$			$> 90^{\circ}$
8	$< 90^{\circ}$			$> 90^{\circ}$	$< 90^{\circ}$	

In each of the above cases, the bundle hits one of three bounding faces corresponding to the following three equations:

$$\frac{x_b - x_1}{\cos\gamma} = \frac{y_2 - y_1}{\cos\beta} = \frac{z_2 - z_1}{\cos\theta} \tag{3-67}$$

$$\frac{x_2 - x_1}{\cos\gamma} = \frac{y_b - y_1}{\cos\beta} = \frac{z_2 - z_1}{\cos\theta} \tag{3-68}$$

$$\frac{x_2 - x_1}{\cos\gamma} = \frac{y_2 - y_1}{\cos\beta} = \frac{z_b - z_1}{\cos\theta} \tag{3-69}$$

where subscripts 1 and 2 represent the point of entry and point of exit, respectively. The values x_b, y_b, and z_b represent the bounding surfaces of the volume element that are possibly intersected by the bundle. Each set of the above equations contains three sets of two equations and two unknown. Equation sets 3-67, 3-68, and 3-69 represent the cases in which the bundle intersects the bounding faces $x=x_b$, $y=y_b$, and $z=z_b$, respectively, and each set provides a set of candidate coordinates x_2, y_2, and z_2. The corresponding travel distance from the point of entry to the point of exit ($d_{1\text{-}2}$) can be calculated by the following equation:

$$d_{1-2} = \sqrt{(x_2 - x_1)^2 + (y_2 - y_1)^2 + (z_2 - z_1)^2} \tag{70}$$

The smallest values of $d_{1\text{-}2}$ corresponds to the correct intersection point. Once the minimum travel distance is determined, the updated fluence rate for the volume element is calculated and recorded using Equation 3-66.

For the volume element in contact with the quartz tube surface, such as those shown in Figure 3-16, the values of x_1, y_1, and z_1 are the same as those of the coordinates of Point B, determined in Step 3A. Specific equations for calculating the values of x_b, y_b,

z_b for the octants are listed in Table 3-2. The sizes of these volume elements in the x and y directions are less than 1 cm.

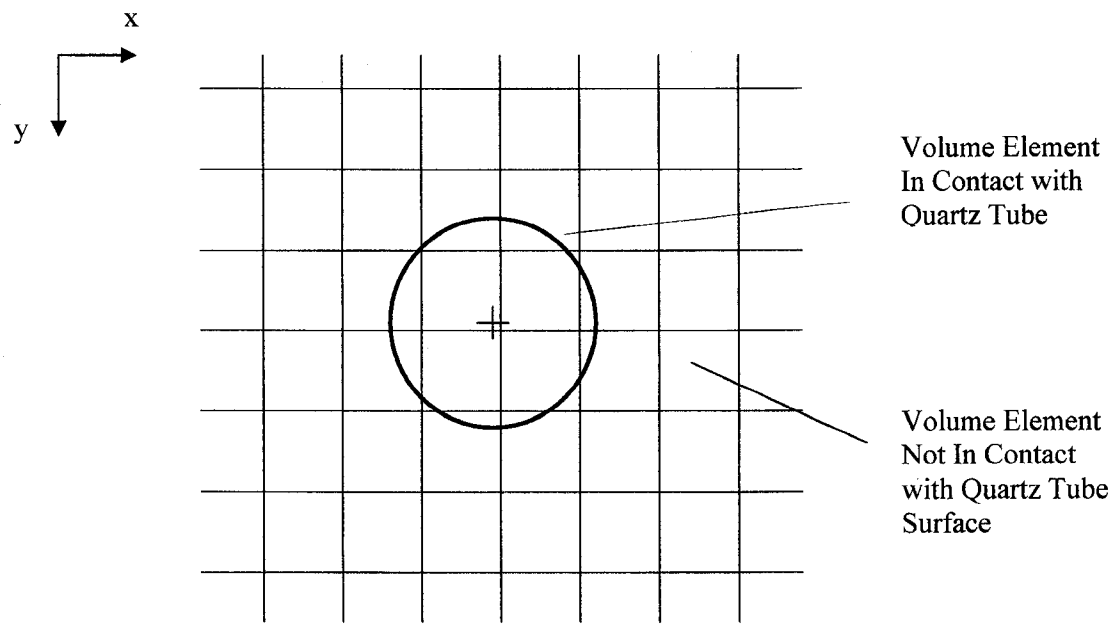

Figure 3-16. Volume Elements in the x-y Plane

For volume elements not in contact with the quartz surface, the bounding surface values are determined by the equations listed in Table 3-3. Three equations would be applicable. When a bounding face is confirmed to be intersected by the bundle (by determining the minimum travel distance, as discussed previously), the first equation corresponding to that face is applied for that face, and the second equations with function *INT()* are applied for the other two faces.

Table 3-2. Formulas for Calculating Bounding Surface Coordinates for Volume Elements In Contact with Quartz Surface

Case	Direction Angles			Equation for x_b, y_b, z_b		
	γ	β	θ	x_b	y_b	z_b
1	$< 90^\circ$	$< 90^\circ$	$< 90^\circ$	$INT(x_B) + 1$	$INT(y_B) + 1$	$INT(z_B) + 1$
2	$< 90^\circ$	$> 90^\circ$	$< 90^\circ$	$INT(x_B) + 1$	$INT(y_B)$	$INT(z_B) + 1$
3	$> 90^\circ$	$> 90^\circ$	$< 90^\circ$	$INT(x_B)$	$INT(y_B)$	$INT(z_B) + 1$
4	$< 90^\circ$	$< 90^\circ$	$> 90^\circ$	$INT(x_B) + 1$	$INT(y_B) + 1$	$INT(z_B)$
5	$> 90^\circ$	$< 90^\circ$	$> 90^\circ$	$INT(x_B)$	$INT(y_B) + 1$	$INT(z_B)$
6	$> 90^\circ$	$> 90^\circ$	$> 90^\circ$	$INT(x_B)$	$INT(y_B)$	$INT(z_B)$
7	$< 90^\circ$	$> 90^\circ$	$> 90^\circ$	$INT(x_B) + 1$	$INT(y_B)$	$INT(z_B)$
8	$> 90^\circ$	$< 90^\circ$	$< 90^\circ$	$INT(x_B)$	$INT(y_B) + 1$	$INT(z_B) + 1$

For example, referring to Figure 3-15(c), Case 2 in which $\gamma < 90^\circ$, $\beta > 90^\circ$, and $\theta < 90^\circ$ is applicable. The picture shows that the intersected bounding face at the point of exit is the face with $y=y_b$. Therefore, the equations to be used for calculating the coordinates of the bounding face for the traveling of the bundle in the succeeding volume element are $x_b=INT(x_2) + 1$, $y_b=y_2+1$, and $z_b=INT(z_2) + 1$. Function *INT()* is a Fortran function that returns an integer. In the succeeding volume element, x_2, y_2, and z_2 become x_1, y_1, and z_1, the coordinates of the point of entry at that volume element.

3.3.5 Step 5: Determining If the Bundle Energy Is Below the Threshold

This step is performed by comparing whether the energy of the current bundle is below a threshold at which the energy is too small to continue the tracing. This level can be considered to be 0.001 of the bundle energy when it first leaves the quartz tube surface (determined in Step 3B of Figure 3-7). This threshold number is arbitrarily chosen with

(determined in Step 3B of Figure 3-7). This threshold number is arbitrarily chosen with the assumption that neglected energy below the threshold would not significantly affect the simulation results. If the energy of the bundle is below the threshold, a new bundle will be randomly simulated from a new point source on the lamp axis. A new bundle will not be generated if the total number of bundles to be generated is reached.

Table 3-3. Formulas for Calculating Bounding Surface Coordinates for Volume Elements

Case	Direction Angles			Equation for x_b, y_b, z_b		
	γ	β	θ	x_b	y_b	z_b
1	< 90°	< 90°	< 90°	x_2+1 or INT(x_2)+1	y_2+1 or INT(y_2)+1	z_2+1 or INT(z_2)+1
2	< 90°	> 90°	< 90°	x_2+1 or INT(x_2)+1	y_2-1 or INT(y_2)-1	z_2+1 or INT(z_2)+1
3	> 90°	> 90°	< 90°	x_2 - 1 or INT(x_2)-1	y_2 -1 or INT(y_2)-1	z_2 + 1 or INT(z_2)+1
4	< 90°	< 90°	> 90°	x_2 + 1 or INT(x_2)+1	y_2 +1 or INT(y_2)+1	z_2 - 1 or INT(z_2)-1
5	> 90°	< 90°	> 90°	x_2 - 1 or INT(x_2)-1	y_2 + 1 or INT(y_2)+1	z_2 - 1 or INT(z_2)-1
6	> 90°	> 90°	> 90°	x_2 - 1 or INT(x_2)-1	y_2 - 1 or INT(y_2)-1	z_2 - 1 or INT(z_2)-1
7	< 90°	> 90°	> 90°	x_2 + 1 or INT(x_2)+1	y_2 - 1 or INT(y_2)-1	z_2 - 1 or INT(z_2)-1
8	> 90°	< 90°	< 90°	x_2 - 1 or INT(x_2)-1	y_2 + 1 or INT(y_2)+1	z_2 + 1 or INT(z_2)+1

3.3.6 Step 6: Determining If the Bundle Hits a Quartz Tube Surface or a Channel Surface

As the bundle moves on, it hits one of the following surfaces in the UV disinfection system: quartz tube surface, water surface, channel walls or channel bottom. Before a bundle hits any of the surfaces, updating and recording fluence rate as described in Step 4 of Figure 3-7 will be carried out. The following sequential steps are performed to determine which surface is hit by the bundle and its corresponding fate.

Step 6A: Determining Intersection with a Quartz Tube Surface and Generating a Specular Reflection Bundle from the Surface

Intersection with a Quartz Tube

The intersection of the bundle with one of the quartz tube surfaces is determined by solving a system of three linear equations for the bundle and one equation for the quartz tube surface with circular cross section. These equations are:

$$x_Q - x_B = l_B d_{B-Q} \tag{3-71}$$

$$y_Q - y_B = m_B d_{B-Q} \tag{3-72}$$

$$z_Q - z_B = n_B d_{B-Q} \tag{3-73}$$

$$\left(x_Q - x_L\right)^2 + \left(y_Q - y_L\right)^2 - {r_{Q2}}^2 = 0 \tag{3-74}$$

where

x_Q, y_Q, z_Q = global coordinates of the point of intersection on the quartz tube surface

x_B, y_B, z_B = global coordinates of the original point of the bundle prior to hitting the quartz tube

l_B, m_B, n_B = direction cosines of the incoming bundle, determined in Step 3 if it comes from the original quartz tube,

$d_{B\text{-}Q}$ = distance from Point B on the original quartz tube (shown in Figure 3-13) to the point of intersection on the new quartz surface with an outside radius r_q.

If the bundle is a reflected bundle from the surface of another quartz tube, the direction cosines at that reflection point would need to be determined, as described later in this step. If the bundle comes from a reflection surface other than the original quartz tube, then $d_{B\text{-}Q}$ would be the distance from that reflection surface to the intersection point on the new quartz surface.

In the above equations, x_Q, y_Q, z_Q, and $d_{B\text{-}Q}$ are unknowns. The solution involves solving a quadratic equation by substituting the first two equations into the fourth equation to solve for $d_{B\text{-}Q}$. If no solution exists, it can be concluded that there is no intersection of the bundle with the quartz tube under consideration.

Step 6B: Determining Intersection with Channel Walls and Bottom

The channel position in the global coordinate system is shown in Figure 3-17. The determination of whether a bundle hits a channel wall or bottom is based on the following equations for the bundle and these surfaces:

Channel Walls

$$x_{CW} - x_B = l_B d_{B-CW} \tag{3-81}$$

$$y_{cw} - y_B = m_B d_{B-CW} \tag{3-82}$$

$$z_{CW} - z_B = n_B d_{B-CW} \tag{3-83}$$

$$y_{W1} = 0 \tag{3-84}$$

$$y_{W2} - Y = 0 \tag{3-85}$$

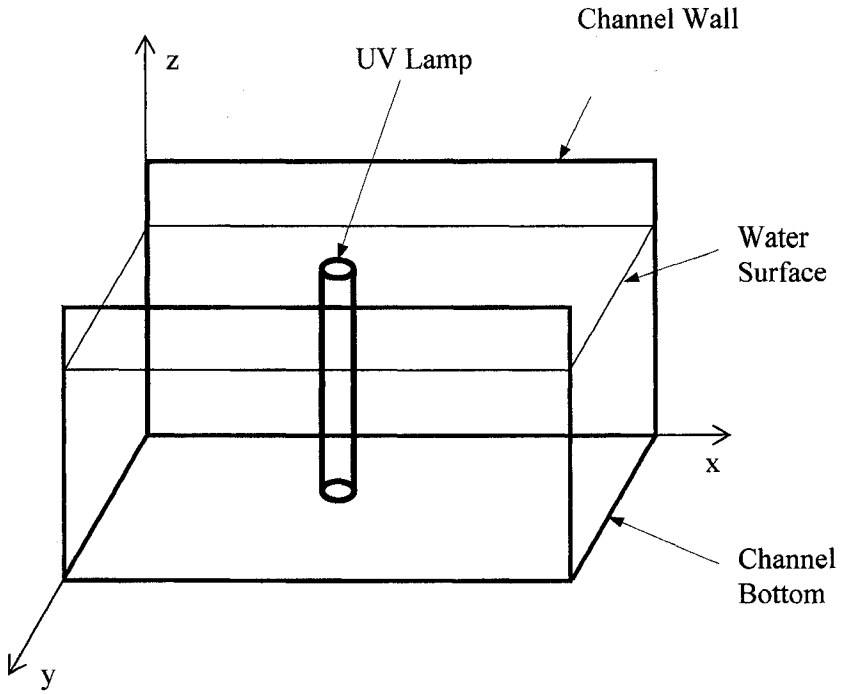

Figure 3-17. Channel Coordinate System

Where x_{CW}, y_{CW}, and z_{CW} are the global coordinates of the intersection point of the bundle with the wall; l_B, m_B, *and* n_B are the direction cosines of the incoming bundle, determined in Step 3 if it comes from the original quartz tube; $d_{B\text{-}CW}$ is the distance from the point on the original quartz tube (Point B shown in Figure 3-13) to the point of intersection at the water-wall interface. If the bundle comes from a reflection surface other than the original quartz tube, $d_{B\text{-}CW}$ would be the distance from that reflection surface to the intersection

point at the water-wall interface. As shown in Figure 3-16, one wall is located at the global x axis and the other wall at the location of $y=Y$ parallel to the x axis. In the above equations, x_{CW}, y_{CW}, z_{CW}, and $d_{B\text{-}CW}$ are the unknowns. If no solution to the above equation exists, it can be concluded that there is no intersection of the bundle with the channel walls. If the bundle hits a channel wall, it is assumed that the wall absorbs all energies from the bundle, and no reflection would occur. Subsequently, a new bundle can be generated based on Step 5B. The assumption is based on the fact that most water/wastewater channels are made of concrete. This assumption is used in the calculations shown in subsequent chapters. However, if a channel wall is made of reflective material such as stainless steel, the reflection calculations described in Step 6A can be used to continue the tracing. If that is the case, the direction of the normal vector would be the opposite of that shown in that step to account for the inward direction of a reflection bundle.

Channel Bottom

$$x_{CB} - x_B = l_B d_{B\text{-}CB} \tag{3-86}$$

$$y_{cB} - y_B = m_B d_{B\text{-}CB} \tag{3-87}$$

$$z_{CB} - z_B = n_B d_{B\text{-}CB} \tag{3-88}$$

$$z_B = 0 \tag{3-89}$$

where x_{CB}, y_{CB}, and z_{CB} are the global coordinates of the intersection point of the bundle with the channel bottom; $d_{B\text{-}CB}$ is the distance from the point on the original quartz tube (Point B shown in Figure 3-13) to the point of intersection at the water-wall interface. If the bundle comes from a reflection surface other than the original quartz tube, $d_{B\text{-}CB}$

would be the distance from that reflection surface to the intersection point at the channel bottom. The channel bottom is located at the plane z=0, as shown in Figure 3-16. In the above equations, x_{CB}, y_{CB}, z_{CB}, and $d_{B\text{-}CB}$ are the unknowns. If a bundle does not hit a quartz tube surface, water surface, or channel wall, it must hit the channel bottom. The same absorption assumption applicable to the wall is applied to the channel bottom.

3.3.7 Step 7: Calculating Direction of Specular Reflection

Generating a Specularly Reflected Bundle from Quartz Tube Surface

Once the bundle hits the quartz tube surface, the bundle is considered to reflect specularly assuming the quartz surface is smooth without fouling. Figure 3-17 shows the basic geometric elements at the reflection location on the quartz tube surface. The vector representing the specular reflection bundle is determined based on the following equation:

$$\vec{v}_r = \vec{v}_i - 2(\vec{v}_i \bullet \vec{n})\vec{n} \quad = \quad v_{ri}i + v_{rj}j + v_{rk}k \tag{3-75}$$

Where $\vec{v}_r$ = specular reflection bundle vector

$\vec{v}_i$ = incident bundle vector

$\vec{n}$ = normal vector

v_{ri}, v_{rj}, v_{rk} = components of the specular reflection bundle vector

In Equation 3-75, v_{ri}, v_{rj}, v_{rk} can be calculated knowing the component of the incident bundle vector and the normal vector. The incident bundle vector is given by

$$\vec{v}_i = (x_Q - x_B)i + (y_Q - y_B)j + (z_Q - z_B)k \tag{3-76}$$

The components of the above vector are $v_{ii}=x_Q - x_B$, $v_{ij} = y_Q - y_B$, and $v_{ik}=z_Q - z_B$.

The normal vector at the intersection point on a surface is determined by

$$\vec{n} = \frac{\nabla S}{|\nabla S|} \tag{3-77}$$

where S represents the surface equation of the quartz tube, Equation 3-74. Using this equation, the normal vector can be written as

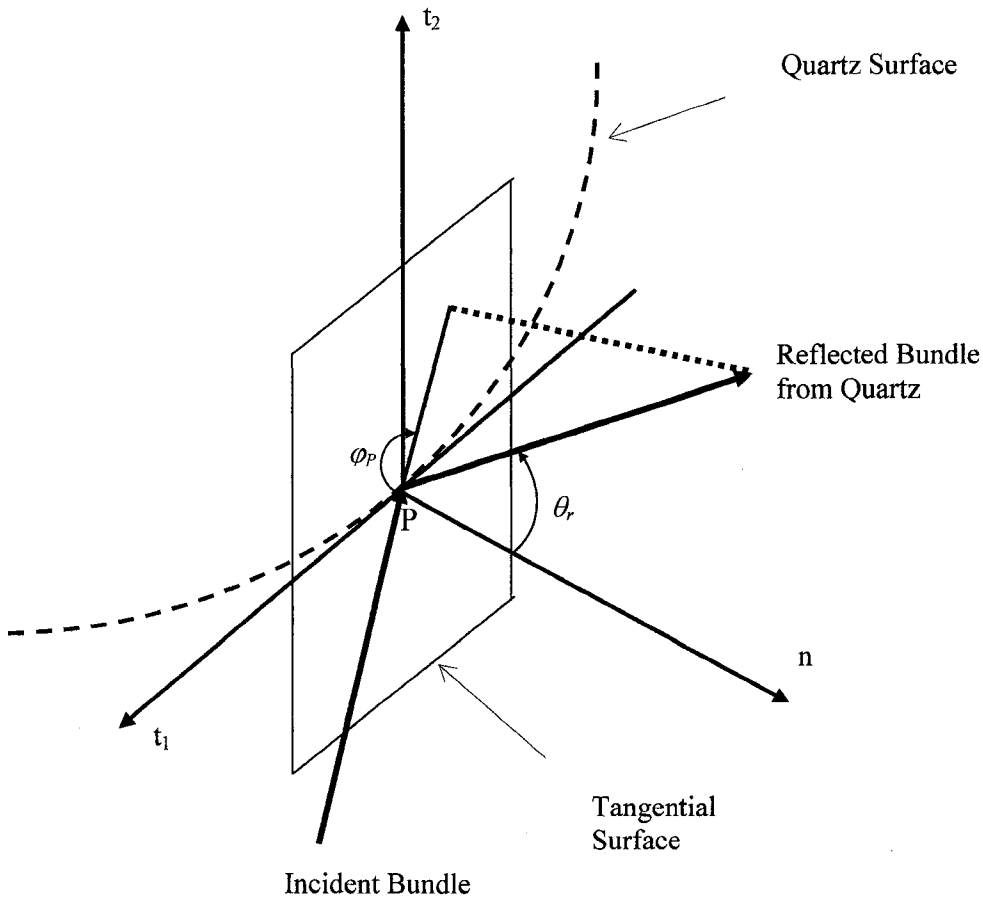

Figure 3-18. Basic Geometric Elements at Quartz Surface Reflection Location

$$\vec{n} = \frac{2(x_q - x_L)i + 2(y_q - y_L)j}{\sqrt{4(x_q - x_L)^2 + 4(y_q - y_L)^2}} = \frac{(x_q - x_L)}{r_q} i + \frac{(y_q - y_L)}{r_q} j \qquad (3\text{-}78)$$

The direction cosines of the reflection vector relative to the global x, *z*, *y*, and *z* axes can be determined by the following equations, respectively:

$$l_r = \frac{v_{ri}}{T_r} \qquad m_r = \frac{v_{rj}}{T_r} \qquad n_r = \frac{v_{rk}}{T_r} \qquad (3\text{-}79)$$

Where *Tr* is the square root of ($v_{ri}^2 + v_{rj}^2 + v_{rk}^2$).

For a bundle emitting from the quartz surface of the original lamp, the reflection bundle at the intersection point on another quartz surface would lie on the same plane as the incident bundle from the original quartz surface. Therefore, the reflection angle at the new quartz surface is ($\pi/2 - \theta_2$) , where θ_2 is calculated in Step 3B, if angle θ_2 is less than 90 degrees, or ($\pi - \theta_2$) if θ_2 is greater than 90 degrees.

For a bundle coming to a quartz tube surface from another location, such as a location on the water surface or a quartz surface other than the original quartz tube, the angle of incident bundle (θ_r) can be calculated by the following equation:

$$\cos\theta_r = \frac{\vec{v}_i \bullet \vec{n}}{|\vec{v}_i||\vec{n}|} = \frac{(v_{ii} \times n_i) + (v_{ij} \times n_j) + (v_{ik} + n_k)}{\left(\sqrt{v_{ii}^2 + v_{ij}^2 + v_{ik}^2}\right)\left(\sqrt{n_i^2 + n_j^2}\right)} \qquad (3\text{-}80)$$

The angle of refraction at the quartz tube surface can be calculated using Snell's law, equation 3-7. The reflectance and irradiance of the reflected bundle at that location can be calculated as in Step 3B. The ray tracing continues with Step 4 if the irradiance is still higher than the threshold based on the irradiance of the bundle at the original quartz tube surface.

3.4 APPLICATIONS OF SIMULATED FLUENCE RATE DATA

Fluence rates are used directly to determine UV dose, also called fluence, which is defined as the factor of fluence rate and exposure time. Dose is expressed in the units of mW-s/cm^2 or, more commonly, in J-s. The determination of UV dose for a system is important in that it is an indication of the amount of UV energy that a microorganism traveling through the system is predicted to be exposed to. Dose data can be used to mathematical reactor models to predict levels of disinfection.

Simulation results obtained by the MCRT method developed in this study can be used as the fluence rate. The residence time can be estimated by performing the tracer test to determine residence time distribution or developing a computational fluid dynamic to determine velocity distribution throughout the system. For multiple vertical lamp systems, variation in flow velocities within the system due to the presence of turbulence, vortex, stagnation zone, boundary layers, and other flow phenomena, determination of flow distribution could be complex. Such data can be used with the fluence rate distribution to determine the dose distribution for the system. However, when such data is not available, average fluence rate and residence time have been used to determine the average dose. This approach is practical for a simple system with one lamp or a few horizontal lamps, in which the residence time can be roughly estimated as the ratio of the flow rate to the flow cross sectional area (excluding areas occupied by the lamps). In such a case, dose is simply expressed as

$$D_{Avg} = E_{Avg} t_{Avg} \tag{3-90}$$

Where E_{Avg} is the average fluence rate of the system, and t_{Avg} is the average residence time or exposure time for the system.

Dose data are used in a computational model to determine the disinfection efficiency. The simplest and most commonly used model is the Chick-Watson model, which is the first order model for a completely mixed batch reactor. This model is given by

$$\frac{dN}{dt} = e^{-kD} \quad => \quad \frac{N}{N_0} = e^{-kD} \tag{3-91}$$

In the above equation, N_0 represents the concentration of representative microorganisms in influent sample, N represents the concentration of the microorganisms in the effluent sample, k represents the reaction constant, and D is the applicable dose.

More complex analytical models called series event models were proposed by Severin *et al* (1983) as shown below

$$\frac{N}{N_0} = e^{-kD}(1 + kD) \tag{3-92}$$

$$\frac{N}{N_0} = e^{-kD}(1 + kD + \frac{(KD)^2}{2}) \tag{3-93}$$

$$\frac{N}{N_0} = e^{-kD}(1 + kD + \frac{(KD)^2}{2} + \frac{(KD)^3}{6}) \tag{3-94}$$

The series event models are the extensions of the Chick-Watson model, and each additional term on the right hand side of the equations represents an additional theoretical stage of treatment or damage to microorganisms exposed to UV light.

Fluence rate distribution data are potentially useful in determining locations of UV sensors as well as estimating Reduction Equivalent Dose (RED), in conjunction with other system specific parameters. Considering the limited number of locations of sensors that could be placed in UV disinfection systems, three dimensional UV fluence rate data

could be used as supplemental information about the nature of such a system with regard to fluence rate distribution and potential effects on RED of such systems.

CHAPTER 4

MCRT SIMULATIONS

One of the objectives of this study was to develop computer programs that address important radiation principles discussed in Chapter 3 based on Monte Carlo Ray-Tracing methods. These programs serve as robust tools for studying effects of reflections and lamp spacing on fluence rate distribution in UV systems. To achieve this objective, several computer programs were developed in Fortran to determine fluence rates in three dimensional space of water, wastewater or air disinfection systems with any number of low pressure lamps. Changes in lamp dimensions and lamp spacing can be made with minimum programming effort. The programs can be executed using a personal computer with the Windows XP operating system. This chapter discusses important programming aspects and Monte Carlo Ray-Trace simulations.

4.1 PROGRAMMING

Modeled Systems

The modeled systems to which the MCRT programs are applied in this study include those with low pressure (LP) lamps oriented vertically in channel with rectangular cross sectional area typically found in water and wastewater treatment systems. Common sizes of these lamps and quartz tubes are 1 cm in diameter and 2.5 cm in diameter, respectively. UV systems with one lamp, two lamps, four lamps, and one to several rows of five lamps were studied using the MCRT method developed in this

research. A schematic of a system with a bank of 25 lamps, including five lamps per row, is shown in Figure 4-1. A similar system has been used by other investigators to study hydrodynamic patterns (Blatchley *et al.* 1995 and 1997; Loge *et al.* 1996; Chiu, 1998; Chiu *et al.* 1999; and Iranpour *et al.* 1999).

The programs were developed based on the rectangular coordinate system (x, y, and z) in which fluence rate at any location within the system can be obtained and retrieved, given the coordinates of the location. Parameters related to lamp spacing, lamp dimensions, channel dimensions, optical properties, and simulation data can be changed in the input data section of the computer program. Even though the computer program was developed to model the vertical UV systems mentioned above, the program could be modified to calculate fluence rate for other UV disinfection systems such as horizontal systems or systems used to treat air instead of water.

Programming Algorithm

The programming algorithm is based on the block diagram shown in Figure 4-2. This figure is essentially similar to Figure 3-7 discussed in Chapter 3. Two primary DO loops, with one nested in the other, were set up to simulate all of the predetermined numbers of bundles from each lamp of the system. All ray tracing steps for each bundle were preformed in the nested DO loop. The outer DO loop tracked the number of lamps in the system. Three subroutines were developed to calculate fluence rates for each volume element in the three dimensional space of the system, determine intersection points of a bundle with surrounding quartz sleeve surfaces, and reflection angles of the bundle at those locations.

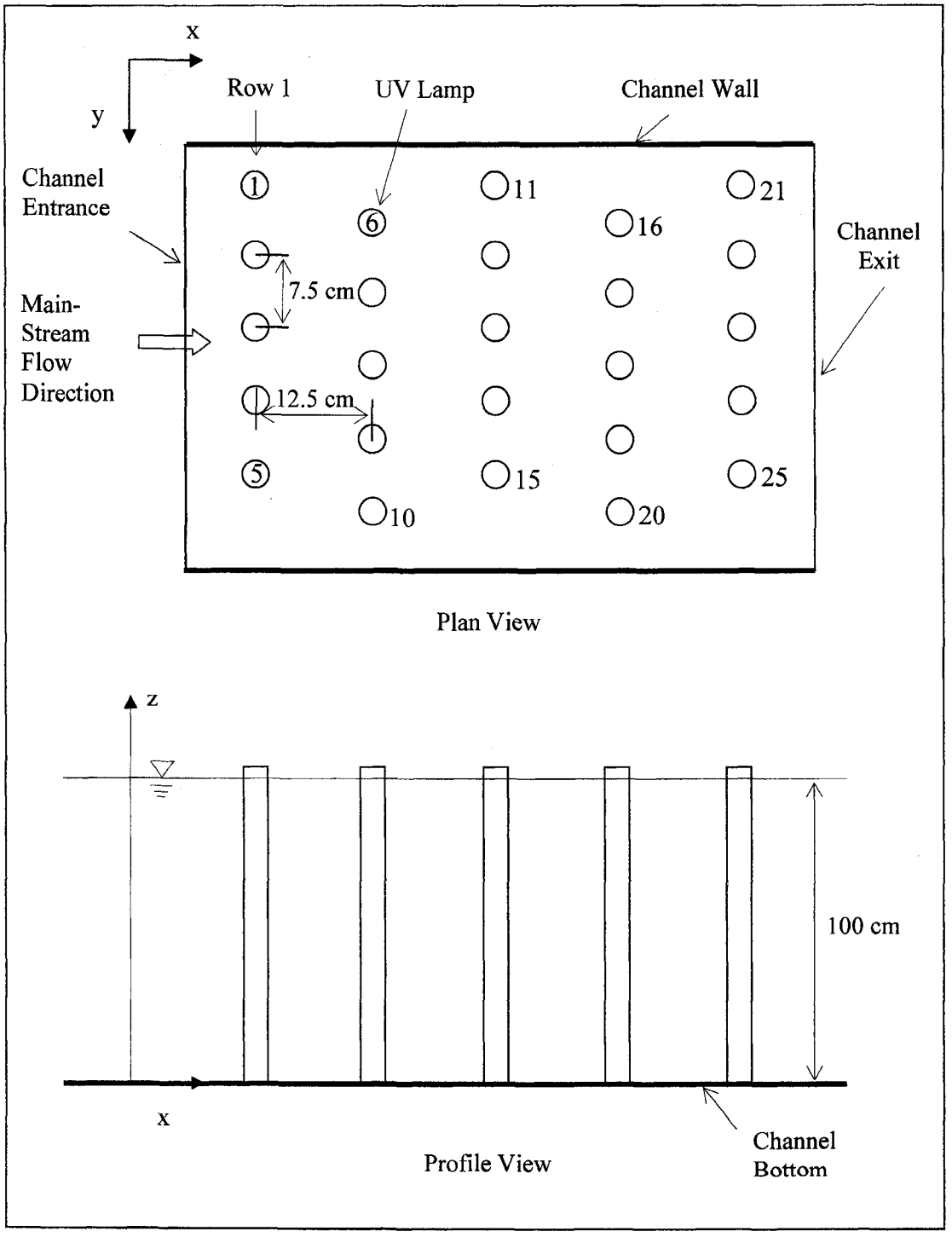

Figure 4-1. Typical Modeled System Schematic

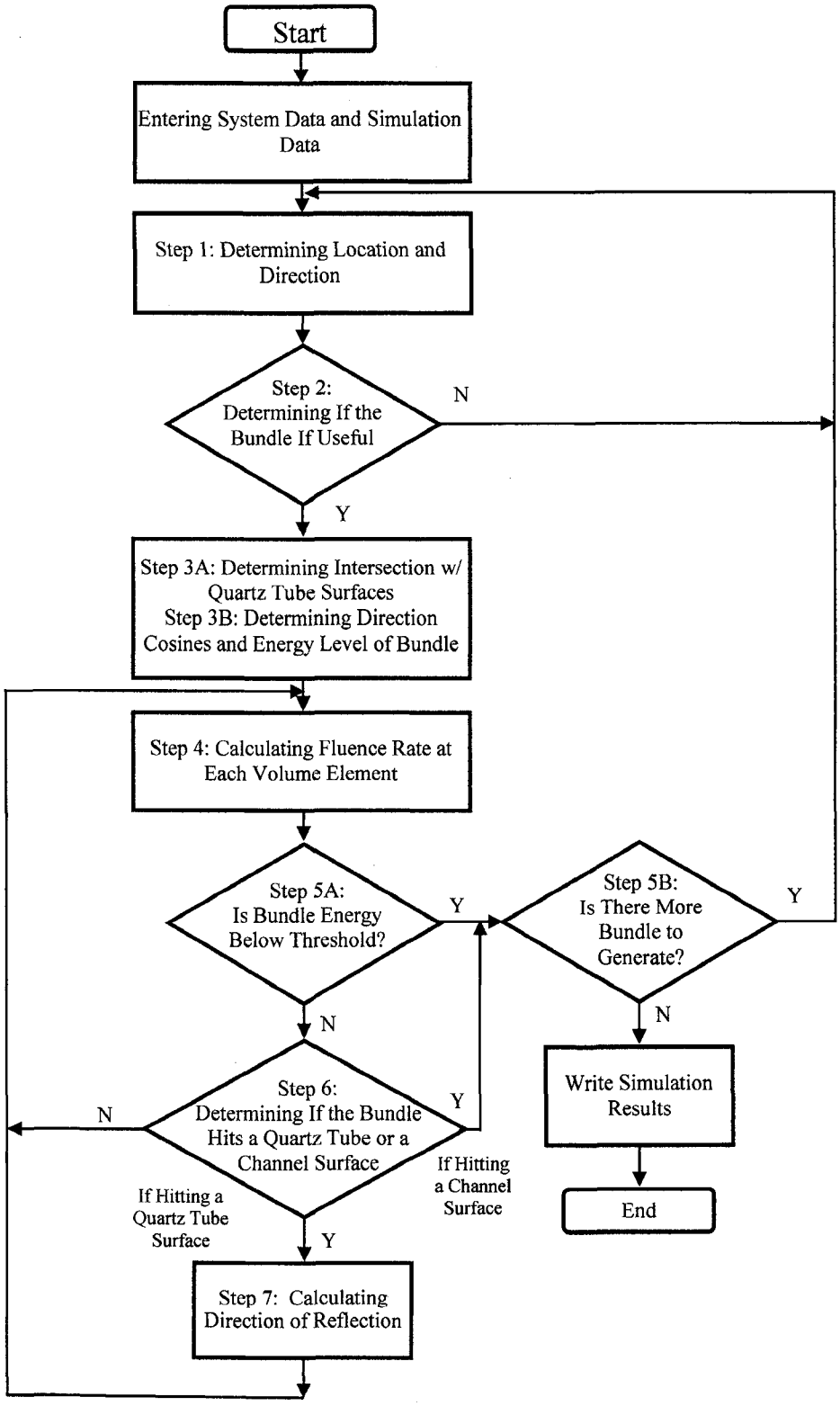

Figure 4-2. Block Diagram for MCRT Method

also used in Step 7 in case of bundles intersecting quartz tube surfaces to calculate angles of reflection and direction angles with respect to the global coordinate system.

Indexing Surface and Volume Elements

Fluence rates at quartz tube surfaces were recorded for each surface element receiving bundle energies from the lamp axis. Each quartz tube surface was divided into equal areas of approximately 1 cm^2. This element size was selected for consistency with the common fluence rate units of mW/cm^2. A smaller subdivision is considered unnecessary because the dimensions of the lamp and channel are much larger than the chosen size. When an energy bundle emitted from the lamp axis hits the quartz-water interface, the intersection point is located in a surface element whose index number is determined based on the unique global coordinates (x, y, and z) of the points using the following equation:

$$j = INT(z)\times\left(INT\left(2\pi r_q\right)+1\right)+INT\left(\frac{\varphi\times\left(INT\left(2\pi r_q\right)+1\right)}{360}+1\right) \qquad (4\text{-}1)$$

where j = local index number of each surface element

INT = Fortran function that returns an integer

z = vertical coordinate of the intersection point, cm

rq = radius of the quartz tube, cm

φ = circumferential angle on the x-y plane

An index is assigned to the cumulative irradiance at each surface element for data storage in a one dimensional vector for minimizing storage memory demands.

Each modeled system is divided into 1 cm^3 volume elements. Specific x, y, and z coordinates of the center point of the volume element associated with each fluence rate data point are converted to corresponding integer indexes n_x, n_y, and n_z based on which fluence data point is stored in the computer. These indexes correspond to the coordinates of the center of the cubic volume, which are estimated by taking the average of the x, y, and z coordinates of the bundle before and after hitting a new volume element. Volume elements are also indexed based on their positions in the system relative to the global coordinates using the following equation:

$$n = (i_{\max} \times j_{\max} \times k_{\max}) + (j \times i_{\max}) + i + 1 \qquad (4\text{-}2)$$

where n = global index number of the volume element

i_{max} = the maximum integer value of the x-coordinate of a volume element, corresponding to the limited length of the channel

j_{max} = the maximum integer value of the y-coordinate of a volume element, corresponding to the width of the channel

j = integer value of the y-coordinate of a volume element

k = integer value of the z-coordinate of a volume element

The fluence rate of each volume element is also stored in the computer as a three dimensional array or a one dimensional array such as *fluence_rate*(n_x,n_y,n_z) or one-dimensional array such as *fr(n)*. These arrays are useful in retrieving fluence data at any location throughout the channel, given the global coordinates of that location.

Random Number Generation

Random numbers are generated using random number generation subroutines RNSET and RNUN from the International Mathematics and Statistics Library (IMSL). A random seed number can be manually entered in the computer program for every run. The value of the random seed ranges from 0 to 214748363646. The seed needs to be entered only once to generate random numbers for each run, which involves the generation of millions of random numbers. If a seed number is not entered in the computer program, the system clock will be used by the subroutine as a random seed number, which constantly changes from one run to the next.

The above IMSL subroutines generate random numbers based on a multiplicative congruential method in which one of the following three multipliers is used: 16807 (which is 7^5), 397204094 (which is $2 \times 7^2 \times 4053103$), and 950706376 (which is $2^3 \times 118838297$) (IMSL, 1997). Use of any of the multipliers is acceptable, considering extensive empirical testing of some of the uniform random number generators available in subroutine RNUN, as reported by IMSL. The first multiplier is known to yield the fastest execution time and was used in the MCRT simulation programs demonstrated in the current study.

The calculations in the program are performed sequentially based on the same essential steps shown in Figure 4-2 for one bundle at a time. Consequently, as the number of bundles increases, the execution time increases. Data related to the number of simulated bundles and corresponding execution times when using the MCRT program are discussed in the next section.

4.2 MONTE CARLO RAY-TRACE SIMULATIONS

Input and Output Data

Typical types of input and output data are listed in Tables 4-1 and 4-2, respectively. Input data can be entered directly into the computer program. A copy of the computer output is shown in Appendix A. Of special importance is the use of a random seed number for each run, as discussed above, to ensure the randomness of simulation results.

Convergence Tests

The MCRT method is basically a probabilistic sampling procedure in which simulation results change from one run to the next due to changes in values of random numbers. However, in spite of the randomness and changes in simulation results, when the number of simulated bundles is large enough, converged results would be obtained. The convergence of a set of runs was confirmed based on the following criterion: fluence rates were within 10% difference from one run to the next. To satisfy this criterion, fluence rate data in the radial distance from the quartz tube surface in both x and y directions were recorded for comparison of data from all trial runs with the increased number of bundles. Convergence data for simulation of fluence rate distribution for a 27.6 W lamp with 1.25 cm radius quartz tube submerged vertically in a container with 100 cm of water depth were summarized in Table 4-1.

Table 4-1. Typical Input Data for MCRT Simulations

Type of Input Data and Typical Units
Lamp Information - Lamp power (W); spectral distribution (medium pressure lamps) - Lamp length (cm) - Lam radius (cm) - Quartz sleeve radius and thickness (cm) - Global coordinates of lamp centers (cm)
Channel Information - Channel length and width (cm) - Depth of water (cm) - Channel coordinates - Channel material - Presence and locations of baffles
Optical Information - Absorption coefficient of water (cm^{-1}) and spectral data as applicable - Absorption coefficient of quartz (cm^{-1}) and spectral data as applicable - Refractive index of UV light in air (dimensionless) - Refractive index of UV light in water (dimensionless) - Refractive index of UV light in quartz (dimensionless)
Simulation Information - Number of bundles to be simulated - Seed number for random number generation - Quartz surface element size (cm^2) - Channel volume element size (cm^3)

As shown in Table 4-3 convergence of the average fluence rate data for the radial distance relative to the quartz surface in the x and y directions began to occur when the number of simulated bundles exceeded one million. Average fluence rates of one run were compared with the preceding run to determine percent changes in the fluence rates. Where no fluence rates were recorded by the program output files, the legend "ND" was shown on the table. The radial distance from the quartz tube surface ranged from 1 cm to 5 cm, relative to the global coordinate system shown in Figure 4-1. The fluence rate data

represented estimated fluence rates along a line normal to the lamp mid-point, at a lamp height of 50 cm from the channel bottom. Data for 15 runs with the number of simulated bundles ranging from 25,000 to 8,000,000 were presented in the table.

Table 4-2 Typical Output Data from MCRT Simulations

Type of Output Data and Typical Units
Fluence Rate Data
- Fluence rate on quartz surfaces (mW/cm2)
- Fluence rate of any volume element in the channel (mW/cm2)
- Average fluence rates of the system or certain zones in the system (mW/cm2)
Optical Information
- Reflectivity at each interface (dimensionless)
- Reflectance across a quartz tube (dimensionless)
- Absorbance and transmittance of a medium in the system

As shown in the table, changes in average fluence rates for the radial distance within a few centimeters from the quartz tube surface exceeded 10 percent when the number of simulated bundles was less than one million. In addition, insignificant fluence rate data for a number of volume elements were recorded as zero values in simulation output files. As the number of bundles increased, fluence rates of these volume elements were recorded as non-zero values. Changes in the fluence rates at radial distances greater than 10 centimeters still exceeded 1o percent at a higher level of simulations. However, because the magnitude of fluence rates at these locations were

insignificant compared with those within a few centimeters from the quartz surface, such changes would not affect the overall fluence rate distribution.

Figure 4-3 shows the fluence rates at radial distances of 1 cm to 4 cm with respect to the number of simulated bundles. As shown in this figure, the fluence rates within 1 cm fluctuated between approximately 8 mW/cm^2 to 12 mW/cm^2. When the number of bundles exceeded one million, the fluence rates at the radial locations were stable. Simulation results for systems with more than one lamp were expected to converge at a lower number of bundles due to repeated simulations from different lamps. Based on the convergence test results, the number of bundles ranging from one million to two million were considered appropriate for simulation of such systems for the purpose of evaluation of reflection and spacing effects, as discussed in Chapter 6.

Table 4-3 Convergence Test Data

Run 1 (100,000 Bundles)

Radial Distance From Sleeve (cm)	Fluence Rate at Pt. 1 (mW/cm^2)	Fluence Rate at Pt. 2 (mW/cm^2)	Average Fluence Rate (mW/cm^2)	Changes in Fluence Rate (%)
1	4.84	7.82	6.33	
2	3.79	4.25	4.02	
3	3.11	4.21	3.66	
4	2.36	3.36	2.86	
5	2.28	2.75	2.51	
6	1.92	2.32	2.12	
7	1.50	1.45	1.47	
8	1.37	1.64	1.50	
9	1.47	1.65	1.56	
10	1.36	1.70	1.53	

Table 4-3 (Continued)

Run 2 (250,000 Bundles)

Radial Distance From Sleeve (cm)	Fluence Rate at Pt. 1 (mW/cm^2)	Fluence Rate at Pt. 2 (mW/cm^2)	Average Fluence Rate (mW/cm^2)	Changes in Fluence Rate (%)
1	5.44	6.63	6.03	4.7
2	3.74	5.15	4.44	-10.4
3	3.58	4.27	3.92	-7.1
4	2.83	3.05	2.94	-2.8
5	2.18	2.14	1.26	13.9
6	1.90	1.75	1.82	14.2
7	1.65	1.45	1.55	-5.4
8	1.44	1.26	1.35	10.0
9	1.18	0.91	1.05	32.7
10	0.92	0.96	0.94	38.6

Table 4-3 (Continued)

Run 3 (500,000 Bundles)

Radial Distance From Sleeve (cm)	Fluence Rate at Pt. 1 (mW/cm^2)	Fluence Rate at Pt. 2 (mW/cm^2)	Average Fluence Rate (mW/cm^2)	Changes in Fluence Rate (%)
1	5.80	6.68	6.24	-3.5
2	4.32	4.76	4.54	-2.3
3	3.27	3.41	3.34	14.8
4	2.43	2.98	2.70	8.2
5	1.71	2.60	2.16	0.0
6	1.86	2.07	1.97	-8.2
7	1.47	1.82	1.64	-5.8
8	1.16	1.50	1.33	1.5
9	0.89	1.06	0.98	6.7
10	0.82	1.07	0.94	0.0

Table 4-3 (Continued)

Run 4 (750,000 Bundles)

Radial Distance From Sleeve (cm)	Fluence Rate at Pt. 1 (mW/cm^2)	Fluence Rate at Pt. 2 (mW/cm^2)	Average Fluence Rate (mW/cm^2)	Changes in Fluence Rate (%)
1	6.10	6.56	6.33	-1.4
2	4.38	5.17	4.77	-5.1
3	3.46	3.89	3.67	-9.9
4	2.64	3.12	2.88	-6.7
5	1.91	2.47	2.19	-1.4
6	1.61	2.02	1.82	7.6
7	1.32	1.60	1.46	11.0
8	1.16	1.40	1.28	3.8
9	0.96	1.15	1.06	-8.2
10	0.86	0.99	0.93	1.1

Table 4-3 (Continued)

Run 5 (1,000,000 Bundles)

Radial Distance From Sleeve (cm)	Fluence Rate at Pt. 1 (mW/cm^2)	Fluence Rate at Pt. 2 (mW/cm^2)	Average Fluence Rate (mW/cm^2)	Changes in Fluence Rate (%)
1	6.21	7.00	6.61	-4.4
2	4.45	4.90	4.68	1.9
3	3.25	3.80	3.53	3.8
4	2.47	3.27	2.87	0.3
5	1.90	2.72	2.31	-5.5
6	1.78	2.14	1.96	-7.7
7	1.59	1.83	1.71	-17.1
8	1.39	1.52	1.46	-14.1
9	1.15	1.41	1.28	-20.8
10	0.90	1.09	1.00	-7.5

Table 4-3 (Continued)

Run 6 (2,000,000 Bundles)

Radial Distance From Sleeve (cm)	Fluence Rate at Pt. 1 (mW/cm^2)	Fluence Rate at Pt. 2 (mW/cm^2)	Average Fluence Rate (mW/cm^2)	Changes in Fluence Rate (%)
1	6.47	6.59	6.53	1.2
2	4.11	4.69	4.40	6
3	3.22	3.77	3.50	0.8
4	2.48	3.17	2.83	1.4
5	2.02	2.48	2.25	2.6
6	1.84	2.05	1.95	0.5
7	1.45	1.74	1.60	6.4
8	1.22	1.49	1.36	6.8
9	1.09	1.27	1.18	7.8
10	1.01	1.08	1.05	-5.0

Table 4-3 (Continued)

Run 7 (3,000,000 Bundles)

Radial Distance From Sleeve (cm)	Fluence Rate at Pt. 1 (mW/cm^2)	Fluence Rate at Pt. 2 (mW/cm^2)	Average Fluence Rate (mW/cm^2)	Changes in Fluence Rate (%)
1	5.95	6.67	6.31	3.4
2	4.40	4.93	4.67	-6.1
3	3.12	3.85	3.49	0.3
4	2.49	3.02	2.76	2.5
5	1.98	2.54	2.26	-0.4
6	1.59	2.14	1.82	6.7
7	1.35	1.78	1.57	1.9
8	1.24	1.50	1.37	-0.7
9	1.05	1.26	1.16	1.7
10	0.91	1.07	1.00	4.8

Table 4-3 (Continued)

Run 8 (4,000,000 Bundles)

Radial Distance From Sleeve (cm)	Fluence Rate at Pt. 1 (mW/cm^2)	Fluence Rate at Pt. 2 (mW/cm^2)	Average Fluence Rate (mW/cm^2)	Changes in Fluence Rate (%)
1	6.19	6.58	6.38	-1.1
2	4.51	4.89	4.70	-0.6
3	3.38	3.76	3.57	-2.3
4	2.63	3.07	2.85	-3.3
5	2.12	2.42	2.27	-0.4
6	1.84	2.15	2.00	-9.9
7	1.53	1.81	1.67	-6.4
8	1.31	1.51	1.41	-2.9
9	1.06	1.25	1.16	0.0
10	0.96	1.07	1.02	-2.0

Table 4-3 (Continued)

Run 9 (5,000,000 Bundles)

Radial Distance From Sleeve (cm)	Fluence Rate at Pt. 1 (mW/cm^2)	Fluence Rate at Pt. 2 (mW/cm^2)	Average Fluence Rate (mW/cm^2)	Changes in Fluence Rate (%)
1	6.03	6.65	6.34	0.6
2	4.31	4.88	4.60	2.1
3	3.34	3.70	3.52	1.4
4	2.57	2.78	2.68	6.0
5	1.98	2.31	2.15	5.3
6	1.68	2.03	1.86	7.0
7	1.49	1.78	1.64	1.8
8	1.29	1.45	1.37	2.8
9	1.07	1.21	1.14	1.7
10	0.99	1.04	0.97	4.9

Table 4-3 (Continued)

Run 10 (6,000,000 Bundles)

Radial Distance From Sleeve (cm)	Fluence Rate at Pt. 1 (mW/cm^2)	Fluence Rate at Pt. 2 (mW/cm^2)	Average Fluence Rate (mW/cm^2)	Changes in Fluence Rate (%)
1	6.00	6.83	6.42	-1.3
2	4.31	5.04	4.68	-1.7
3	3.31	3.83	3.57	-1.4
4	2.55	3.02	2.79	-4.1
5	2.13	2.51	2.32	-7.9
6	1.83	2.14	1.99	-7.0
7	1.52	1.75	1.64	0.0
8	1.28	1.51	1.40	-2.2
9	1.12	1.30	1.21	-6.1
10	1.00	1.10	1.05	-8.2

Table 4-3 (Continued)

Run 11 (7,000,000 Bundles)

Radial Distance From Sleeve (cm)	Fluence Rate at Pt. 1 (mW/cm^2)	Fluence Rate at Pt. 2 (mW/cm^2)	Average Fluence Rate (mW/cm^2)	Changes in Fluence Rate (%)
1	6.22	6.86	6.54	-1.9
2	4.38	5.02	4.70	-0.4
3	3.30	3.91	3.61	-1.1
4	2.60	3.06	2.83	-1.4
5	2.10	2.51	2.30	0.9
6	1.75	2.10	1.93	3.0
7	1.49	1.76	1.63	0.6
8	1.24	1.49	1.37	2.1
9	1.09	1.25	1.17	3.3
10	0.94	1.06	1.00	4.8

Table 4-3 (Continued)

Run 12 (8,000,000 Bundles)

Radial Distance From Sleeve (cm)	Fluence Rate at Pt. 1 (mW/cm^2)	Fluence Rate at Pt. 2 (mW/cm^2)	Average Fluence Rate (mW/cm^2)	Changes in Fluence Rate (%)
1	5.98	6.82	6.40	2.1
2	4.28	5.09	4.69	0.2
3	3.18	3.83	3.51	2.8
4	2.48	3.12	2.80	1.1
5	2.08	2.51	2.30	0.0
6	1.74	2.02	1.88	2.6
7	1.49	1.75	1.62	0.6
8	1.29	1.49	1.39	-1.5
9	1.13	1.26	1.20	-2.6
10	0.94	1.11	1.03	-3.0

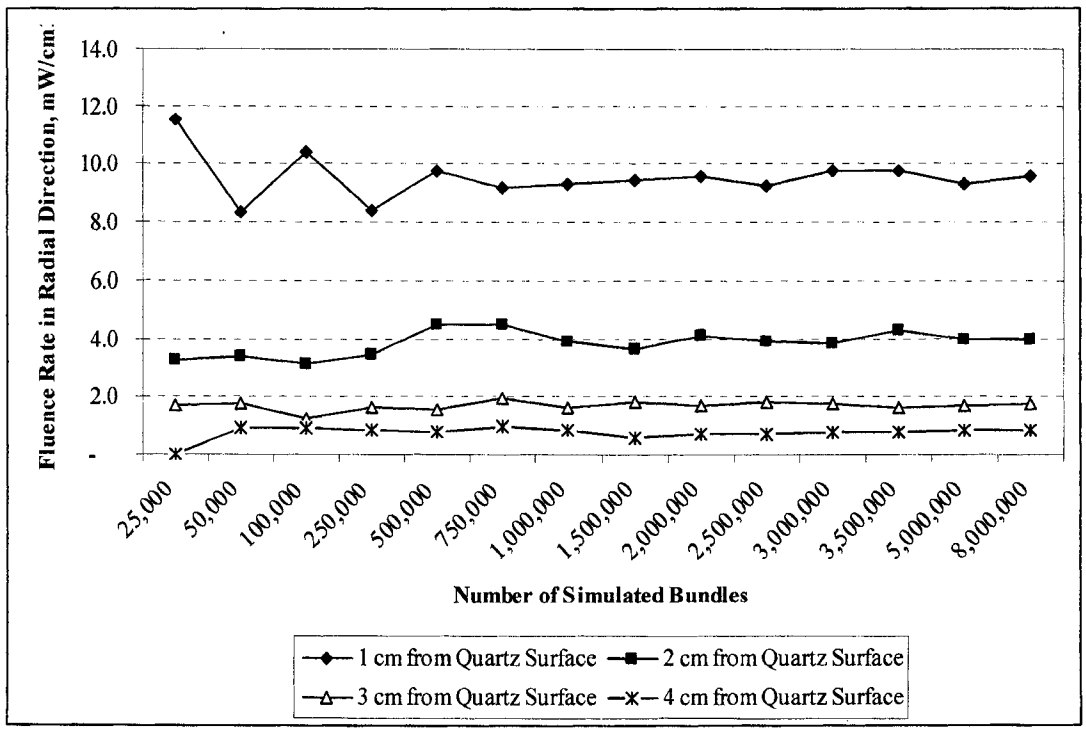

Figure 4-3. Effects of Number of Simulated Bundles on Fluence Rate Distributions (26,700 mW lamp with 100 cm length and 1.25 cm Quartz Tube Radius)

CHAPTER 5

VALIDATION OF THE MCRT METHOD

In this chapter, model estimates from the proposed MCRT simulations were compared with three sets of observed experimental data provided by two independent sources and with one well recognized UV computational model. The first set of data was provided by Bolton Photosciences Inc. based on the results of experimental work that involved the use of a chemical actinometry to measure fluence rates of UV reactors with water (Rahn *et al.*, 2000). The second set of data was provided by Trojan Technologies Inc. based on the results of experimental work that involved the use of a sensor to measure UV irradiance in the air (Sasges *et al.*, 2007). Model estimates from MCRT simulations were also compared with simulation data obtained from the Point Source Summation (PSS) Model (Jacob and Dranoff, 1970). What follows is a detailed discussion of the MCRT model validation and comparison of simulated model estimates.

5.1 VALIDATION OF THE MCRT METHOD

5.1.1 Comparison with Measured Fluence Rates in Water

The experimental data used in the validation was generated by iodide/iodate actinometry. The experimental work was performed by Rahn *et al.* (2000) for determining fluence rate at various distances from a lamp with a quartz sleeve submerged in water with two levels of UV transmission of 100 percent, which represented clear water, and 73 percent using filtered instant coffee, which represented wastewater. In

these experiments, iodide/iodate solutions in the forms of potassium iodide (KI) and potassium iodate (KIO_3) contained in 1 cm spherical vessels made from quartz tubing were exposed to UV light emitted from a single lamp placed in water with the above UV transmission specifications.

The spheres with the actinometric solution were placed at several locations surrounding the lamp. As a result of the UV light exposure, chemical reactions occurred to form triiodide ions (I_3^-) that were directly related to the number of photons absorbed in the solution and corresponding fluence rates at specific locations where the spherical vessels were placed in the experimental system. Additional details of the experiments and experimental data were reported by Stefan *et al.* (2001).

The following are three representative chemical reactions (Rahn *et al.*, 2000):

$$I^- + h\gamma \rightarrow I^\bullet + e_{aq}^- \qquad (5\text{-}1)$$

$$2\,I^\bullet + I^- \rightarrow I_3^- \qquad (5\text{-}2)$$

$$e_{aq}^- + IO_3^- \rightarrow IO^- + H_2O_2 + OH^- + \bullet OH \qquad (5\text{-}3)$$

Triiodide ion is formed by the first two reactions and complex reactions of the oxidizing species in Reaction 5-3 with iodine and iodine atoms.

Fluence rates, E', exposed by each sphere were then determined by (Rahn *et al.*, 2000):

$$E' = \frac{27.1 \times A_{352nm} \times V}{Area \times t} \qquad (5\text{-}4)$$

where A_{352nm} = Absorbance at 352 nm

V = Volume of the actinometric solution, mL

$Area$ = Cross sectional area of the sphere, cm^2

t = Exposure time, seconds

27.1 = Conversion factor, obtained by dividing the energy of one mole of photons at 254 nm wavelength (4.716×10^8 mJ) by the molar absorption coefficient (27,590 M^{-1} cm^{-1}), the quantum yield of 0.63, and a factor of 1,000 for conversion from L to mL.

Table 5-1 summarizes data from the experimental system used by Stefan *et al.* The same data was employed in the MCRT simulations for the purpose of validating the proposed MCRT method. UV transmissions of 100 percent and 73 percent corresponded to the absorption coefficient of 0 cm^{-1} and 0.137 cm^{-1}, respectively. The UVC emitting efficiency and quantum yield were incorporated into the Beer-Lambert's absorption law (Equation 16) in the calculation of fluence rates at actinometric sphere locations.

Table 5-1. Experimental System Information

Parameter	Data
Lamp Emitting Power	12.4 W
Lamp Length	15.0 cm
Quartz Sleeve Radius	3.2 cm
Quartz Sleeve Thickness	3.0 mm
UV Transmissions of Tested Water and	100.0 % and 73.0 %
UVC Emitting Efficiency of Lamp (Manufacturer's Specification)	31.0 %
Quantum Yield at 21°C	0.63

Fluence rate data reported by Rahn *et al.* (2000) under the same actinometric testing conditions are listed in Tables 5-2 and 5-3, respectively. These data represented

Table 5-2. Observed Experimental Fluence Rate Data for a UV Reactor with 100 % UV Transmission Water (Rahn *et al.* 2000)

Vertical Distance from Lamp Center (cm)	Horizontal Distance from Quartz Sleeve (cm)	Fluence Rate (mW/cm^2)
-8.6	3.8	1.448
-4.5	4.3	2.660
-0.9	4.4	3.316
3.2	3.7	2.980
6.7	4.1	2.455
10.5	3.1	1.145
15.0	3.5	0.313
-10.0	5.7	0.957
-6.3	6.4	1.647
-2.4	6.4	2.098
0.8	6.2	2.278
4.4	6.9	1.835
7.8	6.9	1.208
11.5	7.4	0.654
14.8	6.4	0.306
-10.0	8.9	0.806
-6.8	9.0	1.202
-3.0	9.5	1.415
0.2	9.3	1.524
3.6	9.5	1.292
6.8	10.1	0.957
10.1	10.1	0.654
14.6	9.3	0.311
-9.6	11.3	0.645
-6.3	11.7	0.865
-3.1	12.1	0.966
0.3	12.1	0.980
3.6	12.0	0.964
7.0	12.0	0.757
10.2	12.1	0.541
14.5	12.1	0.311
-9.1	13.0	0.603
-5.8	12.4	0.886
-2.2	12.8	0.975
2.5	13.0	0.915
7.2	12.9	0.748
11.5	13.1	0.429

Table 5-3. Observed Experimental Fluence Rate Data for a UV Reactor with 73 % UV Transmission Water (Rahn *et al.*, 2000)

Vertical Distance from Lamp Center (cm)	Horizontal Distance from Quartz Sleeve (cm)	Fluence Rate (mW/cm^2)
-5.6	2.3	0.884
-1.0	2.3	1.356
2.8	2.2	1.547
6.9	2.2	1.501
11.0	2.5	1.139
15.8	2.4	0.387
-7.5	5.6	0.228
-3.6	5.6	0.422
-0.3	5.7	0.488
3.6	5.4	0.527
7.2	5.7	0.369
11.1	5.3	0.136
13.6	5.2	0.065
17.3	4.7	0.017
-7.7	8.5	0.074
-3.8	8.7	0.117
-0.1	8.9	0.133
3.2	8.8	0.132
7.0	8.5	0.103
10.9	8.7	0.051
14.2	8.4	0.018
17.1	8.1	0.007
-7.5	11.3	0.022
-3.5	11.7	0.031
0.7	11.4	0.040
4.7	11.6	0.035
8.6	11.6	0.023
12.4	11.5	0.012
16.8	11.6	0.004
-7.0	12.6	0.016
-1.7	12.6	0.024
3.0	12.6	0.023
8.3	12.5	0.018
12.6	12.5	0.009
16.9	12.1	0.004

the fluence rate at locations relative to the lamp center and quartz sleeve. The distance data indicated that the spheres were placed up to 2.5 cm below the line normal to the quartz sleeve surface at the bottom of the sleeve and approximately 10 cm above the line normal to the quartz sleeve surface at the top of the sleeve.

To calculate fluence rates in and from the UV reactor system, a lamp coordinate system was set up as shown in Figure 5-1. The figure shows that the center of the lamp was arbitrarily chosen to be 13 cm from the origin of the vertical axis z'. Correspondingly, the MCRT simulations encompassed a vertical distance from z = 0 to z = 33 cm and a radial distance of 15 centimeters from the lamp axis. The x and y coordinates of the lamp center were chosen to be 15 cm relative to the origin of the global coordinate system. Thus, the above modeling boundaries were chosen to cover all equivalent coordinates of the spheres with respect to the MCRT coordinate system. Three representative sphere locations are also shown in Figure 5-1.

The locational data listed in Tables 5-2 and 5-3 were first converted to corresponding coordinates in the MCRT coordinate system described above. The sphere coordinates are shown in Tables 5-4 and 5-5 for the tested systems with 100 percent UV transmission and 73 percent UV transmission, respectively. The vertical coordinates of the spheres were calculated by adding the vertical distance from the lamp center to one half of the length of the lamp (15 cm and 5.5 cm). The latter distance was arbitrarily chosen to cover the sphere locations at the vertical position below the bottom of the quartz sleeve, such as sphere location 3 shown in Figure 5-1. Further, as shown in these tables, the vertical coordinates were arranged in descending order for ease in plotting.

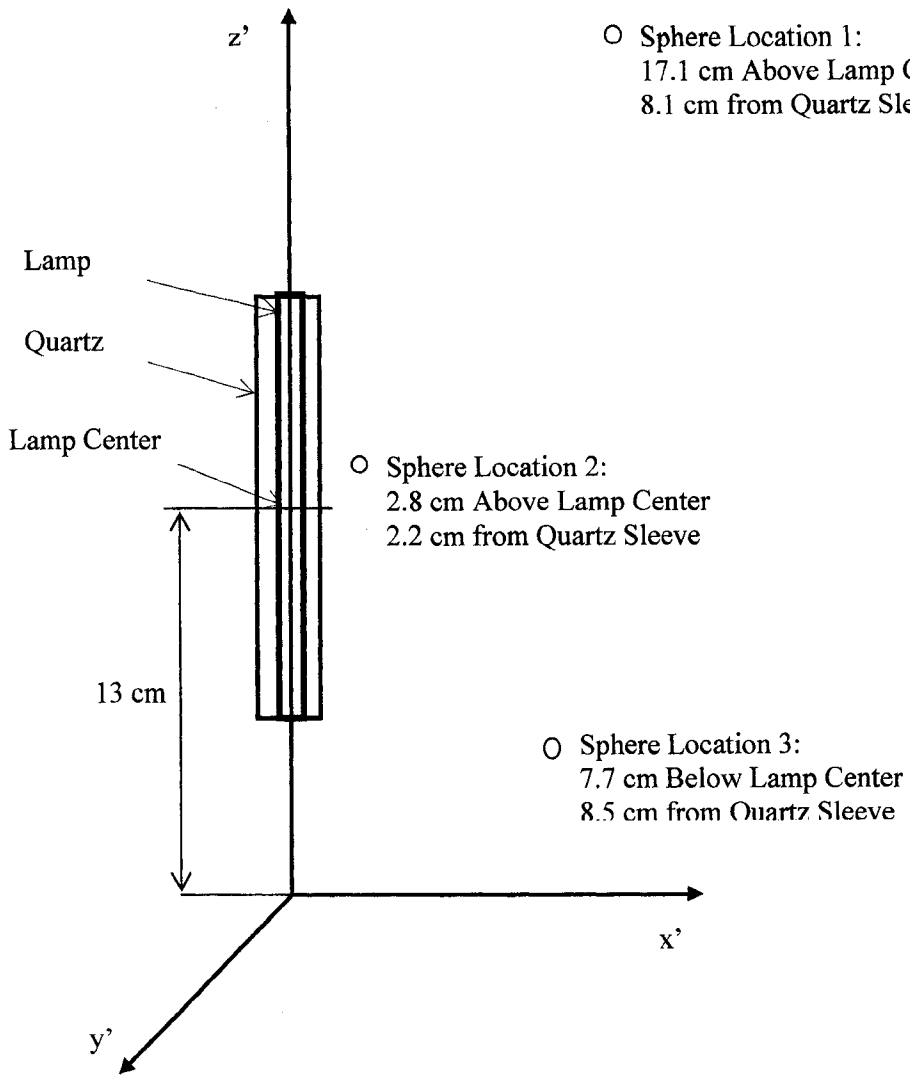

Figure 5-1. Coordinate System for MCRT Modeling Validation Based on Actinometric Testing

The radial coordinates in the x- and y- directions were calculated by adding the quartz sleeve radius (3.2 cm) to the horizontal distance data from the quartz sleeve shown in Tables 5-2 and 5-3 and then adding or subtracting the sum from 15 cm. The resulting radial coordinate values in the x- and y-directions represented the global coordinates of the lamp. Therefore, coordinates of the tested spheres listed in Tables 5-4 and 5-5 were

Table 5-4. Tested Sphere Locations and Equivalent Coordinates Used in MCRT Simulations – 100% UV Transmission Case

Vert. Dist. from Lamp Center Lamp Center (cm)	Hor. Dist. from Quartz Sleeve (cm)	Observed Experimental Fluence Rate (mW/cm^2)	MCRT Vertical Coordinate z (cm)	MCRT Radial Coordinates (x for y =15 cm or y for x = 15 cm) (cm)	
15.0	3.5	0.313	28.0	8.3	21.7
14.8	6.4	0.306	27.8	5.4	24.6
14.6	9.3	0.311	27.6	2.5	27.5
14.5	12.1	0.311	27.5	-0.3	30.3
11.5	7.4	0.654	24.5	4.4	25.6
11.5	13.1	0.429	24.5	-1.3	31.3
10.5	3.1	1.145	23.5	8.7	21.3
10.2	12.1	0.541	23.2	-0.3	30.3
10.1	10.1	0.654	23.1	1.7	28.3
6.7	4.1	2.455	19.7	7.7	22.3
7.8	6.9	1.208	20.8	4.9	25.1
6.8	10.1	0.957	19.8	1.7	28.3
7.0	12.0	0.757	20.0	-0.2	30.2
7.2	12.9	0.748	20.2	-1.1	31.1
4.4	6.9	1.835	17.4	4.9	25.1
3.6	9.5	1.292	16.6	2.3	27.7
3.6	12.0	0.964	16.6	-0.2	30.2
3.2	3.7	2.980	16.2	8.1	21.9
2.5	13.0	0.915	15.5	-1.2	31.2
-0.9	4.4	3.316	12.1	7.4	22.6
0.8	6.2	2.278	13.8	5.6	24.4
0.2	9.3	1.524	13.2	2.5	27.5
0.3	12.1	0.980	13.3	-0.3	30.3
-2.2	12.8	0.975	10.8	-1.0	31.0
-2.4	6.4	2.098	10.6	5.4	24.6
-3.0	9.5	1.415	10.0	2.3	27.7
-3.1	12.1	0.966	9.9	-0.3	30.3
-4.5	4.3	2.660	8.5	7.5	22.5
-6.3	6.4	1.647	6.7	5.4	24.6
-6.8	9.0	0.202	6.2	2.8	27.2
-6.3	11.7	0.865	6.7	0.1	29.9
-5.8	12.4	0.886	7.2	-0.6	30.6
-8.6	3.8	1.448	4.4	8.0	22.0
-9.1	13.0	0.603	3.9	-1.2	31.2
-9.6	11.3	0.645	3.4	0.5	29.5
-10.0	5.7	0.957	3.0	6.1	23.9
-10.0	8.9	0.806	3.0	2.9	27.1

Table 5-5. Tested Sphere Locations and Equivalent Coordinates Used In MCRT Simulations – 73% UV Transmission Case

Vertical Distance from Lamp Center Lamp Center (cm)	Horizontal Distance from Quartz Sleeve (cm)	Observed Experimental Fluence Rate (mW/cm^2)	MCRT Vertical Coordinate z (cm)	MCRT Radial Coordinates (x for y =15 cm or y for x = 15 cm) (cm)	
17.3	4.7	7.9	0.017	30.3	7.1
17.1	8.1	11.3	0.007	30.1	3.7
16.9	12.1	15.3	0.004	29.9	-0.3
16.8	11.6	14.8	0.004	29.8	0.2
15.8	2.4	5.6	0.387	28.8	9.4
14.2	8.4	11.6	0.018	27.2	3.4
13.6	5.2	8.4	0.065	26.6	6.6
12.6	12.5	15.7	0.009	25.6	-0.7
12.4	11.5	14.7	0.012	25.4	0.3
11.1	5.3	8.5	0.136	24.1	6.5
11.0	2.5	5.7	1.139	24.0	9.3
10.9	8.7	11.9	0.051	23.9	3.1
8.6	11.6	14.8	0.023	21.6	0.2
8.3	12.5	15.7	0.018	21.3	-0.7
7.2	5.7	8.9	0.369	20.2	6.1
7.0	8.5	11.7	0.103	20.0	3.3
6.9	2.2	5.4	1.501	19.9	9.6
4.7	11.6	14.8	0.035	17.7	0.2
3.6	5.4	8.6	0.527	16.6	6.4
3.2	8.8	12.0	0.132	16.2	3.0
3.0	12.6	15.8	0.023	16.0	-0.8
2.8	2.2	5.4	1.547	15.8	9.6
0.7	11.4	14.6	0.040	13.7	0.4
-0.1	8.9	12.1	0.133	12.9	2.9
-0.3	5.7	8.9	0.488	12.7	6.1
-1.0	2.3	5.5	1.356	12.0	9.5
-1.7	12.6	15.8	0.024	11.3	-0.8
-3.5	11.7	14.9	0.031	9.5	0.1
-3.6	5.6	8.8	0.422	9.4	6.2
-3.8	8.7	11.9	0.117	9.2	3.1
-5.6	2.3	5.5	0.884	7.4	9.5
-7.0	12.6	15.8	0.016	6.0	-0.8
-7.5	5.6	8.8	0.228	5.5	6.2
-7.5	11.3	14.5	0.022	5.5	0.5
-7.7	8.5	11.7	0.074	5.3	3.3
17.3	4.7	7.9	0.017	30.3	7.1
17.1	8.1	11.3	0.007	30.1	3.7

used as referenced locations to be compared with the corresponding MCRT simulation data. Detailed discussion of MCRT model estimate comparison and interpretation is provided later in this section.

In every MCRT simulation, fluence rates in all volume elements within the system were calculated. However, for point-to-point comparison and model validation purposes, fluence data along the x'- and y'- axis within typical sampling ranges shown in Figure 5-2 were chosen as representative data at each radial distance from the quartz sleeve. Thus, four data points for each radial distance, including two in each direction, were used for comparison purposes.

In generating simulation data for comparison with the measured fluence data, the MCRT model was executed with the number of bundles ranging from two million to six million. As discussed in Chapter 4, convergence of simulated fluence data was obtained when the number of bundles exceeded 750,000. At least two million bundles were simulated for each run to ensure the convergence of fluence data. The higher number of bundles were arbitrarily chosen to obtain additional data; however, values of data obtained in this range were essentially the same.

For each vertical and radial location of the tested sphere, 20 MCRT simulation data points including four samples in each run were used for comparison purposes. These data are listed in Tables 5-6 and 5-7 for the cases with 100 percent and 73 percent UV transmission water, respectively. The observed experimental fluence rate data and their corresponding locations in accordance with the MCRT simulation coordinates are also listed in Tables 5-6 and 5-7 for comparison purposes.

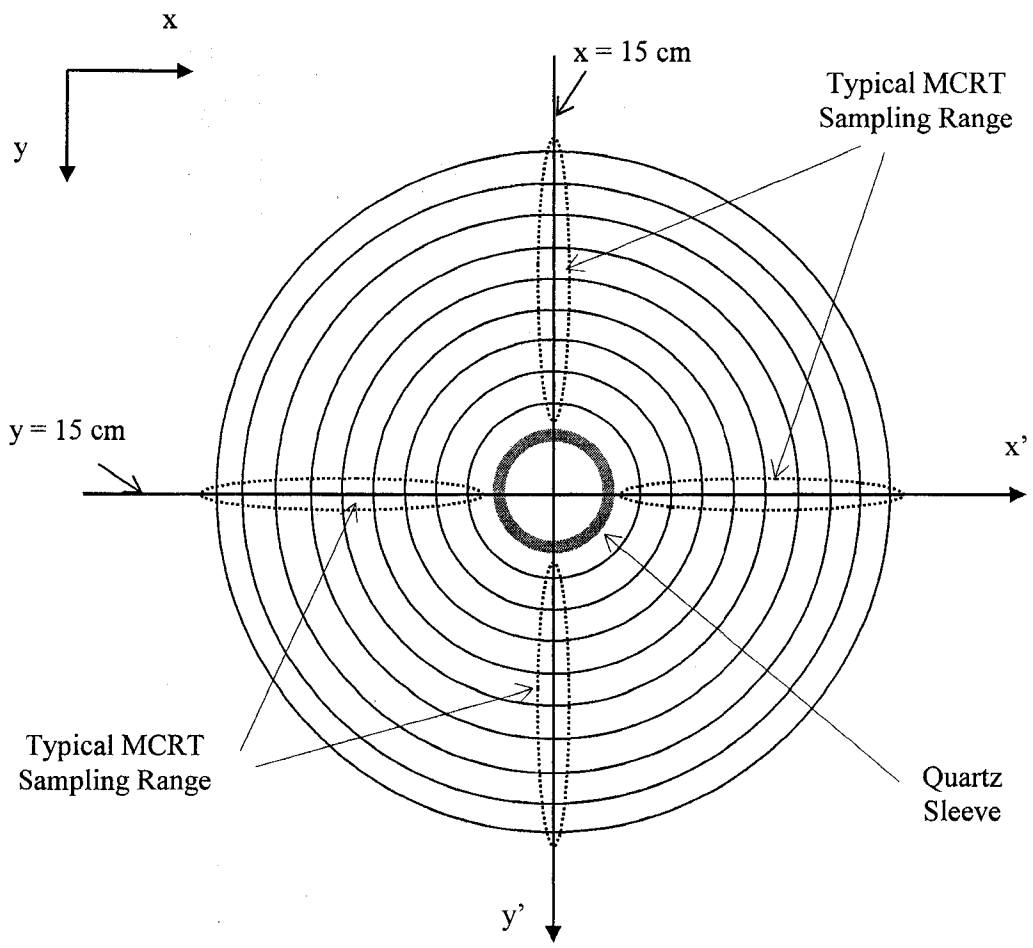

Figure 5-2. Typical Sampling Ranges of MCRT Simulation Data Used in Validation and Comparison

In Tables 5-6 and 5-7, each MCRT fluence rate data point represents the radial location of x or y within the sampling range identified in Figure 5-2. These coordinates correspond to y equal to 15 cm or x equal to 15 cm, respectively.

Table 5-6. Listing of Observed Experimental Data and Estimated MCRT Model Data – 100 % UV Transmission Case

Two-Million Bundle Simulation

Observed Experimental Fluence Rate (mW/cm^2)	Vertical Coord. (z) (cm)	Radial Coord. (x or y) (cm)	Radial Coord. (x or y) (cm)	Estimated MCRT Fluence Rate (mW/cm^2)			
0.313	28.0	8.3	21.7	0.102	0.800	0.421	0.328
0.306	27.8	5.4	24.6	0.285	0.404	0.491	0.515
0.311	27.6	2.5	27.5	0.138	0.318	0.490	0.249
0.311	27.5	-0.3	30.3	0.121	0.435	0.230	0.465
0.654	24.5	4.4	25.6	0.512	0.221	0.885	0.842
0.429	24.5	-1.3	31.3	0.459	0.187	0.556	0.528
1.145	23.5	8.7	21.3	1.251	0.587	2.005	2.082
0.541	23.2	-0.3	30.3	0.478	0.200	0.613	0.644
0.654	23.1	1.7	28.3	0.543	0.211	0.787	0.732
2.455	19.7	7.7	22.3	1.497	0.788	2.266	2.227
1.208	20.8	4.9	25.1	0.867	0.417	1.332	1.304
0.957	19.8	1.7	28.3	0.741	0.361	0.980	0.944
0.757	20.0	-0.2	30.2	0.600	0.307	0.748	0.722
0.748	20.2	-1.1	31.1	0.600	0.307	0.726	0.658
1.835	17.4	4.9	25.1	1.243	0.712	1.586	1.632
1.292	16.6	2.3	27.7	0.927	0.605	1.174	1.209
0.964	16.6	-0.2	30.2	0.729	0.499	0.807	0.825
2.980	16.2	8.1	21.9	2.323	1.670	3.303	3.364
0.915	15.5	-1.2	31.2	0.837	0.611	0.823	0.766
3.316	12.1	7.4	22.6	2.097	1.593	2.637	2.095
2.278	13.8	5.6	24.4	1.554	1.188	1.958	1.956
1.524	13.2	2.5	27.5	1.037	0.732	1.286	1.247
0.980	13.3	-0.3	30.3	0.832	0.611	0.906	0.882
0.975	10.8	-1.0	31.0	0.828	0.668	0.749	0.750
2.098	10.6	5.4	24.6	1.461	1.213	1.769	1.785
1.415	10.0	2.3	27.7	0.995	0.945	0.787	1.158
0.966	9.9	-0.3	30.3	0.723	0.632	0.806	0.820
2.660	8.5	7.5	22.5	1.771	1.583	2.138	2.154
1.647	6.7	5.4	24.6	1.246	1.119	1.448	1.390
0.202	6.2	2.8	27.2	0.860	0.772	0.948	0.966
0.865	6.7	0.1	29.9	0.730	0.626	0.780	0.803
0.886	7.2	-0.6	30.6	0.761	0.690	0.720	0.748
1.448	4.4	8.0	22.0	1.055	1.046	1.059	1.030
0.603	3.9	-1.2	31.2	0.547	0.556	0.513	0.464
0.645	3.4	0.5	29.5	0.547	0.556	0.547	0.529
0.957	3.0	6.1	23.9	0.715	0.691	0.650	0.605
0.806	3.0	2.9	27.1	0.613	0.573	0.632	0.648

Table 5-6 (Continued)

Three-Million Bundle Simulation

Observed Experimental Fluence Rate (mW/cm^2)	Vertical Coord. (z) (cm)	Radial Coord. (x or y) (cm)	Radial Coord. (x or y) (cm)	Estimated MCRT Fluence Rate (mW/cm^2)			
0.313	28.0	8.3	21.7	0.088	0.310	0.188	0.327
0.306	27.8	5.4	24.6	0.289	0.293	0.358	0.536
0.311	27.6	2.5	27.5	0.302	0.503	0.514	0.126
0.311	27.5	-0.3	30.3	0.277	0.094	0.202	0.196
0.654	24.5	4.4	25.6	0.506	0.231	0.221	0.842
0.429	24.5	-1.3	31.3	0.388	0.181	0.550	0.582
1.145	23.5	8.7	21.3	0.625	0.277	1.057	1.001
0.541	23.2	-0.3	30.3	0.462	0.213	0.681	0.638
0.654	23.1	1.7	28.3	0.516	0.223	0.744	0.776
2.455	19.7	7.7	22.3	1.541	0.836	2.299	2.257
1.208	20.8	4.9	25.1	0.958	0.389	1.350	1.354
0.957	19.8	1.7	28.3	0.733	0.378	0.967	0.962
0.757	20.0	-0.2	30.2	0.612	0.259	0.736	0.744
0.748	20.2	-1.1	31.1	0.612	0.259	0.651	0.652
1.835	17.4	4.9	25.1	1.139	0.670	1.574	1.543
1.292	16.6	2.3	27.7	0.961	0.596	1.203	1.201
0.964	16.6	-0.2	30.2	0.772	0.444	0.846	0.854
2.980	16.2	8.1	21.9	2.366	1.640	3.266	3.314
0.915	15.5	-1.2	31.2	0.895	0.597	0.791	0.715
3.316	12.1	7.4	22.6	2.041	1.651	2.822	1.050
2.278	13.8	5.6	24.4	1.558	1.100	2.002	0.726
1.524	13.2	2.5	27.5	1.013	0.781	1.272	1.250
0.980	13.3	-0.3	30.3	0.797	0.619	0.878	0.863
0.975	10.8	-1.0	31.0	0.843	0.706	0.720	0.755
2.098	10.6	5.4	24.6	1.462	1.198	1.804	1.836
1.415	10.0	2.3	27.7	1.039	0.855	1.190	1.189
0.966	9.9	-0.3	30.3	0.786	0.663	0.796	0.819
2.660	8.5	7.5	22.5	1.852	1.565	2.151	2.117
1.647	6.7	5.4	24.6	1.285	1.139	1.375	1.405
0.202	6.2	2.8	27.2	0.933	0.768	0.963	0.970
0.865	6.7	0.1	29.9	0.764	2.431	0.808	0.811
0.886	7.2	-0.6	30.6	0.760	0.643	0.734	0.753
1.448	4.4	8.0	22.0	1.027	0.973	1.032	1.070
0.603	3.9	-1.2	31.2	0.539	0.501	0.535	0.512
0.645	3.4	0.5	29.5	0.539	0.501	0.592	0.563
0.957	3.0	6.1	23.9	0.663	0.680	0.603	0.680
0.806	3.0	2.9	27.1	0.600	0.572	0.636	0.568

Table 5-6 (Continued)

Four-Million Bundle Simulation

Observed Experimental Fluence Rate (mW/cm^2)	Vertical Coord. (z) (cm)	Radial Coord. (x or y) (cm)	Radial Coord. (x or y) (cm)	Estimated MCRT Fluence Rate (mW/cm^2)			
0.313	28.0	8.3	21.7	0.293	0.303	0.312	0.216
0.306	27.8	5.4	24.6	0.287	0.379	0.415	0.261
0.311	27.6	2.5	27.5	0.313	0.124	0.495	0.486
0.311	27.5	-0.3	30.3	0.313	0.124	0.442	0.464
0.654	24.5	4.4	25.6	0.504	0.208	0.530	0.866
0.429	24.5	-1.3	31.3	0.396	0.188	0.554	0.866
1.145	23.5	8.7	21.3	0.627	0.273	1.070	0.542
0.541	23.2	-0.3	30.3	0.491	0.187	0.626	0.646
0.654	23.1	1.7	28.3	0.483	0.206	0.775	0.752
2.455	19.7	7.7	22.3	1.487	0.854	2.231	2.191
1.208	20.8	4.9	25.1	0.907	0.459	1.316	1.317
0.957	19.8	1.7	28.3	0.714	0.345	0.948	0.966
0.757	20.0	-0.2	30.2	0.596	0.283	0.776	0.746
0.748	20.2	-1.1	31.1	0.596	0.283	0.693	0.673
1.835	17.4	4.9	25.1	1.148	0.703	1.594	1.534
1.292	16.6	2.3	27.7	0.955	0.574	1.231	1.194
0.964	16.6	-0.2	30.2	0.759	0.454	0.853	0.812
2.980	16.2	8.1	21.9	2.349	1.622	3.354	3.312
0.915	15.5	-1.2	31.2	0.890	0.567	0.762	0.777
3.316	12.1	7.4	22.6	2.152	1.671	2.640	1.043
2.278	13.8	5.6	24.4	1.569	1.133	1.940	1.924
1.524	13.2	2.5	27.5	1.055	0.768	1.200	1.255
0.980	13.3	-0.3	30.3	0.843	0.612	0.835	0.888
0.975	10.8	-1.0	31.0	0.791	0.657	0.742	0.753
2.098	10.6	5.4	24.6	1.482	1.244	1.817	1.780
1.415	10.0	2.3	27.7	1.028	0.867	1.238	1.194
0.966	9.9	-0.3	30.3	0.807	0.687	0.864	0.831
2.660	8.5	7.5	22.5	1.779	1.639	2.143	2.214
1.647	6.7	5.4	24.6	1.186	1.135	1.357	1.342
0.202	6.2	2.8	27.2	0.862	0.829	0.957	0.927
0.865	6.7	0.1	29.9	0.708	0.710	0.743	0.783
0.886	7.2	-0.6	30.6	0.753	0.689	0.740	0.791
1.448	4.4	8.0	22.0	1.053	1.023	1.034	1.018
0.603	3.9	-1.2	31.2	0.523	0.504	0.519	0.474
0.645	3.4	0.5	29.5	0.474	0.524	0.584	0.562
0.957	3.0	6.1	23.9	0.684	0.679	0.669	0.624
0.806	3.0	2.9	27.1	0.609	0.605	0.647	0.614

Table 5-6 (Continued)

Five-Million Bundle Simulation

Observed Experimental Fluence Rate (mW/cm^2)	Vertical Coord. (z) (cm)	Radial Coord. (x or y) (cm)	Radial Coord. (x or y) (cm)	Estimated MCRT Fluence Rate (mW/cm^2)			
0.313	28.0	8.3	21.7	0.314	0.314	0.224	0.308
0.306	27.8	5.4	24.6	0.276	0.377	0.502	0.288
0.311	27.6	2.5	27.5	0.290	0.120	0.471	0.508
0.311	27.5	-0.3	30.3	0.296	0.129	0.282	0.282
0.654	24.5	4.4	25.6	0.527	0.252	0.835	0.866
0.429	24.5	-1.3	31.3	0.401	0.561	0.179	0.545
1.145	23.5	8.7	21.3	0.838	0.384	1.362	1.362
0.541	23.2	-0.3	30.3	0.491	0.222	0.652	0.639
0.654	23.1	1.7	28.3	0.548	0.214	0.766	0.767
2.455	19.7	7.7	22.3	1.511	0.816	2.225	2.302
1.208	20.8	4.9	25.1	0.903	0.426	1.320	1.329
0.957	19.8	1.7	28.3	0.692	0.353	0.965	1.019
0.757	20.0	-0.2	30.2	0.591	0.263	0.743	0.796
0.748	20.2	-1.1	31.1	0.591	0.263	0.673	0.796
1.835	17.4	4.9	25.1	1.137	0.670	1.558	1.566
1.292	16.6	2.3	27.7	0.968	0.631	1.242	1.195
0.964	16.6	-0.2	30.2	0.749	0.488	0.838	0.847
2.980	16.2	8.1	21.9	2.396	1.625	3.345	3.360
0.915	15.5	-1.2	31.2	0.821	0.596	0.776	0.803
3.316	12.1	7.4	22.6	2.139	1.673	2.690	2.728
2.278	13.8	5.6	24.4	1.517	1.161	1.957	1.989
1.524	13.2	2.5	27.5	1.028	0.764	1.271	1.273
0.980	13.3	-0.3	30.3	0.810	0.573	0.869	0.863
0.975	10.8	-1.0	31.0	0.812	0.683	0.745	0.773
2.098	10.6	5.4	24.6	1.510	1.213	1.772	1.860
1.415	10.0	2.3	27.7	1.056	0.830	1.179	1.206
0.966	9.9	-0.3	30.3	0.798	0.672	0.844	0.792
2.660	8.5	7.5	22.5	1.809	1.598	2.194	2.190
1.647	6.7	5.4	24.6	1.217	1.131	1.388	1.308
0.202	6.2	2.8	27.2	0.875	0.813	0.957	0.936
0.865	6.7	0.1	29.9	0.748	0.694	0.773	0.748
0.886	7.2	-0.6	30.6	0.778	0.713	0.737	0.768
1.448	4.4	8.0	22.0	1.026	1.074	1.033	1.056
0.603	3.9	-1.2	31.2	0.524	0.524	0.531	0.494
0.645	3.4	0.5	29.5	0.524	0.524	0.582	0.564
0.957	3.0	6.1	23.9	0.688	0.687	0.624	0.666
0.806	3.0	2.9	27.1	0.625	0.596	0.666	0.639

Table 5-6 (Continued)

Six-Million Bundle Simulation

Observed Experimental Fluence Rate (mW/cm^2)	Vertical Coord. (z) (cm)	Radial Coord. (x or y) (cm)	Radial Coord. (x or y) (cm)	Estimated MCRT Fluence Rate (mW/cm^2)			
0.313	28.0	8.3	21.7	0.298	0.347	0.312	0.223
0.306	27.8	5.4	24.6	0.300	0.390	0.474	0.508
0.311	27.6	2.5	27.5	0.299	0.140	0.495	0.497
0.311	27.5	-0.3	30.3	0.273	0.130	0.447	0.449
0.654	24.5	4.4	25.6	0.501	0.220	0.820	0.378
0.429	24.5	-1.3	31.3	0.430	0.168	0.566	0.570
1.145	23.5	8.7	21.3	0.811	0.367	1.348	1.337
0.541	23.2	-0.3	30.3	0.473	0.201	0.663	0.646
0.654	23.1	1.7	28.3	0.517	0.204	0.773	0.781
2.455	19.7	7.7	22.3	1.517	0.835	2.281	2.252
1.208	20.8	4.9	25.1	0.904	0.421	1.312	1.288
0.957	19.8	1.7	28.3	0.716	0.344	0.992	0.985
0.757	20.0	-0.2	30.2	0.621	0.265	0.767	0.772
0.748	20.2	-1.1	31.1	0.621	0.265	0.707	0.706
1.835	17.4	4.9	25.1	1.166	0.689	1.600	1.519
1.292	16.6	2.3	27.7	0.934	0.609	1.255	1.281
0.964	16.6	-0.2	30.2	0.758	0.469	0.858	0.838
2.980	16.2	8.1	21.9	2.367	1.589	3.336	3.292
0.915	15.5	-1.2	31.2	0.882	0.583	0.768	0.790
3.316	12.1	7.4	22.6	2.143	1.634	2.730	2.753
2.278	13.8	5.6	24.4	1.566	1.156	1.943	1.995
1.524	13.2	2.5	27.5	0.996	0.774	1.235	1.263
0.980	13.3	-0.3	30.3	0.790	0.635	0.855	0.891
0.975	10.8	-1.0	31.0	0.828	0.668	0.749	0.750
2.098	10.6	5.4	24.6	1.499	1.220	1.783	1.778
1.415	10.0	2.3	27.7	1.014	0.843	1.183	1.197
0.966	9.9	-0.3	30.3	0.786	0.674	0.829	0.806
2.660	8.5	7.5	22.5	1.834	1.593	2.201	2.129
1.647	6.7	5.4	24.6	1.201	1.174	1.382	1.371
0.202	6.2	2.8	27.2	0.879	0.833	0.957	0.972
0.865	6.7	0.1	29.9	0.711	0.684	0.792	0.792
0.886	7.2	-0.6	30.6	0.770	0.710	0.752	0.779
1.448	4.4	8.0	22.0	1.045	1.043	1.040	1.046
0.603	3.9	-1.2	31.2	0.539	0.520	0.532	0.486
0.645	3.4	0.5	29.5	0.539	0.520	0.568	0.564
0.957	3.0	6.1	23.9	0.656	0.655	0.620	0.651
0.806	3.0	2.9	27.1	0.611	0.594	0.614	0.622

Table 5-7. Listing of Observed Experimental Data and Estimated MCRT Data – 73 % UV Transmission Case

Two-Million Bundle Simulation

Observed Experimental Fluence Rate (mW/cm^2)	Vertical Coord. (z) (cm)	Radial Coord. (x or y) (cm)	Radial Coord. (x or y) (cm)	Estimated MCRT Fluence Rate (mW/cm^2)			
0.017	30.3	7.1	22.9	0.049	0.027	0.075	0.083
0.007	30.1	3.7	26.3	0.034	0.016	0.065	0.063
0.004	29.9	-0.3	30.3	0.031	0.014	0.078	0.045
0.004	29.8	0.2	29.8	0.031	0.014	0.048	0.055
0.387	28.8	9.4	20.6	0.104	0.050	0.171	0.172
0.018	27.2	3.4	26.6	0.075	0.035	0.122	0.124
0.065	26.6	6.6	23.4	0.139	0.070	0.254	0.258
0.009	25.6	-0.7	30.7	0.066	0.030	0.088	0.081
0.012	25.4	0.3	29.7	0.066	0.030	0.108	0.095
0.136	24.1	6.5	23.5	0.230	0.109	0.418	0.414
1.139	24.0	9.3	20.7	0.416	0.218	0.748	0.762
0.051	23.9	3.1	26.9	0.151	0.072	0.248	0.255
0.023	21.6	0.2	29.8	0.096	0.049	0.153	0.156
0.018	21.3	-0.7	30.7	0.096	0.049	0.049	0.125
0.369	20.2	6.1	23.9	0.521	0.229	0.808	0.841
0.103	20.0	3.3	26.7	0.229	0.101	0.360	0.344
1.501	19.9	9.6	20.4	1.500	0.822	2.490	2.559
0.035	17.7	0.2	29.8	0.134	0.078	0.198	0.199
0.527	16.6	6.4	23.6	0.712	0.497	1.081	0.268
0.132	16.2	3.0	27.0	0.314	0.213	0.346	0.337
0.023	16.0	-0.8	30.8	0.142	0.096	0.160	0.154
1.547	15.8	9.6	20.4	1.967	1.512	3.248	3.322
0.040	13.7	0.4	29.6	0.153	0.115	0.211	0.202
0.133	12.9	2.9	27.1	0.262	0.193	0.341	0.333
0.488	12.7	6.1	23.9	0.791	0.583	0.834	1.105
1.356	12.0	9.5	20.5	2.054	1.556	3.162	3.034
0.024	11.3	-0.8	30.8	0.161	0.119	0.155	0.155
0.031	9.5	0.1	29.9	0.144	0.129	0.187	0.191
0.422	9.4	6.2	23.8	0.713	0.585	0.967	0.983
0.117	9.2	3.1	26.9	0.312	0.268	0.420	0.414
0.884	7.4	9.5	20.5	1.526	1.382	2.229	2.230
0.016	6.0	-0.8	30.8	0.024	0.129	0.135	0.121
0.228	5.5	6.2	23.8	0.495	0.497	0.643	0.648
0.022	5.5	0.5	29.5	0.107	0.115	0.150	0.145
0.074	5.3	3.3	26.7	0.238	0.249	0.307	0.297
0.017	30.3	7.1	22.9	0.049	0.027	0.075	0.083
0.007	30.1	3.7	26.3	0.034	0.016	0.065	0.063

Table 5-7 (Continued)

Three-Million Bundle Simulation

Observed Experimental Fluence Rate (mW/cm^2)	Vertical Coord. (z) (cm)	Radial Coord. (x or y) (cm)	Radial Coord. (x or y) (cm)	Estimated MCRT Fluence Rate (mW/cm^2)			
0.017	30.3	7.1	22.9	0.047	0.023	0.082	0.080
0.007	30.1	3.7	26.3	0.036	0.018	0.064	0.063
0.004	29.9	-0.3	30.3	0.029	0.013	0.046	0.046
0.004	29.8	0.2	29.8	0.029	0.013	0.059	0.053
0.387	28.8	9.4	20.6	0.095	0.053	0.189	0.177
0.018	27.2	3.4	26.6	0.066	0.033	0.135	0.121
0.065	26.6	6.6	23.4	0.137	0.067	0.250	0.256
0.009	25.6	-0.7	30.7	0.016	0.026	0.081	0.085
0.012	25.4	0.3	29.7	0.016	0.026	0.104	0.100
0.136	24.1	6.5	23.5	0.231	0.102	0.428	0.409
1.139	24.0	9.3	20.7	0.404	0.218	0.741	0.732
0.051	23.9	3.1	26.9	0.153	0.065	0.251	0.271
0.023	21.6	0.2	29.8	0.099	0.045	0.158	0.168
0.018	21.3	-0.7	30.7	0.099	0.045	0.124	0.131
0.369	20.2	6.1	23.9	0.505	0.232	0.823	0.838
0.103	20.0	3.3	26.7	0.226	0.106	0.347	0.375
1.501	19.9	9.6	20.4	1.499	0.845	2.521	2.555
0.035	17.7	0.2	29.8	0.180	0.078	0.200	0.191
0.527	16.6	6.4	23.6	0.755	0.497	1.107	1.135
0.132	16.2	3.0	27.0	0.250	0.198	0.350	0.352
0.023	16.0	-0.8	30.8	0.147	0.093	0.164	0.169
1.547	15.8	9.6	20.4	2.087	1.445	3.268	3.239
0.040	13.7	0.4	29.6	0.155	0.102	0.273	0.216
0.133	12.9	2.9	27.1	0.259	0.191	0.369	0.351
0.488	12.7	6.1	23.9	0.759	0.603	1.092	1.132
1.356	12.0	9.5	20.5	0.000	1.575	3.125	3.164
0.024	11.3	-0.8	30.8	0.150	0.120	0.160	0.154
0.031	9.5	0.1	29.9	0.147	0.123	0.156	0.190
0.422	9.4	6.2	23.8	0.717	0.569	0.996	0.946
0.117	9.2	3.1	26.9	0.318	0.266	0.426	0.416
0.884	7.4	9.5	20.5	1.589	1.401	2.260	2.136
0.016	6.0	-0.8	30.8	0.127	0.129	0.134	0.120
0.228	5.5	6.2	23.8	0.521	0.498	0.674	0.673
0.022	5.5	0.5	29.5	0.120	0.118	0.143	0.149
0.074	5.3	3.3	26.7	0.247	0.239	0.304	0.312
0.017	30.3	7.1	22.9	0.047	0.023	0.082	0.080
0.007	30.1	3.7	26.3	0.036	0.018	0.064	0.063

Table 5-7 (Continued)

Four-Million Bundle Simulation

Observed Experimental Fluence Rate (mW/cm^2)	Vertical Coord. (z) (cm)	Radial Coord. (x or y) (cm)	Radial Coord. (x or y) (cm)	Estimated MCRT Fluence Rate (mW/cm^2)			
0.017	30.3	7.1	22.9	0.044	0.025	0.080	0.086
0.007	30.1	3.7	26.3	0.035	0.018	0.065	0.066
0.004	29.9	-0.3	30.3	0.031	0.014	0.049	0.047
0.004	29.8	0.2	29.8	0.031	0.014	0.057	0.052
0.387	28.8	9.4	20.6	0.089	0.054	0.174	0.183
0.018	27.2	3.4	26.6	0.094	0.039	0.156	0.154
0.065	26.6	6.6	23.4	0.150	0.065	0.260	0.253
0.009	25.6	-0.7	30.7	0.063	0.027	0.081	0.085
0.012	25.4	0.3	29.7	0.063	0.027	0.101	0.103
0.136	24.1	6.5	23.5	0.248	0.107	0.427	0.401
1.139	24.0	9.3	20.7	0.423	0.202	0.774	0.746
0.051	23.9	3.1	26.9	0.158	0.068	0.255	0.251
0.023	21.6	0.2	29.8	0.105	0.042	0.149	0.162
0.018	21.3	-0.7	30.7	0.105	0.042	0.117	0.128
0.369	20.2	6.1	23.9	0.507	0.233	0.798	0.815
0.103	20.0	3.3	26.7	0.244	0.105	0.340	0.379
1.501	19.9	9.6	20.4	1.474	0.823	2.498	2.499
0.035	17.7	0.2	29.8	0.129	0.077	0.201	0.197
0.527	16.6	6.4	23.6	0.728	0.491	1.111	1.139
0.132	16.2	3.0	27.0	0.288	0.201	0.335	0.356
0.023	16.0	-0.8	30.8	0.144	0.095	0.157	0.172
1.547	15.8	9.6	20.4	2.013	1.391	3.257	3.235
0.040	13.7	0.4	29.6	0.153	0.115	0.219	0.213
0.133	12.9	2.9	27.1	0.261	0.200	0.349	0.352
0.488	12.7	6.1	23.9	0.783	0.603	1.122	1.166
1.356	12.0	9.5	20.5	1.983	1.575	3.176	3.098
0.024	11.3	-0.8	30.8	0.156	0.117	0.158	0.160
0.031	9.5	0.1	29.9	0.148	0.123	0.183	0.187
0.422	9.4	6.2	23.8	0.729	0.572	0.955	0.239
0.117	9.2	3.1	26.9	0.306	0.250	0.410	0.406
0.884	7.4	9.5	20.5	1.571	1.414	2.171	2.210
0.016	6.0	-0.8	30.8	0.126	0.118	0.127	0.124
0.228	5.5	6.2	23.8	0.516	0.531	0.661	0.689
0.022	5.5	0.5	29.5	0.117	0.119	0.142	0.153
0.074	5.3	3.3	26.7	0.248	0.238	0.305	0.306
0.017	30.3	7.1	22.9	0.044	0.025	0.080	0.086
0.007	30.1	3.7	26.3	0.035	0.018	0.065	0.066

Table 5-7 (Continued)

Five-Million Bundle Simulation

Observed Experimental Fluence Rate (mW/cm^2)	Vertical Coord. (z) (cm)	Radial Coord. (x or y) (cm)	Radial Coord. (x or y) (cm)	Estimated MCRT Fluence Rate (mW/cm^2)			
0.017	30.3	7.1	22.9	0.046	0.024	0.081	0.082
0.007	30.1	3.7	26.3	0.035	0.020	0.066	0.065
0.004	29.9	-0.3	30.3	0.031	0.015	0.058	0.049
0.004	29.8	0.2	29.8	0.031	0.015	0.058	0.058
0.387	28.8	9.4	20.6	0.095	0.052	0.169	0.176
0.018	27.2	3.4	26.6	0.069	0.034	0.132	0.135
0.065	26.6	6.6	23.4	0.146	0.064	0.255	0.271
0.009	25.6	-0.7	30.7	0.057	0.057	0.087	0.089
0.012	25.4	0.3	29.7	0.057	0.028	0.102	0.108
0.136	24.1	6.5	23.5	0.238	0.106	0.422	0.417
1.139	24.0	9.3	20.7	0.413	0.217	0.760	0.780
0.051	23.9	3.1	26.9	0.145	0.067	0.255	0.261
0.023	21.6	0.2	29.8	0.096	0.044	0.152	0.160
0.018	21.3	-0.7	30.7	0.096	0.044	0.119	0.124
0.369	20.2	6.1	23.9	0.485	0.237	0.832	0.832
0.103	20.0	3.3	26.7	0.225	0.106	0.354	0.356
1.501	19.9	9.6	20.4	1.424	0.835	2.482	2.527
0.035	17.7	0.2	29.8	0.136	0.086	0.199	0.195
0.527	16.6	6.4	23.6	0.752	0.474	1.120	1.117
0.132	16.2	3.0	27.0	0.315	0.193	0.343	0.365
0.023	16.0	-0.8	30.8	0.140	0.084	0.164	0.155
1.547	15.8	9.6	20.4	2.035	1.425	3.222	3.266
0.040	13.7	0.4	29.6	0.154	0.120	0.199	0.208
0.133	12.9	2.9	27.1	0.253	0.200	0.349	0.349
0.488	12.7	6.1	23.9	0.769	0.601	1.109	1.139
1.356	12.0	9.5	20.5	2.105	1.545	3.127	3.153
0.024	11.3	-0.8	30.8	0.154	0.123	0.157	0.162
0.031	9.5	0.1	29.9	0.149	0.118	0.193	0.192
0.422	9.4	6.2	23.8	0.723	0.585	0.962	0.248
0.117	9.2	3.1	26.9	0.312	0.262	0.412	0.407
0.884	7.4	9.5	20.5	1.575	1.389	2.177	2.215
0.016	6.0	-0.8	30.8	0.129	0.123	0.129	0.122
0.228	5.5	6.2	23.8	0.507	0.510	0.658	0.650
0.022	5.5	0.5	29.5	0.121	0.117	0.147	0.153
0.074	5.3	3.3	26.7	0.251	0.238	0.318	0.068
0.017	30.3	7.1	22.9	0.046	0.024	0.081	0.082
0.007	30.1	3.7	26.3	0.035	0.020	0.066	0.065

Table 5-7 (Continued)

Six-Million Bundle Simulation

Observed Experimental Fluence Rate (mW/cm^2)	Vertical Coord. (z) (cm)	Radial Coord. (x or y) (cm)	Radial Coord. (x or y) (cm)	Estimated MCRT Fluence Rate (mW/cm^2)			
0.017	30.3	7.1	22.9	0.044	0.024	0.093	0.087
0.007	30.1	3.7	26.3	0.035	0.018	0.067	0.067
0.004	29.9	-0.3	30.3	0.028	0.017	0.051	0.046
0.004	29.8	0.2	29.8	0.028	0.017	0.059	0.055
0.387	28.8	9.4	20.6	0.100	0.059	0.193	0.182
0.018	27.2	3.4	26.6	0.070	0.031	0.136	0.125
0.065	26.6	6.6	23.4	0.140	0.069	0.265	0.260
0.009	25.6	-0.7	30.7	0.060	0.026	0.085	0.087
0.012	25.4	0.3	29.7	0.060	0.026	0.104	0.109
0.136	24.1	6.5	23.5	0.241	0.097	0.426	0.426
1.139	24.0	9.3	20.7	0.421	0.207	0.770	0.755
0.051	23.9	3.1	26.9	0.149	0.068	0.256	0.253
0.023	21.6	0.2	29.8	0.108	0.043	0.156	0.157
0.018	21.3	-0.7	30.7	0.108	0.043	0.121	0.126
0.369	20.2	6.1	23.9	0.520	0.231	0.799	0.824
0.103	20.0	3.3	26.7	0.232	0.101	0.361	0.356
1.501	19.9	9.6	20.4	1.483	0.826	2.487	2.534
0.035	17.7	0.2	29.8	0.135	0.076	0.199	0.198
0.527	16.6	6.4	23.6	0.724	0.496	1.137	1.120
0.132	16.2	3.0	27.0	0.301	0.197	0.347	0.352
0.023	16.0	-0.8	30.8	0.142	0.088	0.158	0.162
1.547	15.8	9.6	20.4	2.033	1.472	3.237	3.273
0.040	13.7	0.4	29.6	0.159	0.116	0.216	0.210
0.133	12.9	2.9	27.1	0.256	0.199	0.358	0.352
0.488	12.7	6.1	23.9	0.773	0.580	1.137	0.271
1.356	12.0	9.5	20.5	2.069	1.557	3.161	3.164
0.024	11.3	-0.8	30.8	0.156	0.126	0.158	0.156
0.031	9.5	0.1	29.9	0.050	0.125	0.194	0.192
0.422	9.4	6.2	23.8	0.705	0.585	0.993	0.231
0.117	9.2	3.1	26.9	0.302	0.266	0.409	0.403
0.884	7.4	9.5	20.5	1.525	1.346	2.167	2.189
0.016	6.0	-0.8	30.8	0.049	0.116	0.128	0.126
0.228	5.5	6.2	23.8	0.509	0.507	0.680	0.651
0.022	5.5	0.5	29.5	0.118	0.117	0.147	0.145
0.074	5.3	3.3	26.7	0.237	0.239	0.297	0.295
0.017	30.3	7.1	22.9	0.044	0.024	0.093	0.087
0.007	30.1	3.7	26.3	0.035	0.018	0.067	0.067

The observed experimental fluence rate data and the estimated MCRT model data are summarized in Tables 5-8 and 5-9 for both cases with 100 percent and 73 percent UV transmission. Since MCRT model simulated and calculated fluence rates in all volume elements within the system, estimated MCRT model fluence rate data were averaged values at the matching locations referenced in observed experimental data so that a point-to-point comparison could be made.

These point-to-point comparative data relative to the quartz sleeve surfaces, radial distances from 0 to 5 cm, 5 to 8 cm, 8 to 12 cm, and 10 to 13.5 cm (for the 100 percent UV transmission case) and from 0 to 5 cm, 5 to 6 cm, 8 to 9 cm, 11 to 12 cm, and 12 to 13 cm (for the 73 percent UV transmission case) are plotted in Figures 5-3 through 5-11, respectively. These specific radial distances were originally determined in the study by Rahn *et al.* (2000). Data for the 100 percent UV transmission case were illustrated in Figures 5-3 through 5-6. As indicated in these figures, the estimated MCRT fluence rates were slightly lower than, but very close to, the corresponding observed experimental data, particularly in the first 3 cm from the quartz sleeve surface. Data for the 73 percent UV transmission case were illustrated in Figures 5-7 through 5-11. These figures indicate that the MCRT fluence rates were slightly higher than, but were still close to, the corresponding experimental data, particularly in the first few centimeters from the quartz sleeve surface. The results suggested a reasonally good agreement between the observed experimental data and the estimated MCRT fluence rate data.

Table 5-8. Summary of Observed vs. Estimated Fluence Rate Data for Water with 100% UV Transmission

Vertical Distance from Lamp Center (cm)	Horizontal Distance from Quartz Sleeve (cm)	Observed Fluence Rate (mW/cm^2)	Estimated Fluence Rate (mW/cm^2)	Difference wrt Observed Fluence Rate (mW/cm^2)
10.5	3.1	1.145	0.960	- 0.185
15	3.5	0.313	0.301	- 0.012
3.2	3.7	2.98	2.660	- 0.320
-8.6	3.8	1.448	1.039	- 0.409
6.7	4.1	2.455	1.711	- 0.744
-4.5	4.3	2.66	1.933	- 0.727
-0.9	4.4	3.316	2.099	- 1.207
-10	5.7	0.957	0.659	- 0.298
0.8	6.2	2.278	1.595	- 0.683
14.8	6.4	0.306	0.381	0.075
-2.4	6.4	2.098	1.574	- 0.524
-6.3	6.4	1.647	1.280	- 0.367
7.8	6.9	1.208	0.994	- 0.214
4.4	6.9	1.835	1.249	- 0.586
11.5	7.4	0.654	0.538	- 0.116
-10	8.9	0.806	0.614	- 0.192
-6.8	9	0.202	0.899	0.697
14.6	9.3	0.311	0.344	0.033
0.2	9.3	1.524	1.075	- 0.449
3.6	9.5	1.292	0.997	- 0.295
-3	9.5	1.415	1.050	- 0.365
10.1	10.1	0.654	0.566	- 0.088
6.8	10.1	0.957	0.755	- 0.202
-9.6	11.3	0.645	0.545	- 0.100
-6.3	11.7	0.865	0.832	- 0.033
7	12	0.757	0.597	- 0.160
3.6	12	0.964	0.725	- 0.239
14.5	12.1	0.311	0.283	- 0.028
10.2	12.1	0.541	0.493	- 0.048
0.3	12.1	0.98	0.793	- 0.793
-3.1	12.1	0.966	0.772	- 0.194
-5.8	12.4	0.886	0.739	- 0.147
-2.2	12.8	0.975	0.749	- 0.226
7.2	12.9	0.748	0.567	- 0.181
2.5	13	0.915	0.753	- 0.162
-9.1	13	0.603	0.517	- 0.0.86
11.5	13.1	0.429	0.443	- 0.014

Table 5-9. Summary of Observed vs. Estimated Fluence Rate Data for Water with 73% UV Transmission

Vertical Distance from Lamp Center (cm)	Horizontal Distance from Quartz Sleeve (cm)	Observed Fluence Rate (mW/cm^2)	Estimated Fluence Rate (mW/cm^2)	Difference wrt Observed Fluence Rate (mW/cm^2)
6.9	2.2	1.501	1.834	0.333
2.8	2.2	1.547	2.497	0.950
-1	2.3	1.356	2.369	1.013
-5.6	2.3	0.884	1.835	0.951
15.8	2.4	0.387	0.127	- 0.260
11	2.5	1.139	0.535	- 0.604
17.3	4.7	0.017	0.059	0.042
13.6	5.2	0.065	0.182	0.117
11.1	5.3	0.136	0.295	0.159
3.6	5.4	0.527	0.823	0.296
-3.6	5.6	0.422	0.700	0.278
-7.5	5.6	0.228	0.586	0.358
7.2	5.7	0.369	0.594	0.225
-0.3	5.7	0.488	0.848	0.360
17.1	8.1	0.007	0.046	0.039
14.2	8.4	0.018	0.094	0.076
7	8.5	0.103	0.262	0.159
-7.7	8.5	0.074	0.262	0.188
10.9	8.7	0.051	0.183	0.132
-3.8	8.7	0.117	0.349	0.232
3.2	8.8	0.132	0.298	0.166
-0.1	8.9	0.133	0.290	0.157
-7.5	11.3	0.022	0.132	0.110
0.7	11.4	0.040	0.175	0.135
12.4	11.5	0.012	0.072	0.032
16.8	11.6	0.004	0.039	0.035
8.6	11.6	0.023	0.115	0.095
4.7	11.6	0.035	0.154	0.119
-3.5	11.7	0.031	0.154	0.123
16.9	12.1	0.004	0.035	0.031
12.6	12.5	0.009	0.063	0.054
8.3	12.5	0.018	0.095	0.078
3	12.6	0.023	0.139	0.116
-1.7	12.6	0.024	0.148	0.124
-7	12.6	0.016	0.121	0.105
6.9	2.2	1.501	1.834	0.333
2.8	2.2	1.547	2.497	0.950

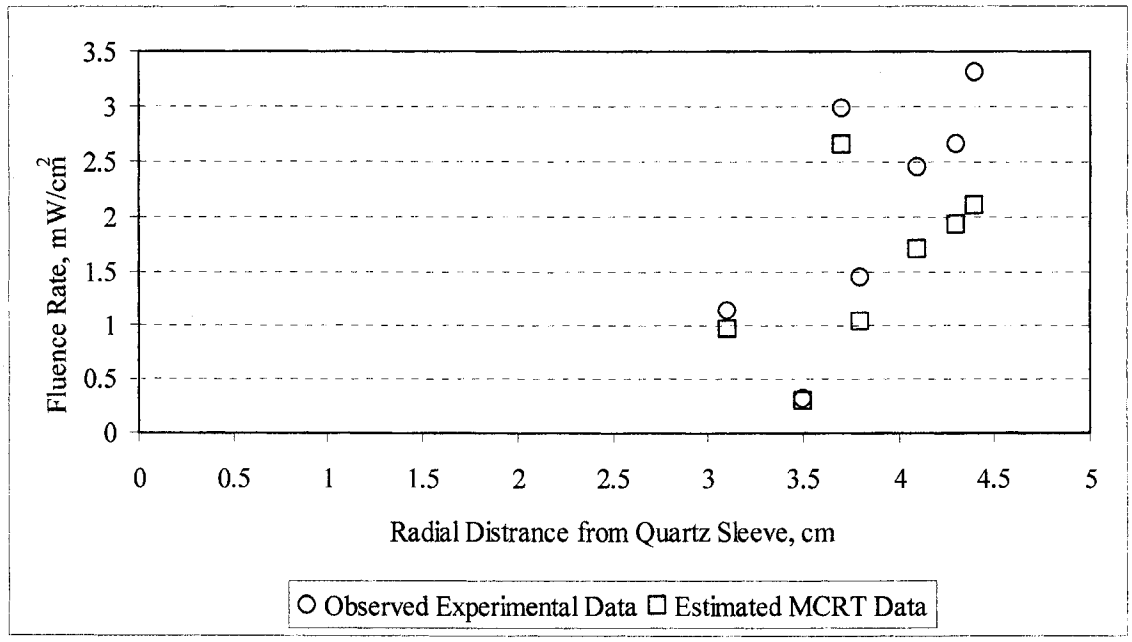

Figure 5-3. Observed vs. Estimated Fluence Rate Comparison for Radial Distance from 0 to 5 cm - 100 % UV Transmission Water

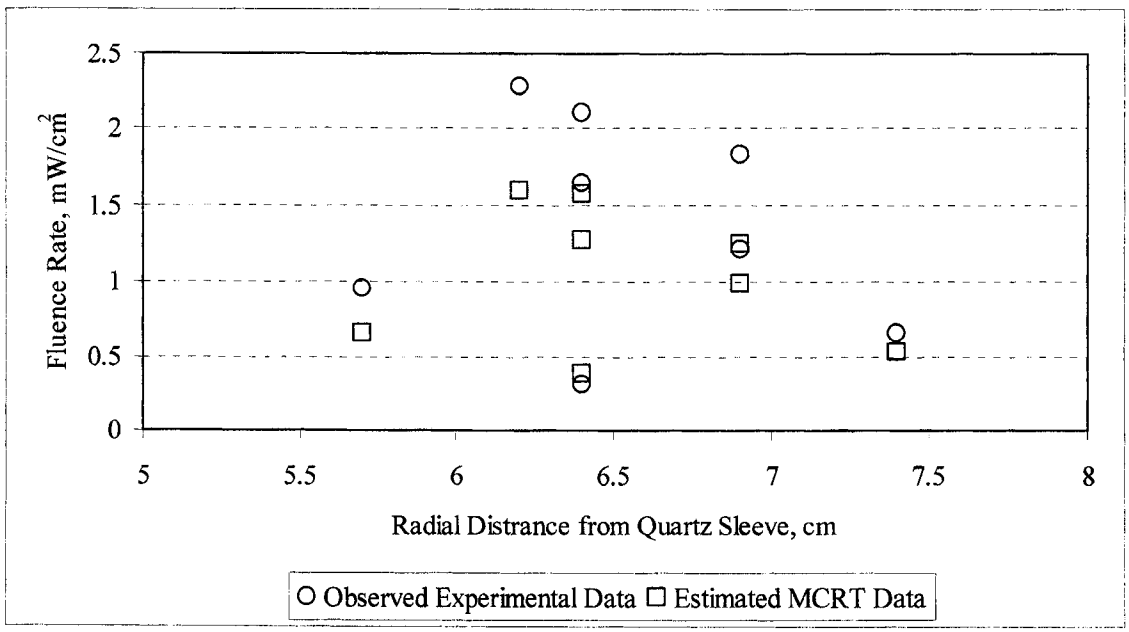

Figure 5-4. Observed vs. Estimated Fluence Rate Comparison for Radial Distance from 5 to 8 cm - 100 % UV Transmission Water

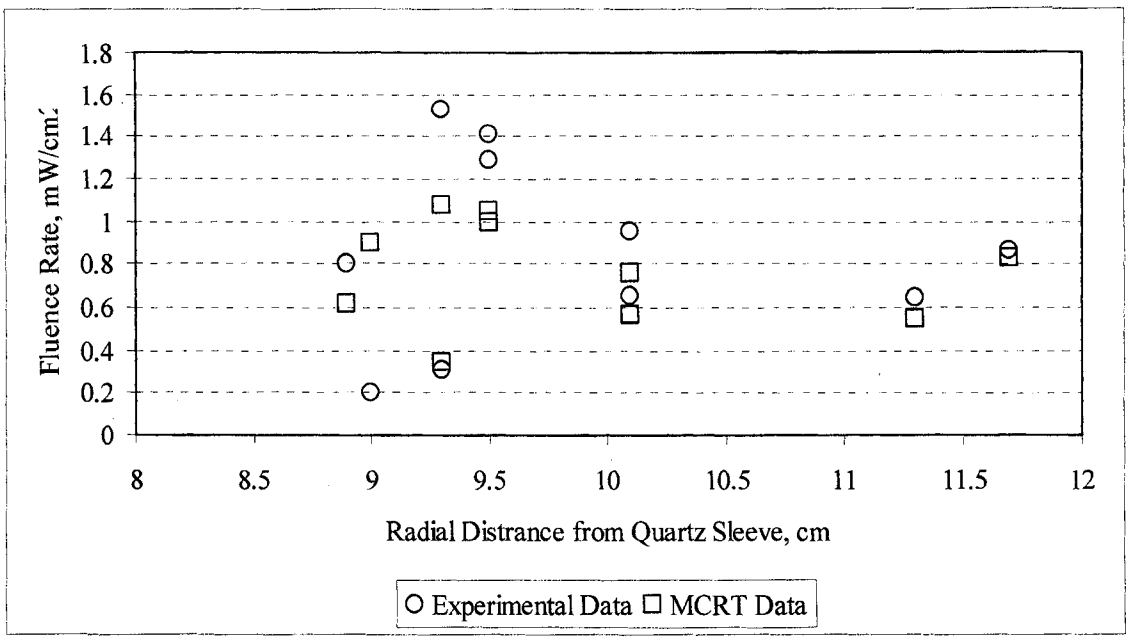

Figure 5-5. Observed vs. Estimated Fluence Rate Comparison for Radial Distance from 8 to 12 cm - 100 % UV Transmission Water

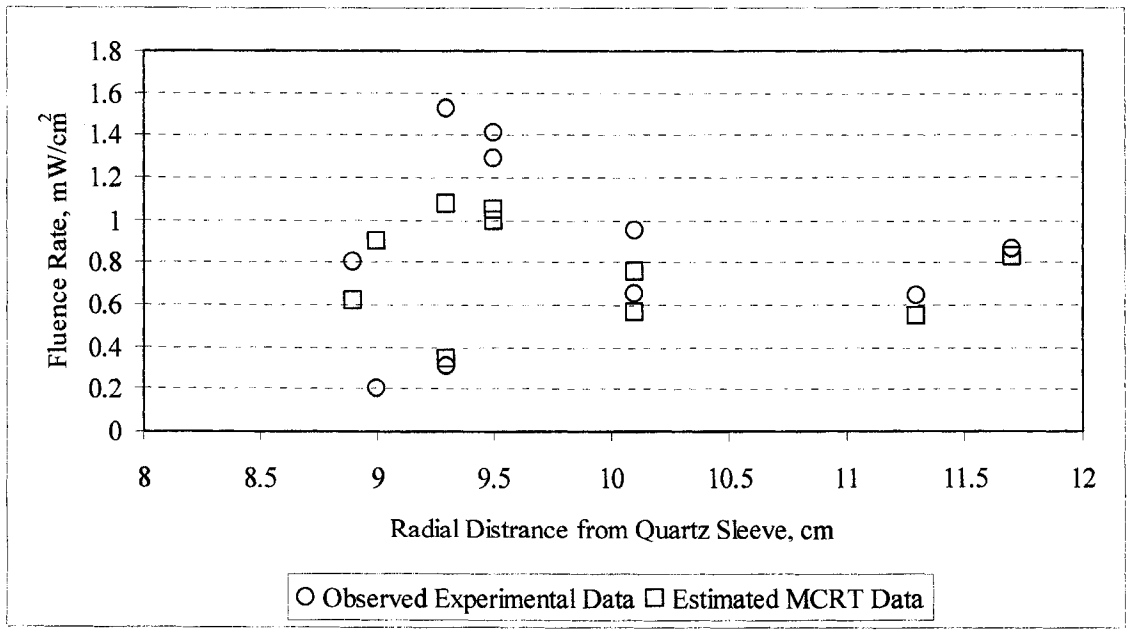

Figure 5-6. Observed vs. Estimated Fluence Rate Comparison for Radial Distance from 10 to 13.5 cm - 100 % UV Transmission Water

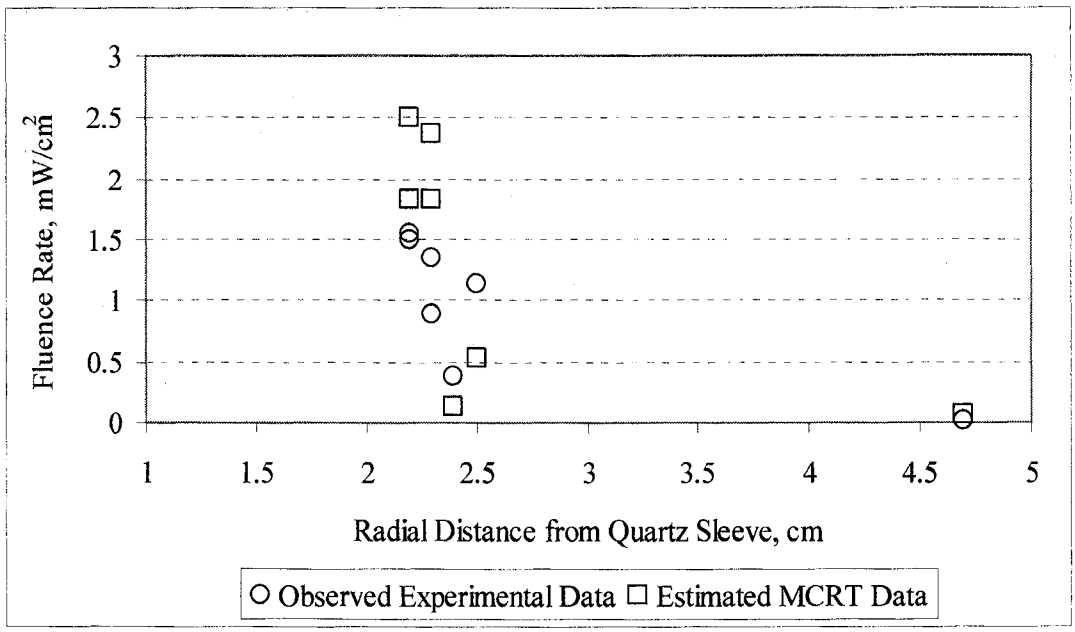

Figure 5-7. Observed vs. Estimated Fluence Rate Comparison for Radial Distance from 0 to 5 cm - 73 % UV Transmission Water

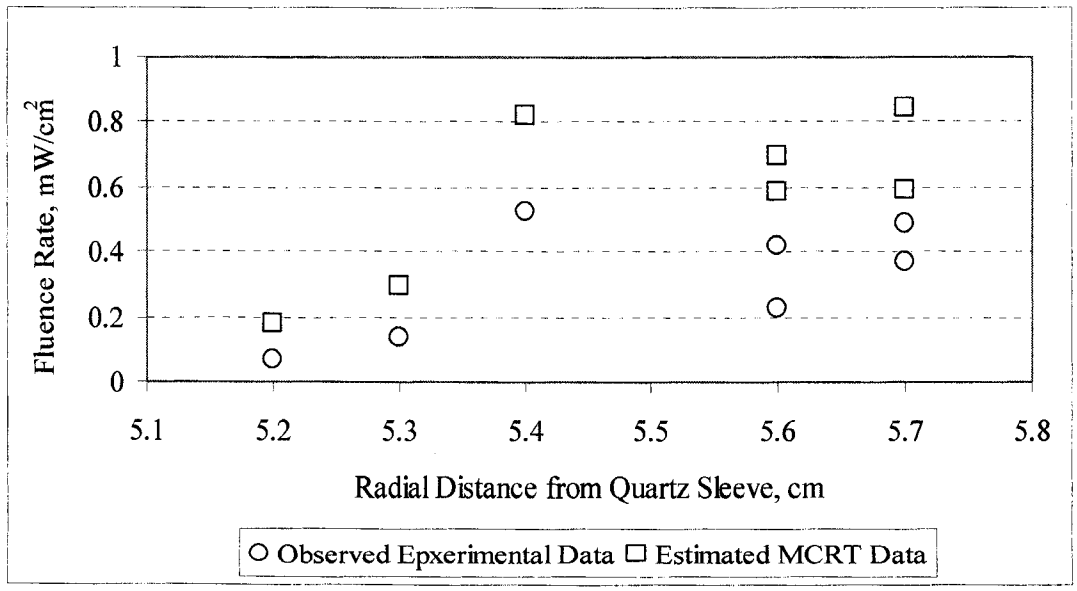

Figure 5-8. Observed vs. Estimated Fluence Rate Comparison for Radial Distance from 5 to 6 cm - 73 % UV Transmission Water

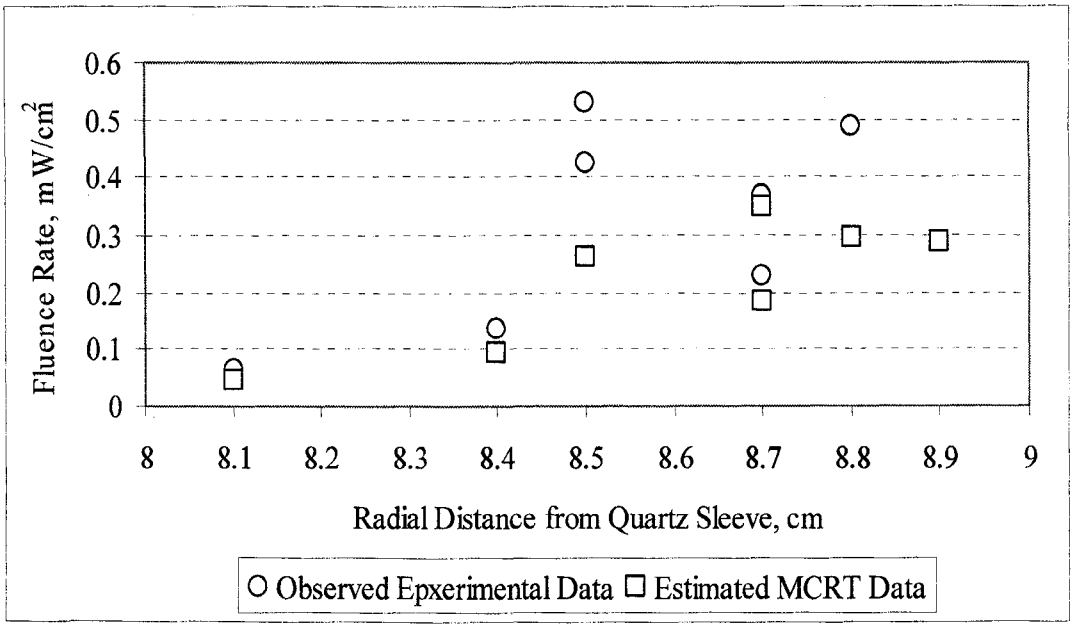

Figure 5-9. Observed vs. Estimated Fluence Rate Comparison for Radial Distance from 8 to 9 cm - 73 % UV Transmission Water

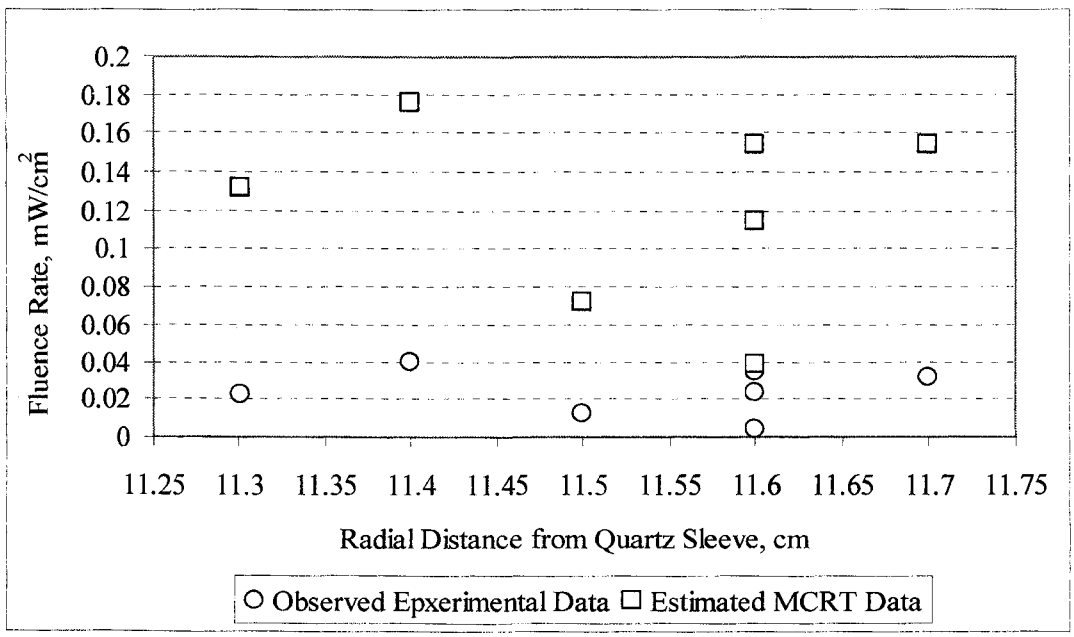

Figure 5-10. Observed vs. Estimated Fluence Rate Comparison for Radial Distance from 11 to 12 cm - 73 % UV Transmission Water

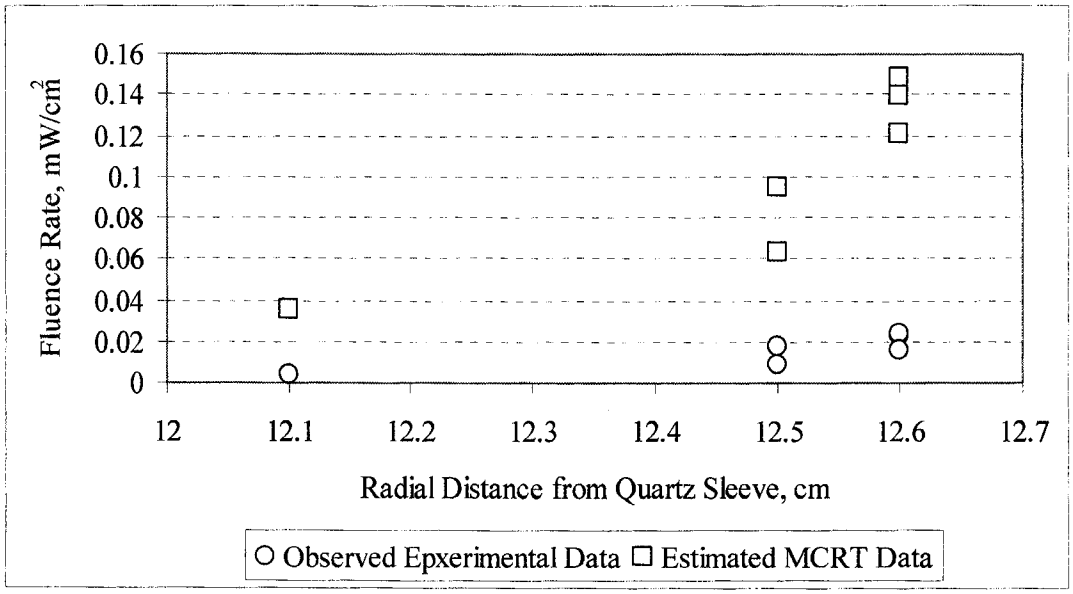

Figure 5-11. Observed vs. Estimated Fluence Rate Comparison for Radial Distance from 12 to 13 cm - 73 % UV Transmission Water

To further compare the MCRT simulation data with the observed experimental data, standard root mean square errors (RMSE) were estimated using the following equation:

$$RMSE = \sqrt{\frac{\left(\sum\left(E'_{Obs} - E'_{MCRT}\right)\right)}{N}} \qquad (5\text{-}1)$$

where E'_{Obs} = Observed experimental data, obtained from the actinometric tests, mW/cm^2.

E'_{MCRT} = Estimated MCRT simulation data, generated for the same systems used in the actinometry tests, mW/cm^2, as listed in Tables 5-6 and 5-7.

N = Number of samples used in the analysis, 20, as shown in Tables 5-6 and 5-7.

The RMSE with respect to experimental data for the water system with the 100 percent UV transmission case are shown in Figure 5-12. These data indicate that 32 of 37 RMSE values (86 percent) were below the median RMSE value of 0.7 mW/cm^2.

The RMSE with respect to experimental data for the water system with the 73 percent UV transmission case are shown in Figure 5-13. These data indicate that 32 of 35 RMSE values (91 percent) were below the median RMSE value of 1.3 mW/cm^2.

In addition, 95 percent confidence limit (CL) for both sets of MCRT fluence rate data were calculated and compared with the experimental fluence rates as shown in Tables 5-8 and 5-9. For the case of 100 percent UV transmission, the data listed in Table 5-8 showed that nine of 37 experimental data points, or 24 percent, were within the MCRT confidence limit. Percent differences between these MCRT data points relative to corresponding experimental data were listed as zero. Where experimental data points were outside the MCRT confidence limit, upper or lower MCRT limit values were within 0.1 percent to 30 percent of corresponding experimental values. One exception to the above range is related to the data associated with the vertical coordinate of 13.9 cm and the radial coordinate of 2.8 cm and 27.3 cm, for which the percent difference of 330 was found. For this data location, the MCRT fluence rate appeared consistent with MCRT fluence rates at other locations approximately the same relative to the lamp center and quartz sleeve surface, such as the last data point listed in Table 5-8.

Box plots shown in Figures 5-15 through 5-23 indicate that estimated MCRT fluence rate results were in good agreement with the observed experimental data for all tested radial locations.

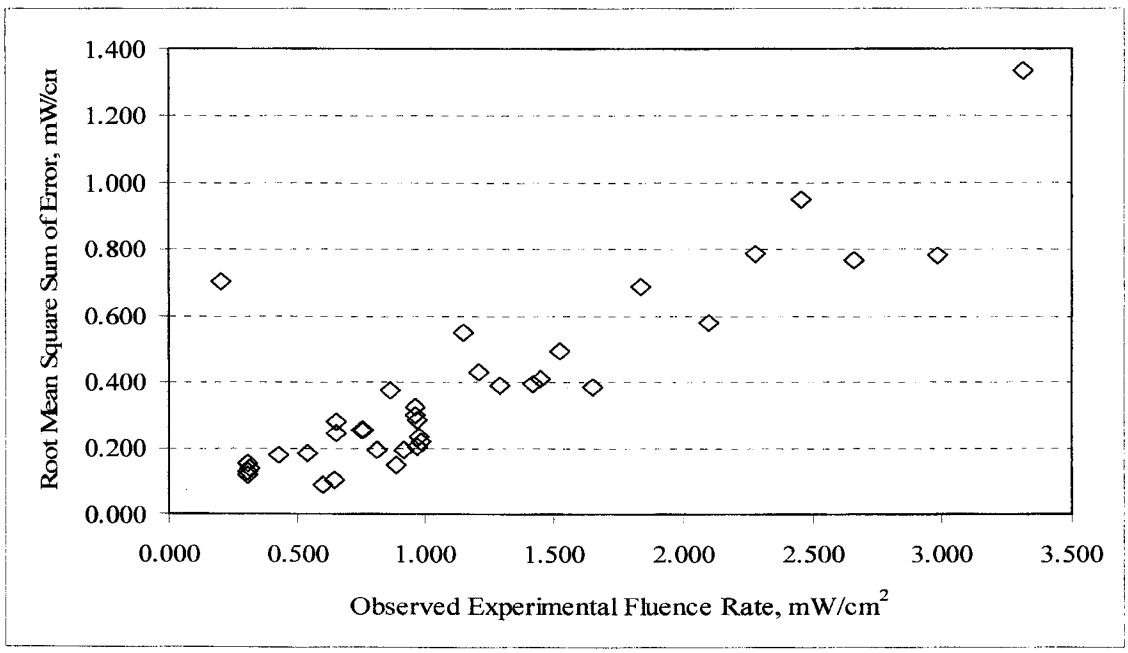

Figure 5-12. Root Mean Square of Error with Respect to Observed Experimental Data for Water System with 100 % UV Transmission

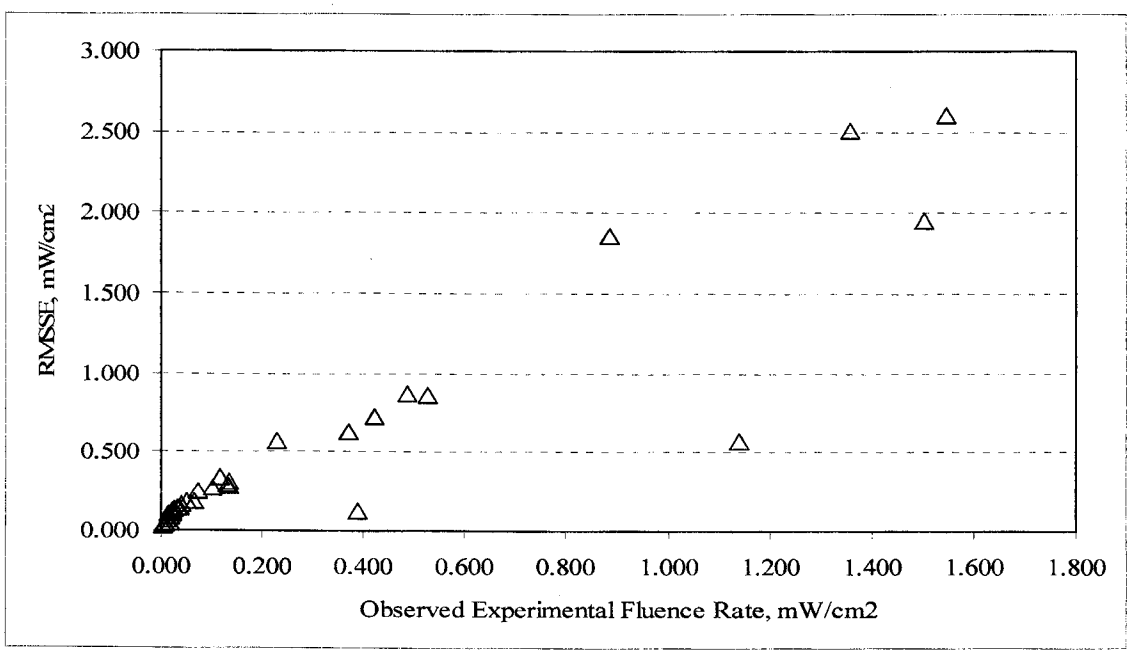

Figure 5-13. Root Mean Square of Error with Respect to Observed Experimental Fluence Rate Data for Water System with 73 % UV Transmission

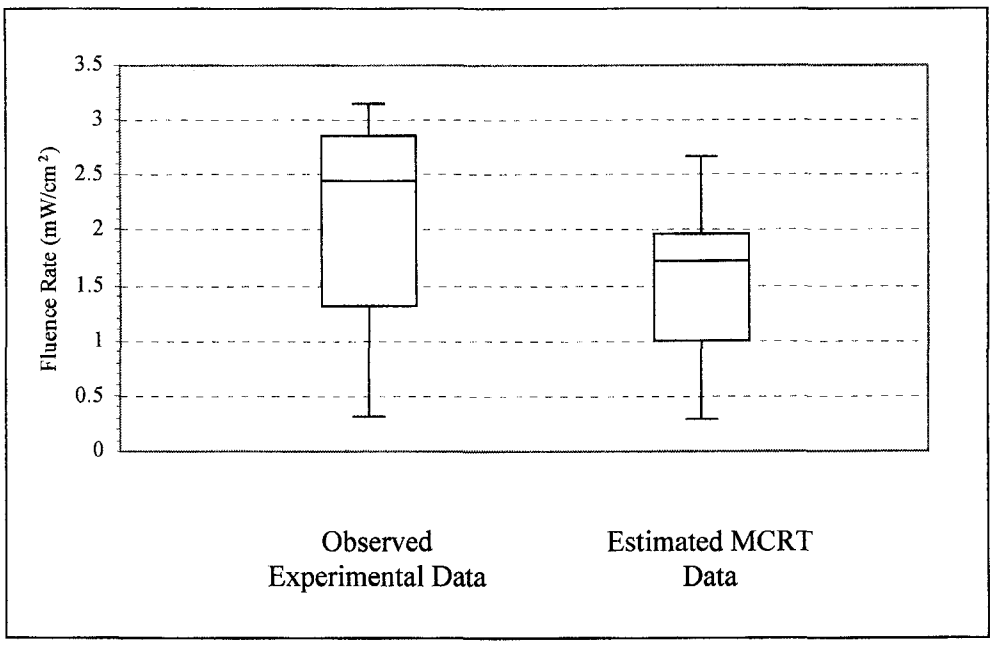

Figure 5-14. Comparison of Observed Experimental with Estimated MCRT Fluence Rates at Radial Distance 3.1 to 4.4 cm from Quartz Sleeve for Water System with 100 % UV Transmission

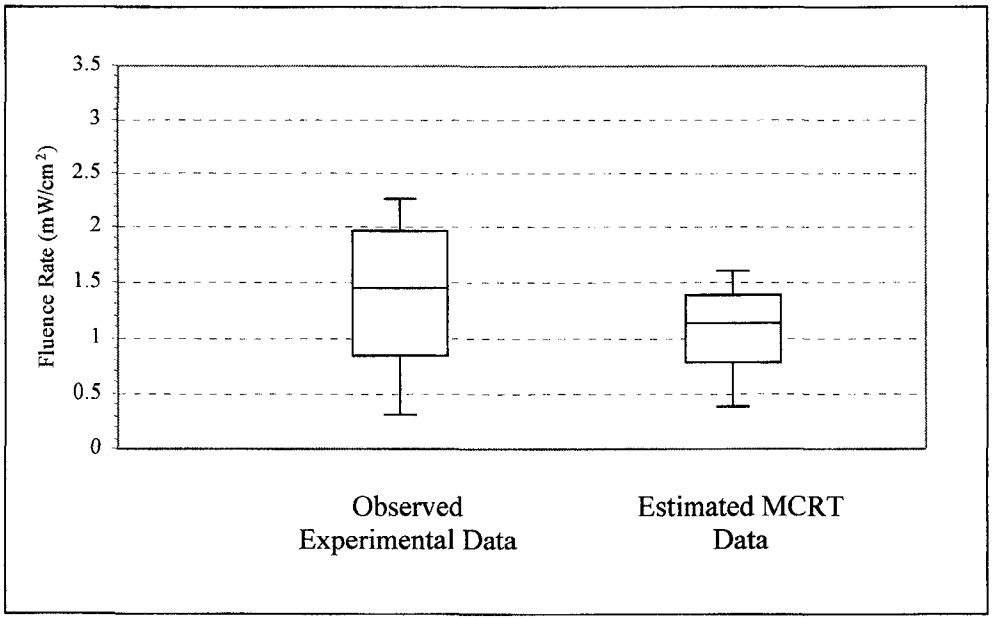

Figure 5-15. Comparison of Observed Experimental with Estimated MCRT Fluence Rates at Radial Distance 5.7 to 7.4 cm from Quartz Sleeve for Water System with 100 % UV Transmission

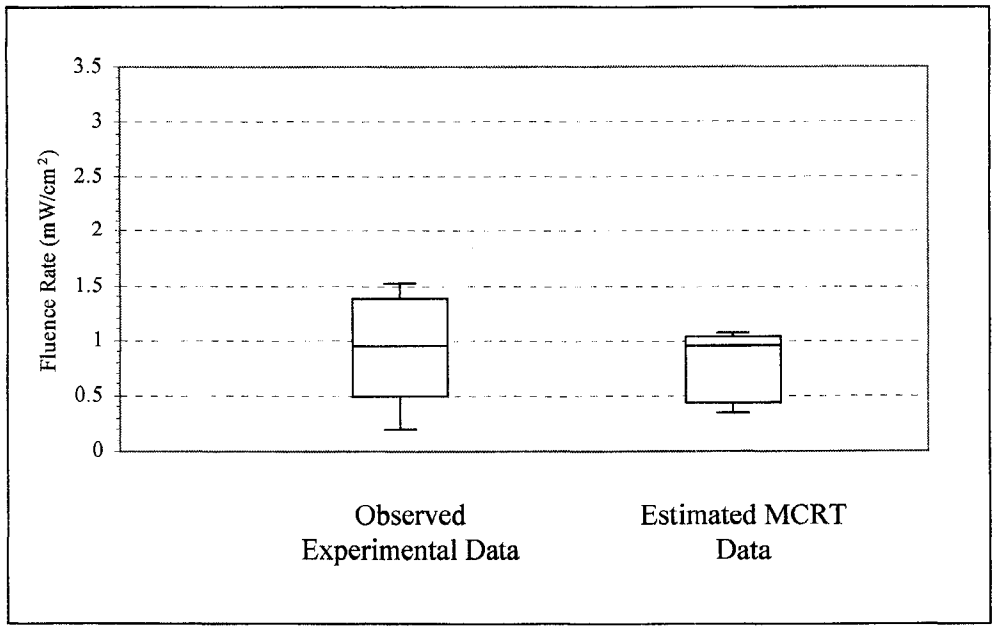

Figure 5-16. Comparison of Observed Experimental with Estimated MCRT Fluence Rates at Radial Distance 8.9 to 10.1 cm from Quartz Sleeve for Water System with 100 % UV Transmission

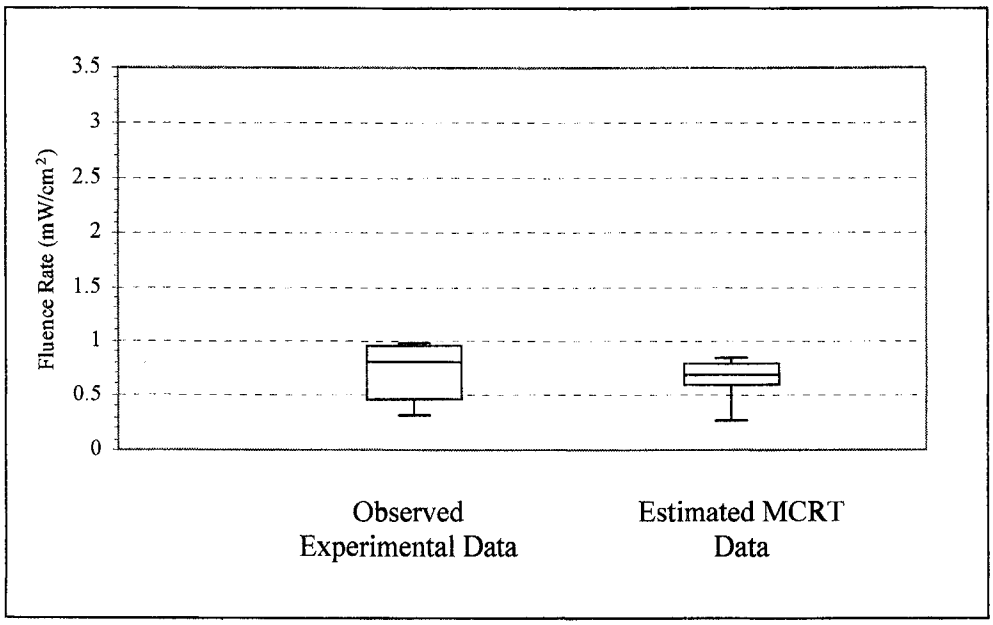

Figure 5-17. Comparison of Observed Experimental with Estimated MCRT Fluence Rates at Radial Distance 11.3 to 12.0 cm from Quartz Sleeve for Water System with 100 % UV Transmission

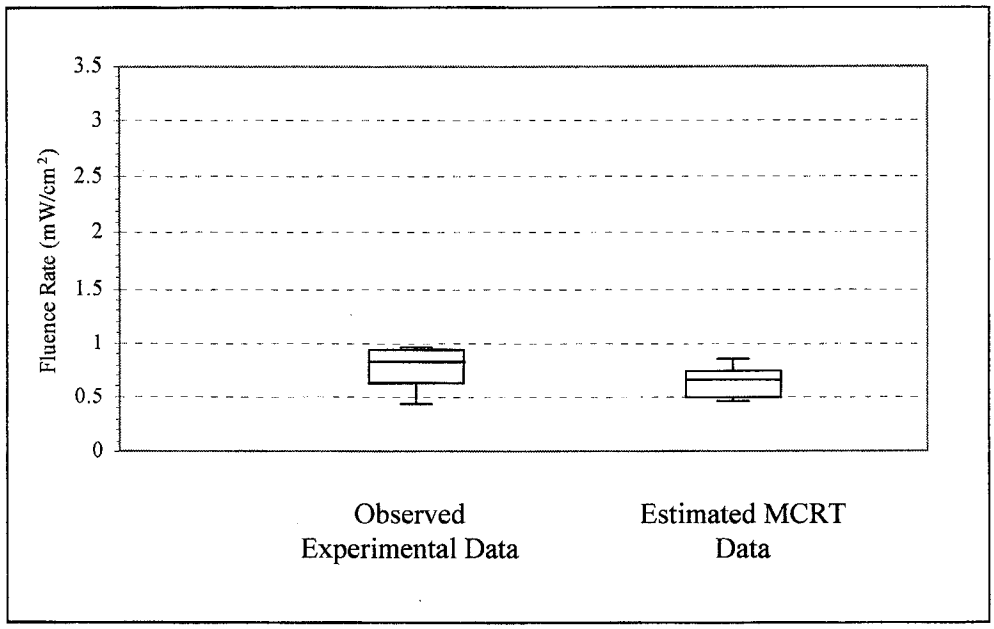

Figure 5-18. Comparison of Observed Experimental with Estimated MCRT Fluence Rates at Radial Distance 12.4 to 13.0 cm from Quartz Sleeve for Water System with 100 % UV Transmission

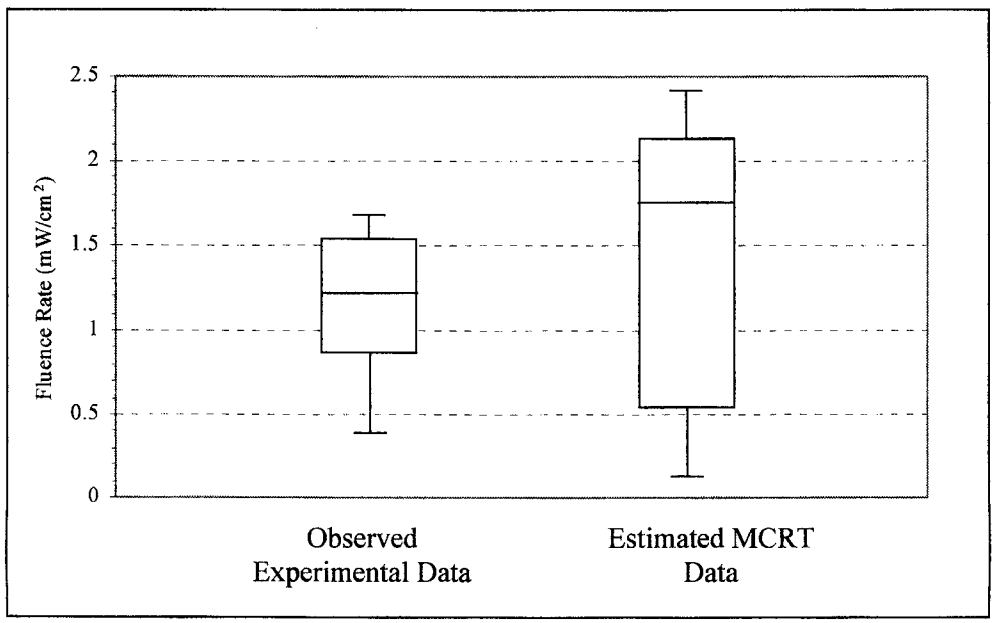

Figure 5-19. Comparison of Observed Experimental with Estimated MCRT Fluence Rates at Radial Distance 2.3 to 2.5 cm from Quartz Sleeve for Water System with 73% UV Transmission

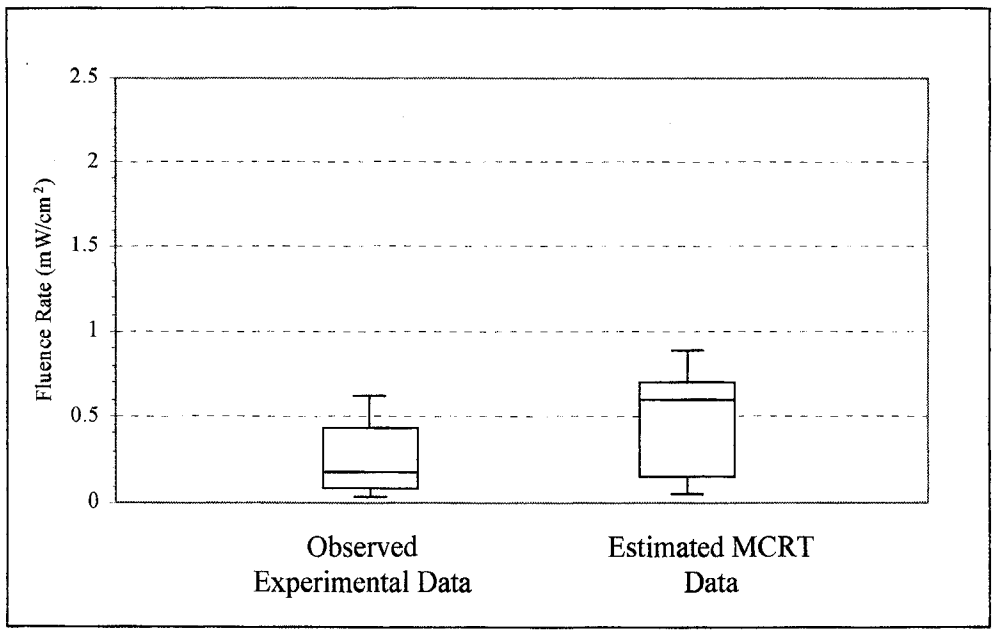

Figure 5-20. Comparison of Observed Experimental with Estimated MCRT Fluence Rates at Radial Distance 4.7 to 5.7 cm from Quartz Sleeve for Water System with 73% UV Transmission

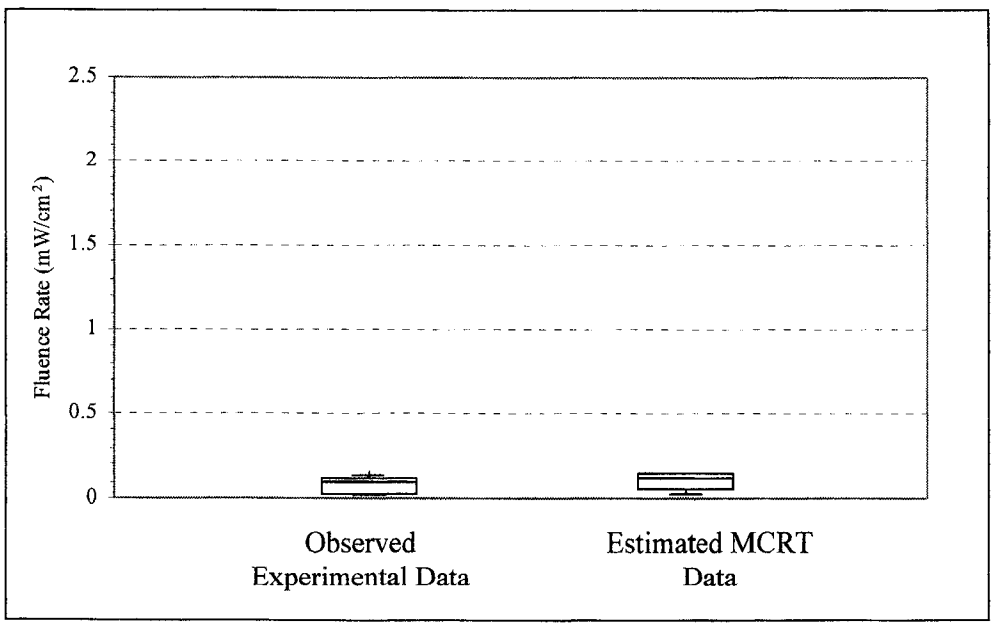

Figure 5-21. Comparison of Observed Experimental with Estimated MCRT Fluence Rates at Radial Distance 8.1 to 8.9 cm from Quartz Sleeve for Water System with 73% UV Transmission

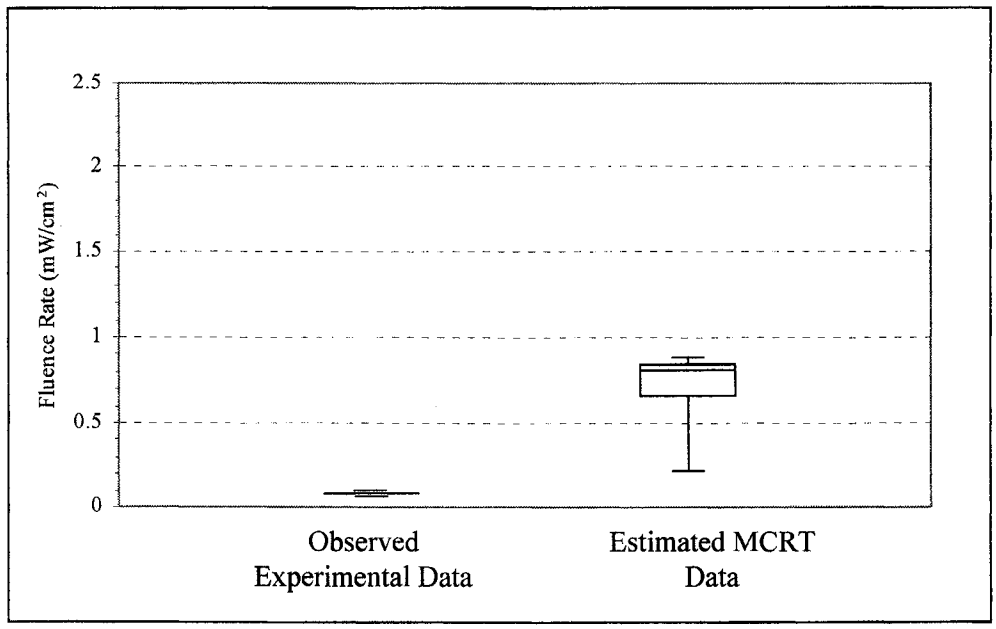

Figure 5-22. Comparison of Observed Experimental with Estimated MCRT Fluence Rates at Radial Distance 11.0 to 11.3 cm from Quartz Sleeve for Water System with 73% UV Transmission

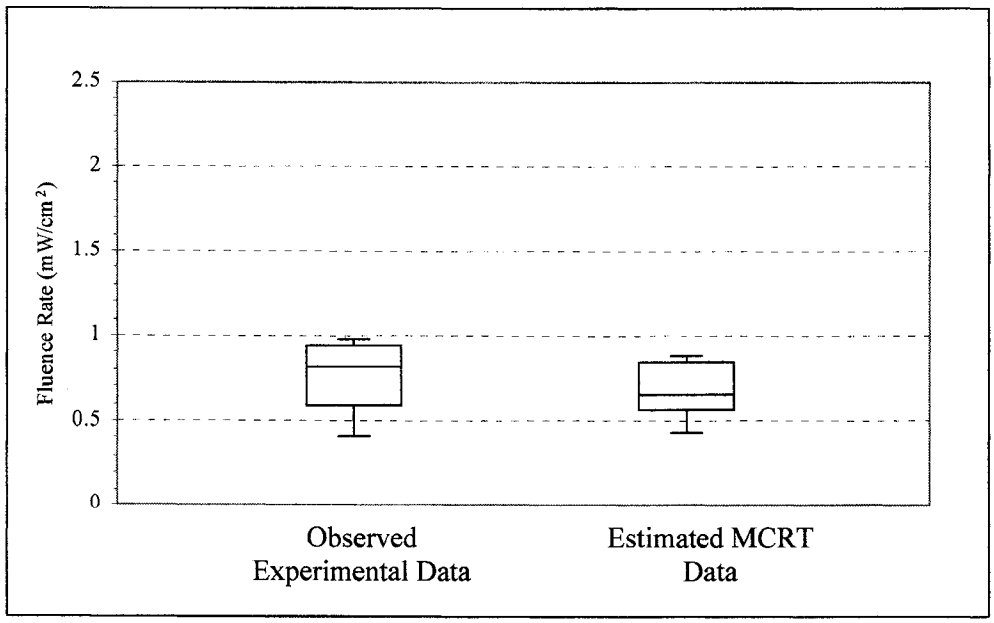

Figure 5-23. Comparison of Observed Experimental with Estimated MCRT Fluence Rates at Radial Distance 12.0 to 12.1 from Quartz Sleeve for Water System with 73% UV Transmission

Further, the MCRT values for the case with 100 percent UV transmission were generally higher than corresponding experimental values, as indicated by positive values of the differences listed in Table 5-10. Positive value progressions mildly indicate possible absorption of the 1 cm test spheres by the quartz material. However, such absorption was not considered in the MCRT simulation due to lack of specific dimensional information of the spheres. Furthermore, the curvature of the sphere would reflect and scatter more light bundles approaching the spheres, as conceptually shown in Figure 5-24. Theoretically speaking, additional analysis of the ray tracing through each sphere would be helpful in determining the portion of incident energies that reach the actinometric solutions. However, additional gains expected from such analysis would be negligible and were not considered critical in the present study. Based on simulation results for the quartz sleeve, the overall UV transmittance across the 3 mm quartz sleeve ranged from 0.72 to 0.94, depending on direction cosines of incident bundles to the quartz surface. It might be possible that MCRT fluence rates would be closer to the observed experimental data if these absorption factors were accounted for. In summary, comparison results indicated that MCRT simulation data were very close to or approximately 30 percent higher than the experimental data for the case with 100 percent UV transmission.

For the case with 73 percent UV transmission, the data listed in Table 5-11 showed that 13 of 35 experimental data points (or 37 percent) were within the corresponding MCRT confidence limit. Percent differences between these MCRT data point relative to corresponding experimental data were listed as zero. Where experimental data points were outside the MCRT confidence limit, upper or lower MCRT

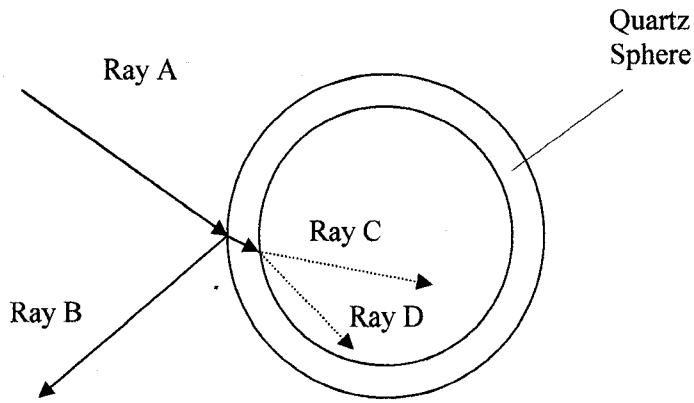

Figure 5-24. Reflection and Refraction Bundles at a Quartz Sphere

limit values were within two to 152 percent of corresponding experimental values, and approximately half of these data points were higher or lower than the MCRT lower or upper limit values. The above results suggest that MCRT simulation data were close to or varied by approximately 150 percent from the experimental data for the case with 73 percent UV transmission.

In summary, strong correlations between MCRT fluence data and actinometric data were found in both of the 100 percent and 73 percent UV transmission cases.

Table 5-10. Comparison of Observed Experimental and Estimated Fluence Rate Data for a Water System with 100% UV Transmission

Vert. Coord. Z (cm)	Radial Coordinate X (y=15) or v.s. (cm)	Radial Coordinate x (y=15) or v.s. (cm)	Observed Exp. Fluence Rate (mW/cm^2)	Estimated MCRT Fluence Rate (mW/cm^2)	Difference wrt Obs.Fluence Rate (mW/cm^2)
13.3	8.3	21.7	0.313	0.142	-0.012
13.4	5.4	24.6	0.306	0.095	0.075
13.3	2.5	27.5	0.311	0.155	0.033
13.3	-0.3	30.3	0.311	0.130	-0.028
13.5	4.4	25.6	0.654	0.262	-0.116
13.4	-1.3	31.3	0.429	0.185	0.014
14.0	8.7	21.3	1.145	0.527	-0.185
13.5	-0.3	30.3	0.541	0.185	-0.048
13.6	1.7	28.3	0.654	0.234	-0.088
14.7	7.7	22.3	2.455	0.610	-0.744
14.0	4.9	25.1	1.208	0.381	-0.214
13.8	1.7	28.3	0.957	0.260	-0.202
13.6	-0.2	30.2	0.757	0.202	-0.160
13.6	-1.1	31.1	0.748	0.179	-0.181
14.2	4.9	25.1	1.835	0.374	-0.586
14.0	2.3	27.7	1.292	0.261	-0.295
13.7	-0.2	30.2	0.964	0.156	-0.239
15.7	8.1	21.9	2.980	0.733	-0.320
13.8	-1.2	31.2	0.915	0.106	-0.162
15.1	7.4	22.6	3.316	0.559	-1.217
14.6	5.6	24.4	2.278	0.397	-0.683
14.1	2.5	27.5	1.524	0.209	-0.449
13.8	-0.3	30.3	0.980	0.113	-0.187
13.7	-1.0	31.0	0.975	0.055	-0.226
14.6	5.4	24.6	2.098	0.250	-0.524
14.0	2.3	27.7	1.415	0.151	-0.365
13.8	-0.3	30.3	0.966	0.069	-0.194
14.9	7.5	22.5	2.660	0.251	-0.727
14.3	5.4	24.6	1.647	0.109	-0.367
13.9	2.8	27.2	0.202	0.068	0.697
13.8	0.1	29.9	0.865	0.379	-0.033
13.7	-0.6	30.6	0.886	0.036	-0.147
14.0	8.0	22.0	1.448	0.022	-0.409
13.5	-1.2	31.2	0.603	0.024	-0.086
13.5	0.5	29.5	0.645	0.029	-0.100
13.7	6.1	23.9	0.957	0.031	-0.298
13.6	2.9	27.1	0.806	0.026	-0.192

Table 5-11. Comparison of Observed Experimental and Estimated Fluence Rate Data for a Water System with 73% UV Transmission

Vert. Coord. Z (cm)	Radial Coordinate		Observed Exp. Fluence Rate (mW/cm^2)	Estimated MCRT Fluence Rate (mW/cm^2)	Difference wrt Obs.Fluence Rate (mW/cm^2)
	x (y=15) or v.s. (cm)	x (y=15) or v.s. (cm)			
13.1	17.5	12.5	0.017	0.059	0.042
13.1	20.5	9.5	0.007	0.046	0.039
13.0	22.9	7.1	0.004	0.035	0.031
13.1	23.7	6.3	0.004	0.039	0.035
13.2	14.3	15.7	0.387	0.127	-0.260
13.1	19.2	10.8	0.018	0.094	0.076
13.3	16.8	13.2	0.065	0.182	0.117
13.1	21.0	9.0	0.009	0.063	0.054
13.1	20.0	10.0	0.012	0.072	0.060
13.4	16.2	13.8	0.136	0.295	0.159
13.8	14.5	15.5	1.139	0.535	-0.604
13.3	17.6	12.4	0.051	0.183	0.132
13.2	19.0	11.0	0.023	0.115	0.092
13.1	19.3	10.7	0.018	0.095	0.077
13.8	15.6	14.4	0.369	0.594	0.225
13.4	16.5	13.5	0.103	0.262	0.159
15.5	15.2	14.8	1.501	1.834	0.333
13.2	18.4	11.6	0.035	0.154	0.119
14.1	15.6	14.4	0.527	0.823	0.296
13.4	16.3	13.7	0.132	0.298	0.166
13.2	20.1	9.9	0.023	0.139	0.116
16.3	15.6	14.4	1.547	2.497	0.950
13.2	18.4	11.6	0.040	0.175	0.135
13.4	16.2	13.8	0.133	0.290	0.157
13.3	15.7	14.3	0.488	0.848	0.360
16.2	15.7	14.3	1.356	2.369	1.013
13.2	20.2	9.8	0.024	0.148	0.124
13.2	19.0	11.0	0.031	0.154	0.123
13.2	15.7	14.3	0.422	0.700	0.278
13.4	17.0	13.0	0.117	0.349	0.232
15.2	16.1	13.9	0.884	1.835	0.951
13.1	21.5	8.5	0.016	0.121	0.105
13.7	16.6	13.4	0.228	0.586	0.358
13.1	20.0	10.0	0.022	0.132	0.110
13.3	17.5	12.5	0.074	0.262	0.188
13.1	17.5	12.5	0.017	0.059	0.042
13.1	20.5	9.5	0.007	0.046	0.039

5.1.2 Fluence Rate Distribution In Air

The MCRT program was also used to generate fluence rate data in air to compare with corresponding experimental irradiance data provided by Trojan Technologies Inc. The experimental data was obtained by using an 80 watt lamp with 147 cm arc length without a quartz sleeve and a sensor located along a line normal to the center of the lamp. The lamp diameter was 19 mm. The experimental data obtained from these measurements were considered irradiance data that corresponded to UV energies measured in the directions limited by the lense and aperture of the sensor. UV irradiance was measured for the distance ranging from 1 cm from the lamp surface to 289 cm from the lamp surface.

To generate MCRT data for validation purposes, absorption of UV energy by the air was not considered. The MCRT program generated fluence data in the three dimensional space surrounding the lamp. To compare with the experimental irradiance data, only the MCRT fluence data in the radial direction along the normal line at the center of the lamp were used. A simplified schematic of the UV irradiance measurement system in air is shown in Figure 5-24. In this system, a low pressure lamp was placed horizontally with its center lined up with a sensor located from 1 cm to 289 cm from the lamp center.

As shown in a comparison plot (Figure 5-25) MCRT fluence rates were generally higher than the irradiance data. However, the MCRT simulation model repeatedly produced a very close system response characteristic under various light bundle conditions. The positive excess trend was attributed to the fact that the MCRT model accounted for fluence rate contributions from all directions, whereas irradiance

measurements resulted from the limited scope of the lense and aperture of the UV sensor fixed at one direction. Thus, reflection, refraction, and absorption by the lense potentially resulted in a partial, under-registered amount of the actual UV energies entering the sensor. Thus, it is postulated that the simulated MCRT model data represents more realistic UV energy distribution than irradiance measured in air via the conventional stationary lense and sensor setups. This is an important hypothesis that needs to be investigated and validated in the future.

An analysis of the data was conducted by calculating the 95 percent confidence limit of the MCRT data and comparing the measurement data with the upper limit of the MCRT data. As shown in Table 5-15, the fluence rate data were 10 to 90 percent higher than the irradiance data in the first 100 cm and were 0 to 90 percent lower than the irradiance data. The sum of error analysis shown in Figure 5-27 indicates that the majority of MCRT fluence data were within 50 percent higher than the irradiance data. In spite of the differences, the MCRT model was capable of generating fluence rates in the air environment that were in reasonably good agreement with the measured data presented.

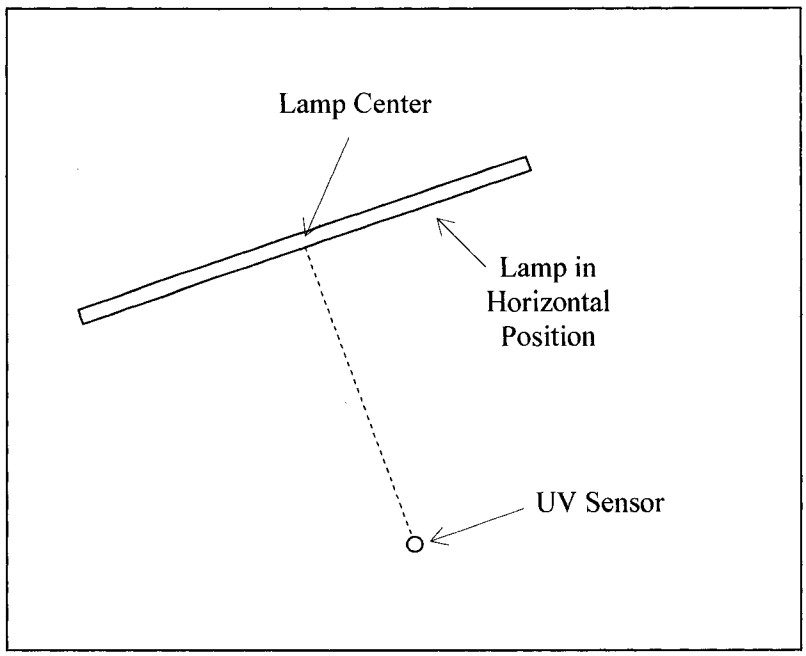

Figure 5-25. Simplified Schematic of UV Irradiance Measurement System in Air

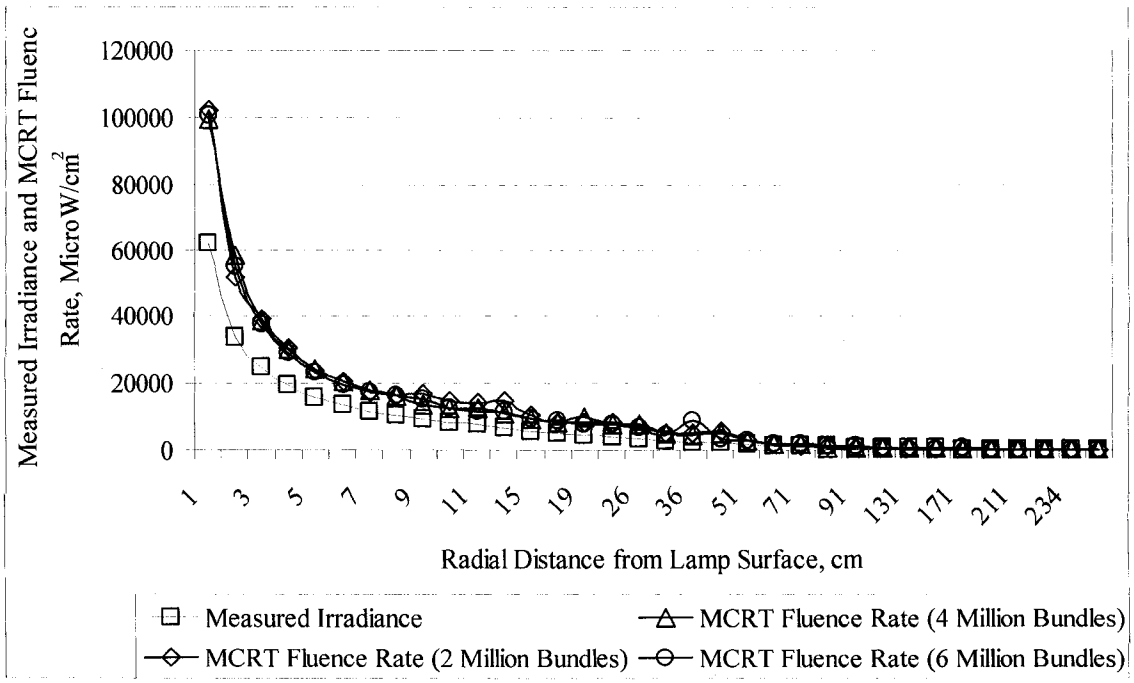

Figure 5-26. Comparison of Measured Irradiance and MCRT Fluence Rates in Air

Table 5-12. Comparison of Observed Experimental Irradiance and Estimated MCRT Fluence Data for an Air System

Estimated MCRT Fluence Rate (microW/cm^2)							Observed Exper. Irradiance Data (microW/cm^2)	Percent Difference Relative to Experimental Irradiance Rates
Number of Simulated Bundles (Millions)					95% C.L.			
2	3	4	5	6	Lower	Upper		
102,160	98,505	99,720	97,984	100,751	98,341	101,307	62,058	-58
51,800	51,734	58,480	53,232	55,172	51,605	56,562	33,607	-54
39,120	36,667	38,820	36,000	37,494	36,441	38,799	24,484	-49
30,360	28,027	29,780	27,824	28,974	28,034	29,952	19,117	-47
23,560	23,787	24,060	22,688	23,147	22,974	23,922	15,616	-47
20,400	19,813	20,240	19,136	19,080	19,199	20,269	13,142	-46
17,360	18,107	17,900	16,960	17,656	17,200	17,993	11,483	-50
16,200	16,453	15,920	14,944	15,973	15,395	16,401	10,023	-54
16,560	15,440	13,380	14,176	14,960	13,840	15,966	9,024	-53
14,560	13,413	12,560	12,672	12,427	12,348	13,905	8,182	-51
13,960	12,533	12,060	11,152	11,400	11,245	13,198	7,450	-51
14,360	11,467	10,760	10,848	10,987	10,352	13,017	6,366	-63
10,360	9,387	8,940	9,392	9,240	8,996	9,931	5,544	-62
8,200	9,200	7,940	11,344	8,373	7,796	10,227	4,915	-59
8,280	7,733	9,560	7,728	7,693	7,499	8,899	4,391	-71
8,080	7,707	7,540	6,736	7,427	7,066	7,929	3,986	-77
7,080	6,786	7,700	5,856	6,507	6,187	7,384	3,217	-92
4,920	5,067	4,580	4,512	4,400	4,447	4,945	2,685	-66
4,680	3,760	4,420	3,568	8,400	3,236	6,696	2,304	-40
5,480	3,600	5,020	4,544	3,107	3,488	5,212	2,003	-74
2,640	2,720	2,760	3,104	2,440	2,521	2,944	1,565	-61
1,480	1,973	1,640	1,680	1,507	1,484	1,828	1,260	-18
1,040	1,387	1,340	1,232	1,440	1,149	1,426	1,033	-11
1,200	800	800	768	1,013	753	1,080	863	13
440	827	500	656	867	491	824	730	33
640	720	720	464	480	495	715	540	8
320	373	420	352	173	246	410	413	41
80	507	280	304	200	137	411	326	58
200	267	140	144	560	109	415	262	58
240	293	220	160	187	175	265	216	19
40	80	160	96	80	53	129	181	71
40	160	100	32	53	30	124	154	80
200	53	80	48	80	38	147	150	75
40	27	40	64	67	32	63	98	67

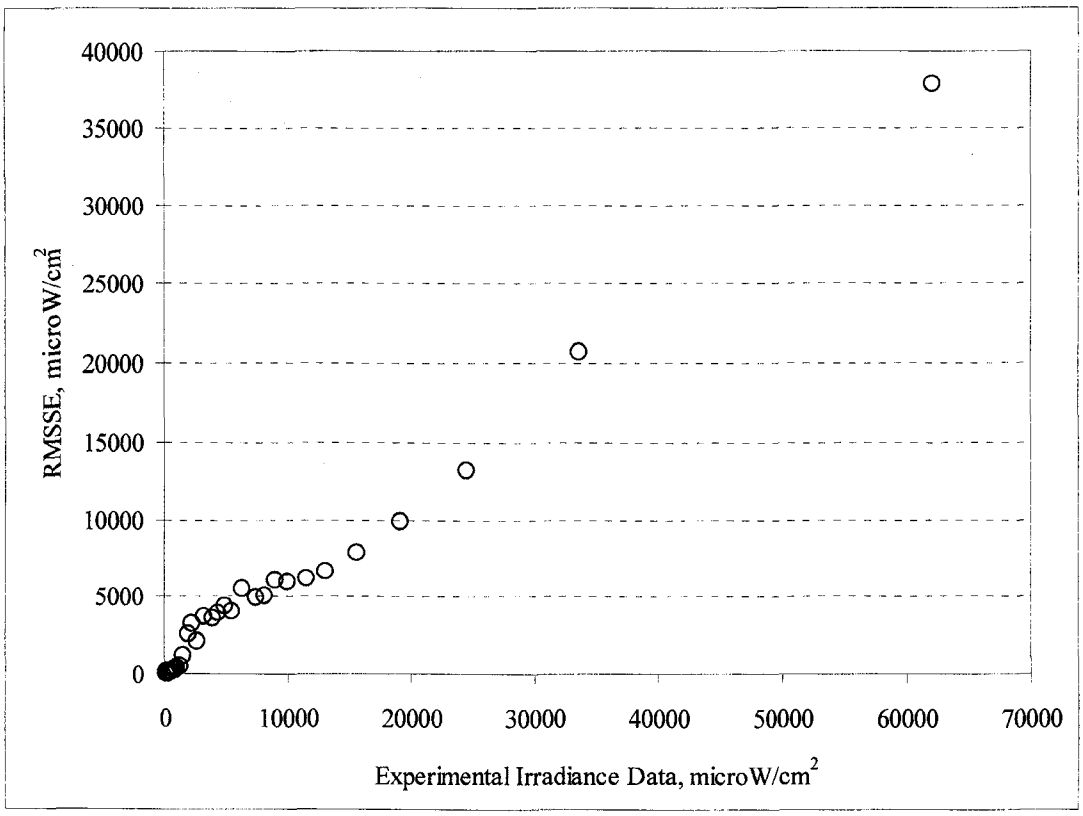

Figure 5-27. Root Mean Square of Error of MCRT Simulation Fluence Rates With Respect to Experimental Irradiance Data for an Air System

5.2 COMPARISON WITH POINT SOURCE SUMMATION MODEL

In this section, estimated MCRT simulation data were compared with calculated values from the Point Source Summation (PSS) model. This model is one of the most well-recognized deterministic UV computational models despite its lack of important fluence elements such as reflection and refraction. This model is simplistic in nature and has been used by UV investigators as a reference in evaluating new UV computational models (Blatchley et al., 1997; Chiu, 1999; Bolton, 2000; Sasges et al., 2007). The PSS model used in this comparison is given by the following equation:

$$I_{(R,z)} = \sum_{i=1}^{n} \frac{P}{4\pi l_i^2 n} \exp\left[-\left(\alpha_q t_q + \alpha_w \left(R - r_q\right)\right)\frac{l}{R}\right] \qquad (5\text{-}6)$$

where $I(R,z)$ = fluence rate at a point in medium, typically water (mW/cm^2)

P = number of point sources making up the lamp

l_i = distance from the point source to a point under consideration (cm)

n = number of point sources making up the lamp

α_q = absorption coefficient of quartz (cm^{-1})

α_w = absorption coefficient of water (cm^{-1})

tq = thickness of quartz tube (cm)

R = radial distance from the lamp axis to the point under consideration (cm)

r_q = radius of the quartz tube (cm)

The term $(P/(4\pi l_i^2 n)$ represents the fluence rate of each individual point source emitted in the 4π spherical space whose center is the point considered. The first and second exponential terms represent the absortivities of UV energy from each point source by the quartz tube and the water medium, respectively. The above equation reflects the application of the inversed square law of radiation in that irradiance reduces with respect to the square of the distance from the point source. This model does not address reflection and refraction as light travels through a quartz tube, nor does it address reflections from an adjacent quartz tube surface. Thus it is intrinsically deficient compared to the proposed MCRT model.

Both the PSS model and the MCRT method share the important concept of summation of energies contributed by individual point sources making up the lamp from the lamp axis. However, the PSS is static and deterministic whereas the MCRT method

is based on probabilistic random generation and stochastic transmission of energies that follow the physical laws of radiation. Further, the fluence rate provided by each point source in the PSS model is given by $P/(4\pi l_i^2 n$, whereas that provided by the MCRT method is given by P/n. In the MCRT method, the ray tracing and sampling of fluence rates resulted in fluence rate data in the 4π spherical space; such simulated data also reflected the results of the inverse square law even though the law was not explicitly described in terms of the above expression.

In comparing results of the MCRT simulations with the above referenced model, the reflection calculation part of the MCRT code was intentionally turned off to simulate a similar condition used in the PSS model. In addition, MCRT simulation estimates with at least two million bundles were used to ensure convergence of each MCRT model run. For MCRT vs. PSS comparison, an additional computer program was developed to calculate fluence rates based on the PSS equation for the same system used in the MCRT simulations. This system includes on a low pressure lamp rated at 26,700 mW, one meter in length and a radius of 1.25 cm. The channel dimensions are 30 cm in width, 80 cm in length with 100 cm of water depth. This system is conceptually similar to the one presented in Figure 3-17.

The success of the MCRT method was again demonstrated in comparing its results with those of the PSS model. Simulation results for the same system described above are presented in Figures 5-28 through 5-33 for the distribution of fluence rates in the radial distance from the quartz sleeve surface at three different location along the length of the lamp; these locations were the lamp mid-point at 50 cm from the bottom of the channel, the near base location 5 cm from the bottom of the channel, and near top

location 95 cm from the bottom of the channel. The PSS data were based on 100 point sources. The MCRT fluence data were the average data of seven simulations with 2 million to 8 million bundles, and they represented fluence rate in the main flow direction (x) downstream from the lamp.

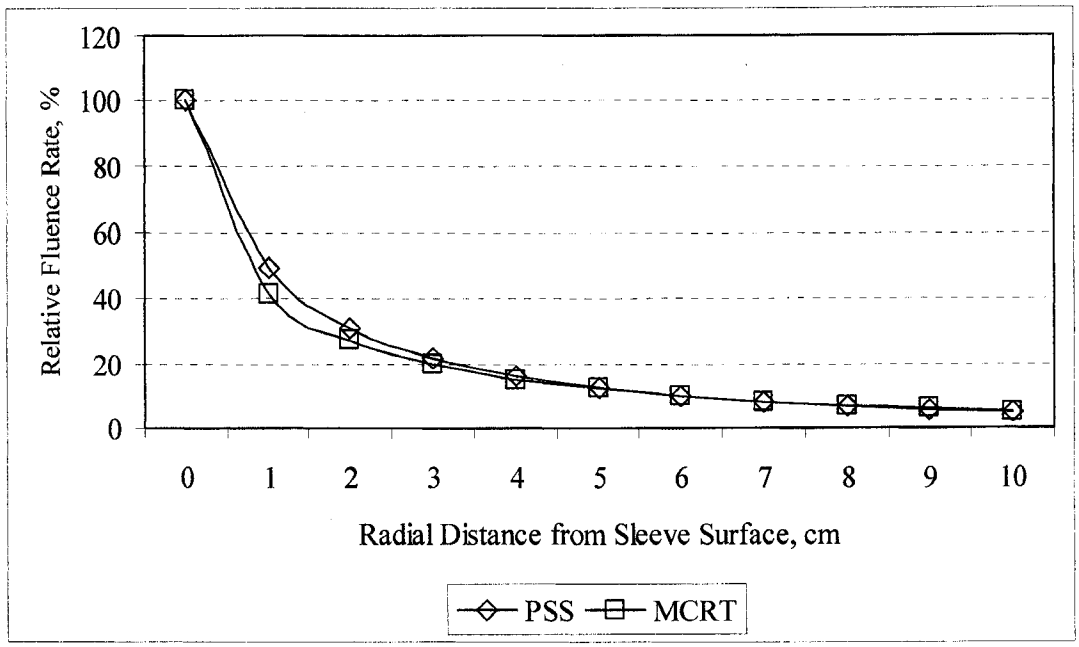

Figure 5-28. Relative Fluence Rate Distribution of PSS Model vs. MCRT Model at Lamp Mid-Point (50 cm from Base)

Two figures were presented for each location. The first figure at each location showed the relative fluence rate distribution in percentage with respect to the estimated fluence rate of the quartz sleeve surface. The second figure at each location showed estimated fluence rates at the radial distance from the sleeve surface.

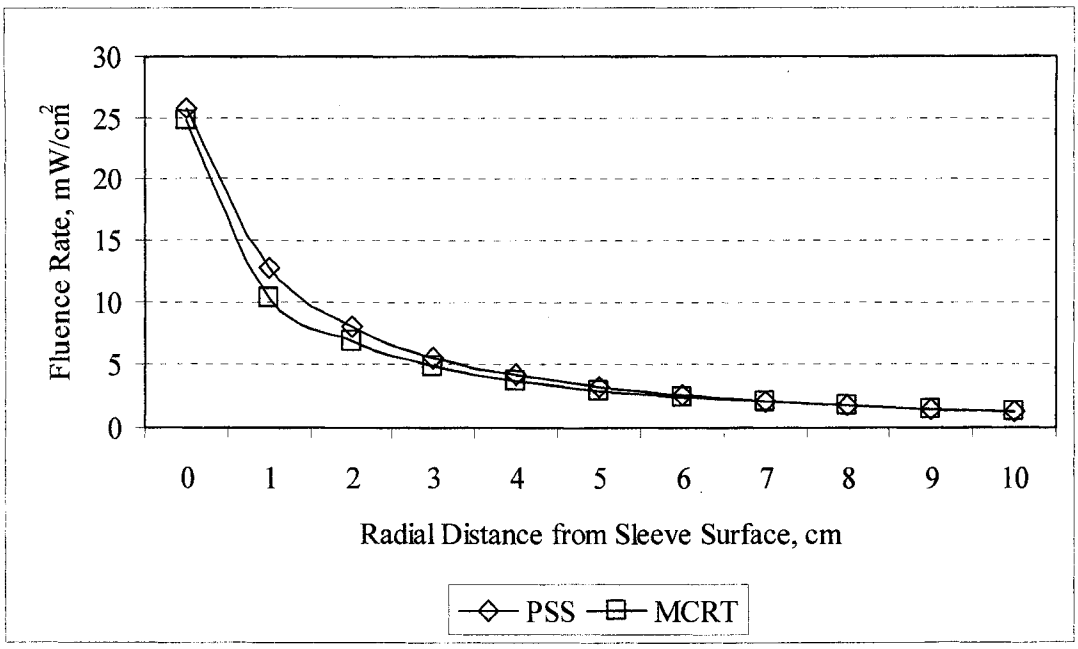

Figure 5-29. Fluence Rate Distribution of PSS Model vs. MCRT Model at Lamp Mid-Point (50 cm from Base)

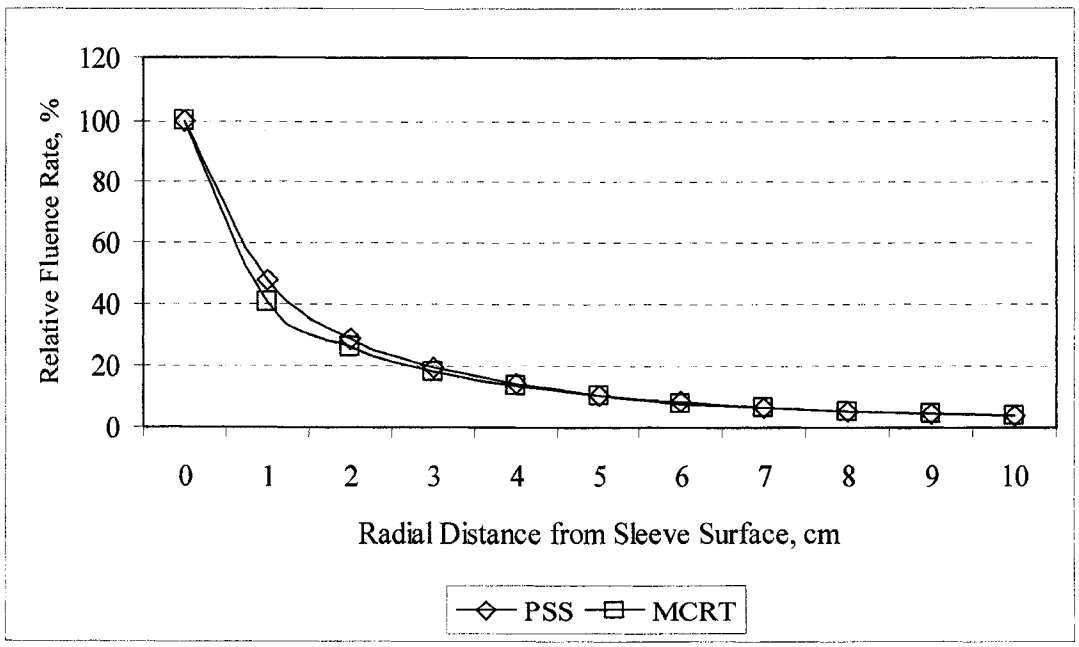

Figure 5-30. Relative Fluence Rate Distribution of PSS Model vs. MCRT Model near Base of Lamp (5 cm above Channel Bottom)

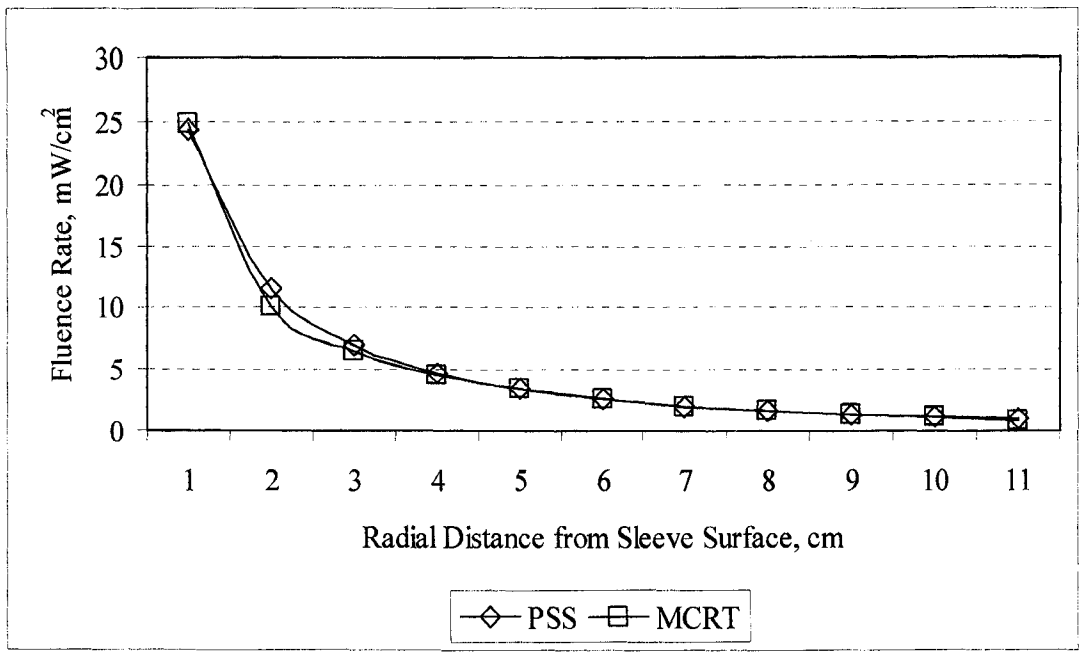

Figure 5-31. Fluence Rate Distribution of PSS Model vs. MCRT Model Near Base of Lamp (5 cm above Channel Bottom)

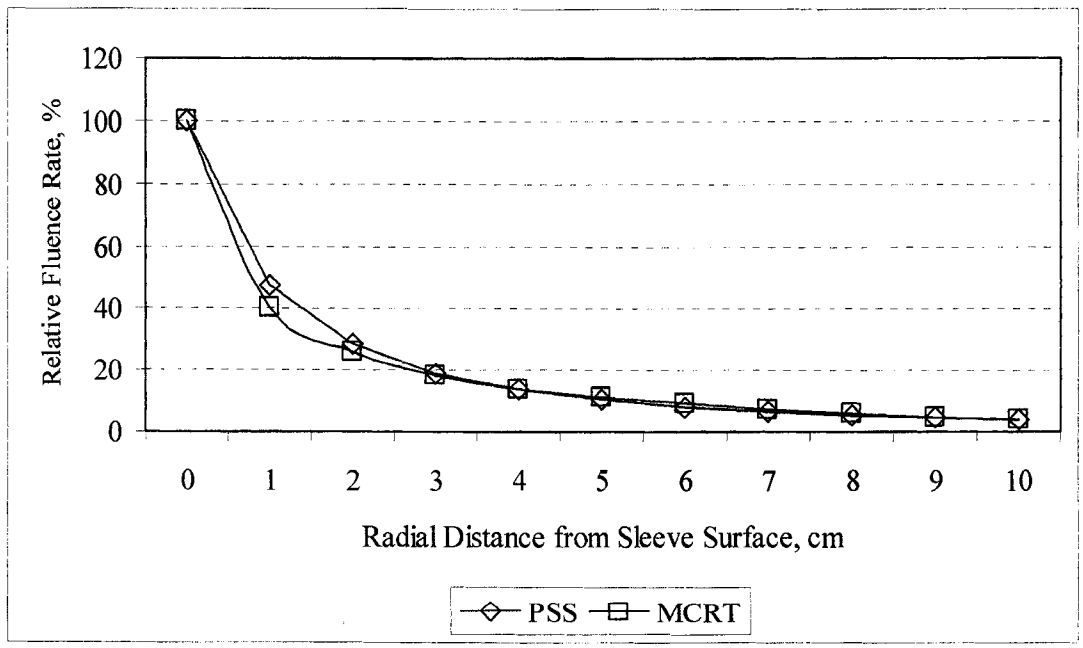

Figure 5-32. Relative Fluence Rate Distribution of PSS Model vs. MCRT Model Near Top of Lamp (95 cm above Channel Bottom)

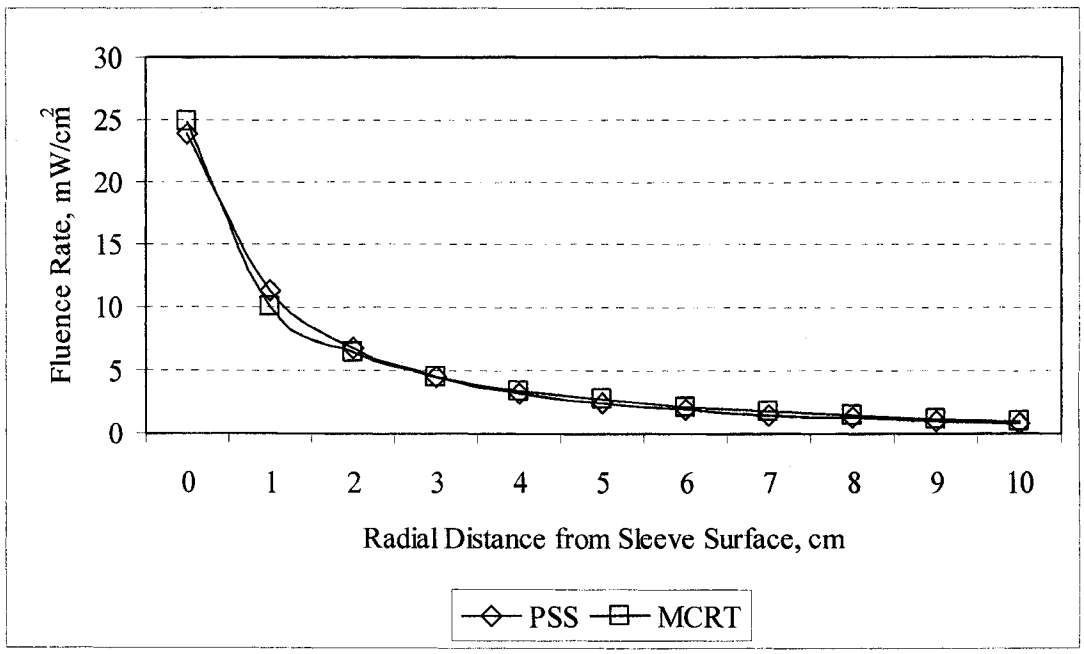

Figure 5-33. Fluence Rate Distribution of PSS Model vs. MCRT Model Near Top of Lamp (95 cm above Channel Bottom)

Excellent agreements in the percent distributions and fluence rate distributions were found in all three cases. The MCRT data were slightly lower than the PSS data in the first five centimeters from the sleeve surface due to effects of refraction and reflection through the quartz sleeve that were accounted for in the MCRT model but not in the PSS model.

In summary, results of the comparisons of MCRT simulation data with actual measurement data for water and air systems and with the PSS data confirmed that the MCRT model was capable of providing fluence rate data very close to the measurement data for the one lamp system being tested. The differences between the actinometric experimental data and corresponding MCRT data were attributed to the fact that absorption and reflection by test spheres were not included in the MCRT model due to

lack of specific information related to physical dimensions of the spheres. The differences between the irradiance measured in air and corresponding MCRT data were attributed to the fact that the UV energy measurements were limited by the scope of the lense, its curvature, and the sensor aperture; therefore, only light energies coming from limited directions were recorded by the sensor. The limitation in the scope of measurement of a sensor is more important when the sensor is placed closer to the lamp where the measurement data were lower than the MCRT data. The limitations of using actinometric spheres and sensors in obtaining fluence rates are more prevalent in UV systems with multiple lamps, where limited space is available for mounting tested spheres and sensors. In this regard, the MCRT model offers a good alternative for estimating fluence rates with comparable accuracies as demonstrated in this chapter. Finally, excellent agreements between MCRT data and PSS data were found for the one lamp system.

CHAPTER 6

RESULTS AND DISCUSSION

6.1 OVERVIEW OF MODELED SYSTEMS AND SYSTEM EVALUATION

One of the objectives of this study was to use the Monte Carlo Ray-Trace (MCRT) method to study effects of quartz sleeve surface reflection and lamp spacing on the distribution of UV fluence rates. To achieve this objective, a MCRT (Monte Carlo Ray-Tracing) computer model was developed to estimate fluence rates in a three dimensional space of different UV modeled systems consisting of two lamps, four lamps, and multiple rows with five lamps in each row with up to 25 lamps. The general layouts of the modeled systems are shown in Figures 6-1 and 6-2.

The MCRT computer model was developed based on the model for a one-lamp system as discussed in Chapter 4 with the additional component for quartz sleeve surface reflection calculations for the multiple lamp systems. The two-lamp and four-lamp systems shown in Figure 6-1 have the same lamp spacing as in the multiple- row system. The four-lamp in-line arrangement is commonly found in horizontal systems. The multiple lamp system is comparable to the pilot scale UV system studied by other investigators (Blatchley *et al.*, 1997; Chiu *et al.*, 1999; Iranpour *et al.*, 1999). Lamp and channel data used in the MCRT simulations are summarized in Table 6-1.

In evaluating each modeled system, fluence rate profiles relative to the quartz sleeve surface in both the y-direction (= cross flow direction) and x-direction (= longitudinal main flow) were evaluated. Also, fluence rate profiles across lamp centers and each row of the lamp were evaluated. Further, fluence rates along the lamp axis are

generally stable except a few centimeters near both ends of the lamp where they typically drop below the fluence rates at the other locations, as shown in Figure 6-3 for a 2-million bundle simulation. This particular trend in fluence rates was also reported in another study (Bolton, 2000). Therefore, fluence data presented in this chapter are those along the radial distance from the mid-point of the quartz sleeve. Lastly, as discussed in Chapter 4, MCRT fluence rate results of one lamp with similar specifications began to converge when the number of simulated bundles reaches 750,000 or more. To ensure the convergence of simulated fluence rates for the modeled system reviewed in this chapter, at least one million bundles were simulated for each MCRT model run.

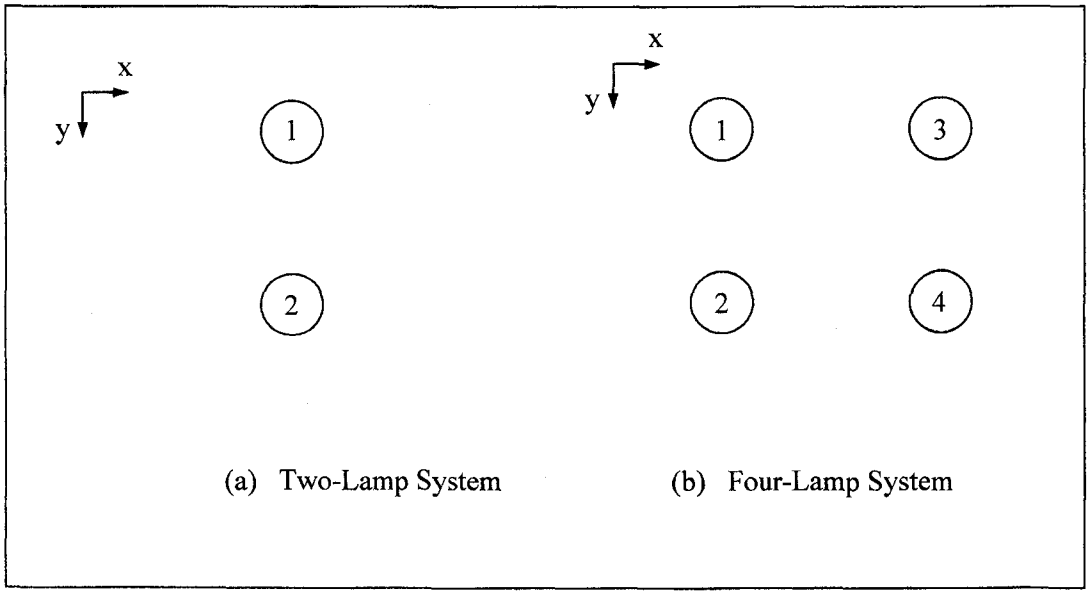

Figure 6-1. One-Lamp and Four-Lamp Systems

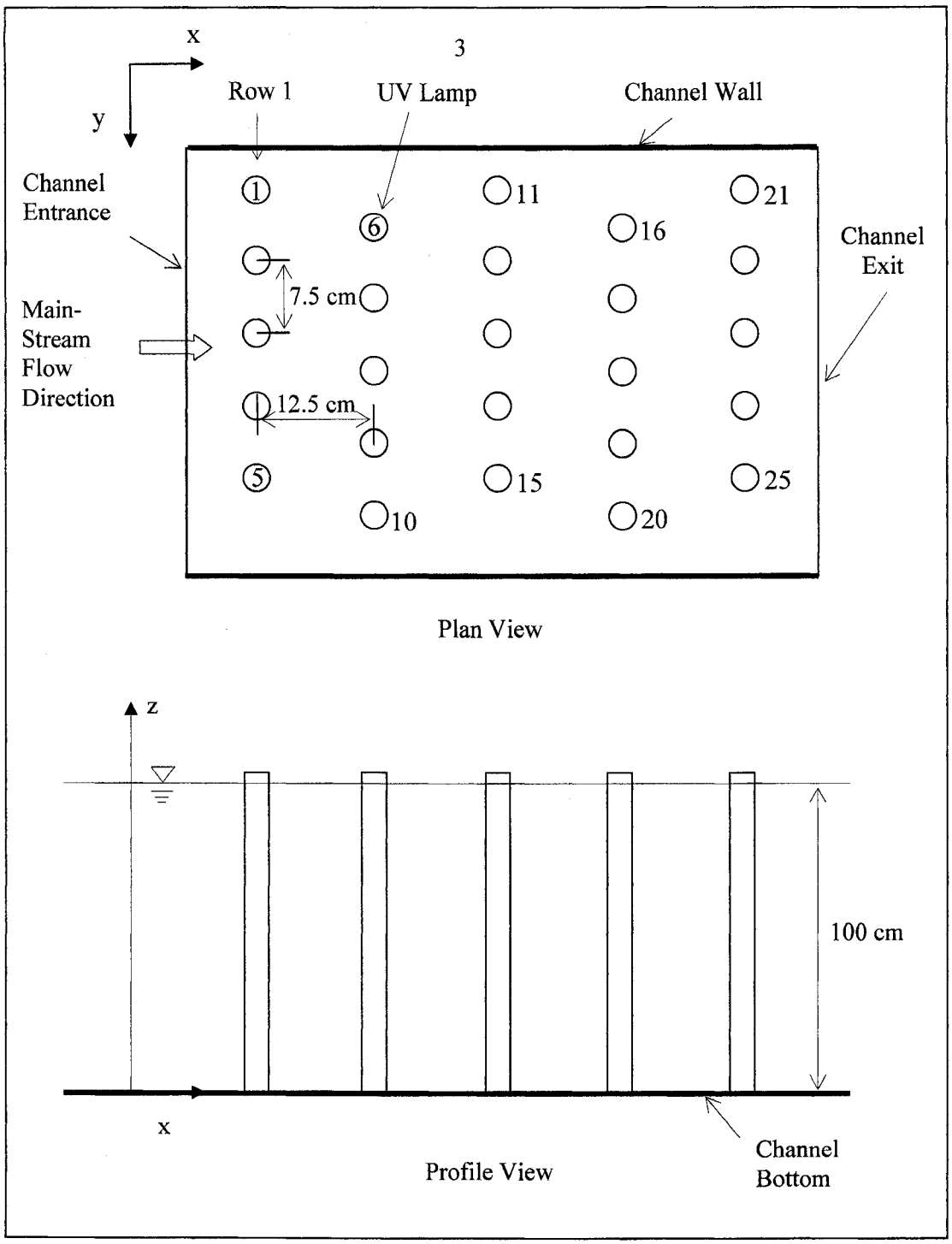

Figure 6-2. Multiple Row System

Table 6-1. Modeled System Data

Parameter	Data
Low Pressure Lamp Emitting Power	26.7 W and 40 W
Section of Lamp Length Submerged in Water	100.00 cm
Lamp Radius	0.50 cm
UVC Emitting Efficiency of Lamp	50.00 %
Quartz Sleeve Radius	1.25 cm
Quartz Sleeve Thickness	0.15 cm
UV Transmission of Water	90.00%
Absorption Coefficient of Water (90%	0.046 cm^{-1}
Absorption Coefficient of Quartz	0.048 cm^{-1}
Refractive Index of Water	1.33
Refractive Index of Quartz	1.52
Channel Width	50.00 cm
Channel Length	80.00 cm

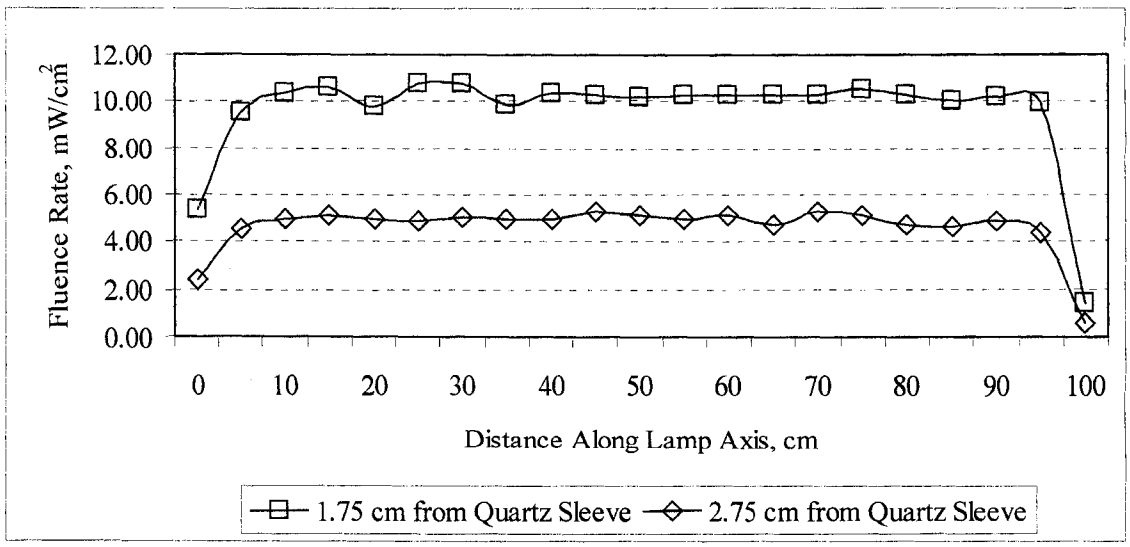

Figure 6-3. Typical MCRT Estimated Fluence Rate Distribution Along Lamp Axis

6.2 TWO-LAMP SYSTEM

6.2.1 Effects of Quartz Reflection in Two-Lamp System

MCRT simulations were conducted for a two-lamp system where two lamps were placed 6.5 cm, 7.5 cm, and 8.5 cm apart in water. To evaluate potential effects of reflection from outside the quartz sleeve surface, the MCRT model was simulated with and without reflection calculations so that a total of six MCRT model runs were performed. Lamp location data used in the simulations are shown in Figure 6-4

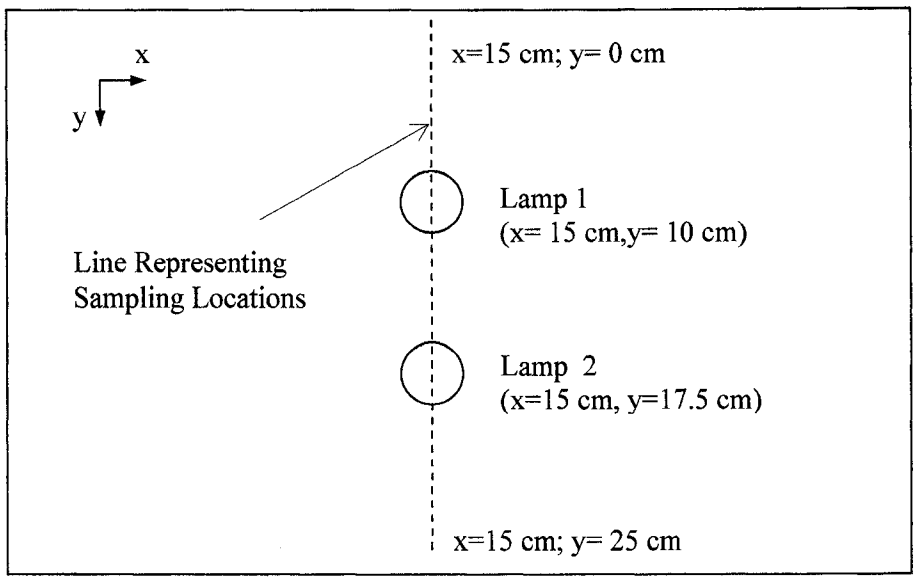

Figure 6-4. Lamp and Sampling Locations in Two-Lamp System

Estimated fluence rates for the system with two 26.7 W lamps placed 7.5 cm apart are presented in Figure 6-5. The horizontal axis of the figure, which represents the radial distance from the quartz sleeve surface of each lamp, corresponds to the dotted line in the y direction shown in Figure 6-4. The locations denoted with "0" cm correspond to the

lamp's location. Figure 6-5 indicates that the fluence rate distributions of the cases with and without reflection from quartz sleeve surfaces are very close to each other. However, the figure equally shows a clear difference in fluence rates along the area where energy bundles from two lamps overlap (i.e., the concave portion in the middle of Figure 6-5) compared with fluence rate distribution from a single lamp. Such difference is due to a higher density of energy bundles in the area between the lamps. Finally, the simulation results shown in Figure 6-5 indicate that fluence rates in the radial distances outside the distance between two lamps drop significantly at 4 cm and more from the quartz sleeve surface.

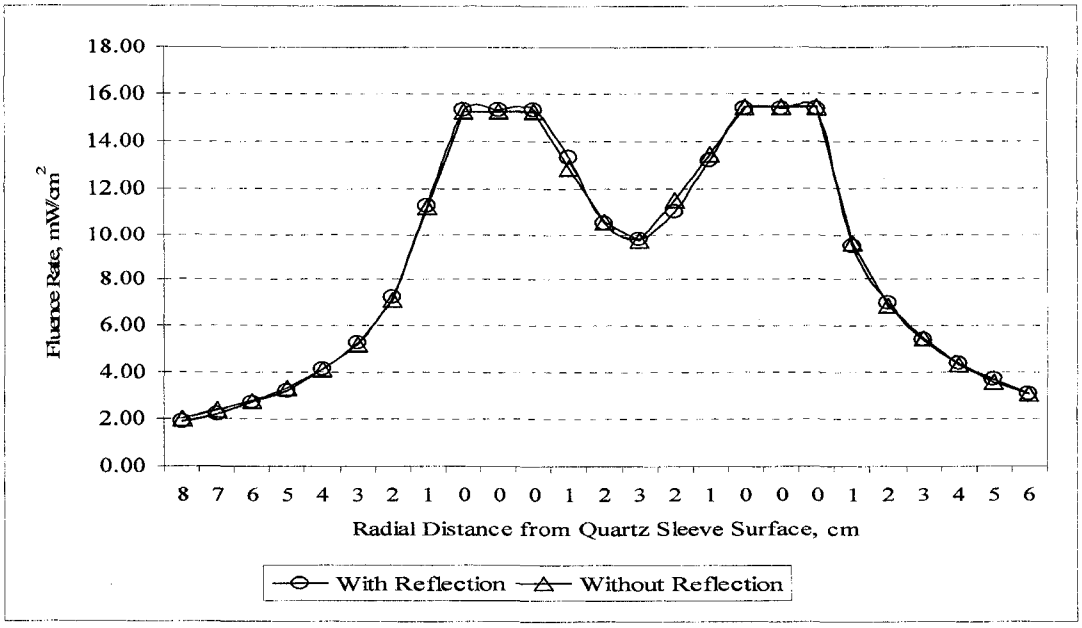

Figure 6-5. MCRT Estimated Fluence Rates for Cases With vs. Without Reflection for Two-Lamp System with 26.7 W Lamps

Table 6-2 lists estimated MCRT fluence rates for the radial direction along the dotted line shown in Figure 6-2. Values shown in column 1 corresponded to the radial distance from the closest quartz tubes associated with Lamp 1 and Lamp 2, and number zero corresponded to the locations of the lamps. Subsequently, the last column represents the differences between 'without-reflection' and 'with-reflection' values. Both negative and positive values were found from the subtraction. These results indicated that both sets of data were approximately the same and that effects of reflections were negligible.

The small differences between fluence rate values with and without reflection were attributed to small reflectivities estimated by the model that range from 0.004 to 0.038. A sample of 30 reflectivity values for various incident and reflection angles at a quartz tube surface is shown in Table 6-3. Furthermore, after leaving the lamp, energies of a bundle drop significantly at radial distances a few centimeters from the quartz tube from which they originate; the amount of energy reflected from another quartz surface would become insignificant. In general, the above results indicated that the contribution of reflection from the quartz sleeve surfaces is negligible for the two-lamp system under consideration.

Table 6-2. Comparison of MCRT Estimated Fluence Rates With and Without Reflection For Two-Lamp System

y Coordinate cm	Distance from Quartz Sleeve cm	Fluence Rate, mW/cm^{2} (*)		
		With Reflection	Without Reflection	Difference
0	9	0.45	0.38	0.07
1	8	1.86	1.99	-0.12
2	7	2.21	2.41	-0.20
3	6	2.68	2.78	-0.09
4	5	3.22	3.32	-0.11
5	4	4.14	4.11	0.03
6	3	5.30	5.21	0.09
7	2	7.21	7.06	0.15
8	1	11.24	11.14	0.11
9 (Lamp 1)	0	15.28	15.21	--
10 (Lamp 1)	0	15.28	15.21	--
11 (Lamp 1)	0	15.28	15.21	--
12	1	13.30	12.84	0.46
13	2	10.49	10.51	-0.01
14	3	9.77	9.70	0.07
15	2	10.99	11.47	-0.49
16	1	13.17	13.44	-0.27
17 (Lamp 2)	0	15.36	15.41	--
18 (Lamp 2)	0	15.36	15.41	--
19 (Lamp 2)	0	15.36	15.41	--
20	1	9.46	9.58	-0.11
21	2	6.96	6.84	0.12
22	3	5.36	5.43	-0.06
23	4	4.40	4.32	0.08
24	5	3.70	3.61	0.10
25	6	3.08	3.05	0.03

(*) 1.5 Million Bundle Simulations

Table 6-3. A Sample of MCRT Estimated Reflectivity Values for Various Incidence and Reflected Angles

Incident Angle (degrees)	Refraction Angle (degrees)	Reflectivity
45.63	38.71	0.007
22.27	19.36	0.005
17.62	15.36	0.004
19.75	17.19	0.004
15.72	13.71	0.004
21.77	18.94	0.005
17.66	15.39	0.004
38.02	32.61	0.006
29.61	25.61	0.005
62.59	50.97	0.028
54.23	45.23	0.013
25.63	22.24	0.005
20.93	18.22	0.005
65.35	52.68	0.038
46.46	39.37	0.008
19.08	16.62	0.004
15.35	13.39	0.004
23.21	20.17	0.005
16.99	14.81	0.004
33.53	28.9	0.005
27.22	23.59	0.005
61.7	50.39	0.026
53.62	44.79	0.012
37.61	32.27	0.005
29.33	25.38	0.005
13.32	11.63	0.004
8.56	7.49	0.004
18.33	15.97	0.004
14.8	12.92	0.004
19.81	17.25	0.004

6.2.2 Effects of Lamp Spacing in Two-Lamp System

Effects of lamp spacing on fluence rate data were evaluated by generating MCRT fluence data with reflection for three center-to-center lamp spacings at 6.7 cm, 7.5 cm, and 8.5 cm. In all three cases, the position of Lamp 1 and its quartz sleeve were unchanged while the position of Lamp 2 and its quartz sleeve was adjusted along the y-direction to achieve the above spacing specifications. Distributions of fluence rates in y-direction radial locations are shown in Figure 6-6. In the figure, data indicates that the minimum fluence rate between two lamps associated with the 8.5 cm spacing (at radial distance 11 to 15 cm) was increased by approximately 1 mW/cm^2 at the 7.5 cm spacing and by approximately 3 mW/cm^2 at the 6.5 cm spacing rate, indicating an inversely proportional correlation between the distance and the minimum fluence rate. The fluence rates in the radial distance outside the area between the lamps were not affected by the lamp spacing.

Fluence data shown in Figure 6-6 are listed in Table 6-4. In the first column, the radial distances of 9 to 11 cm corresponded to the approximate location of Lamp 1, for which the fluence rates were the average fluence rate at the quartz tube of the lamp. The approximate locations of Lamp 2 for lamp spacings 6.5 cm, 7.5 cm, and 8.5 cm were at the radial distance of 15 to 17 cm, 16 to 18 cm, and 17 to 19 cm, respectively.

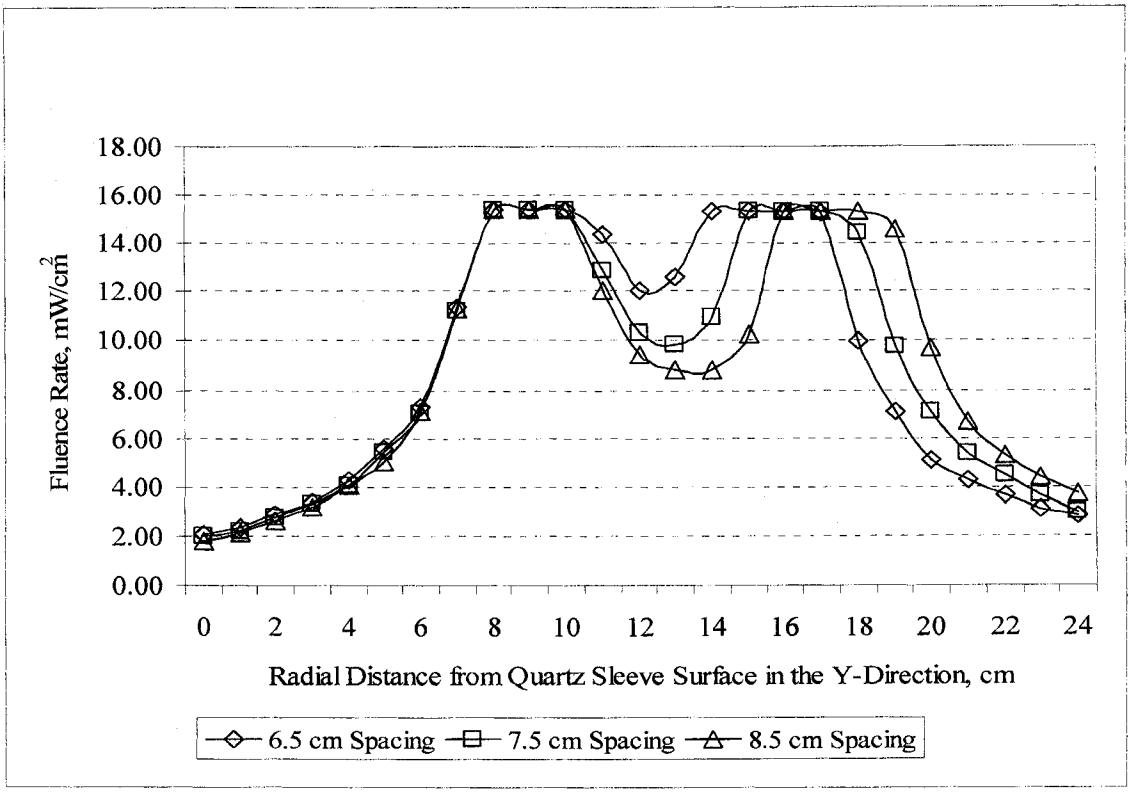

Figure 6-6. Comparison of MCRT Estimated Fluence Rates at Difference Lamp Spacings for Two-Lamp System

The increased fluence rates in the space between Lamp 1 and Lamp 2 illustrated in Figure 6-6 were apparently attributed to the contribution of energies from both lamps in this area. Such increase would be useful in improving UV dose and disinfection efficiency when any increase in head loss is tolerable. Table 6-5 and Figure 6-6 show that the MCRT model's effectiveness and flexible applicability in quantifying changes in fluence rates at different locations for a specified range of lamp spacing for typical UV systems.

Table 6-4. Comparison of MCRT Estimated Fluence Rates for Different Lamp Spacing for Two-Lamp System

y Coordinate cm	Distance from Quartz Sleeve cm	Lamp Spacing (*)		
		6.5 cm	7.5 cm	8.5 cm
0	9	0.40	0.37	0.42
1	8	2.06	2.02	1.75
2	7	2.34	2.21	2.12
3	6	2.91	2.76	2.60
4	5	3.38	3.32	3.13
5	4	4.23	4.08	4.08
6	3	5.57	5.44	5.00
7	2	7.32	7.02	7.09
8	1	11.36	11.22	11.25
9 (Lamp 1)	0	15.41	15.41	15.41
10 (Lamp 1)	0	15.41	15.41	15.41
11 (Lamp 1)	0	15.41	15.41	15.41
12	1	14.37	12.88	12.02
13	2	12.04	10.28	9.45
14	3	12.55	9.84	8.82
15 (Lamp 2)	2	15.32	10.91	8.83
16 (Lamp 2)	1	15.32	15.32	10.24
17 (Lamp 2)	0	15.32	15.32	15.32
18	0	15.25	15.32	15.32
19	0	9.98	14.42	15.32
20	1	7.10	9.74	14.55
21	2	5.10	7.05	9.67
22	3	4.26	5.39	6.66
23	4	3.63	4.49	5.27
24	5	3.06	3.66	4.37
25	6	2.82	2.97	3.71

(*) 1.5 Million Bundle Simulations

6.2.3 Effects of Lamp Shadow in Two-Lamp System

Potential effects of lamp shadow in the two-lamp system were evaluated by simulating the MCRT model with and without shadow effects under a condition that is without reflection from a quartz surface. To calculate fluence rates reflecting shadow effect, the following radial distance relationship was incorporated into the two-lamp MCRT computer program:

$$(x_{i+1} - x_c)^2 + (y_{i+1} - y_c)^2 = r_{i+1} \qquad (6\text{-}1)$$

where x_{i+1}, y_{i+1}= x and y coordinate of the head of a bundle in a 1 cm volume element, as described in Figure 15.

xc, yc = x and y coordinates of the center of a lamp.

r_{i+1} = radial distance from the head of the bundle to the center of the lamp.

If the radial distance, r_{i+1}, is less than the quartz sleeve radius, the bundle is considered to hit the quartz tube and to be absorbed by the quartz tube. When the case without shadowing effects is considered, the bundle travels through the quartz tube as well as the lamp as if these two components were not present.

Fluence data and related radial distance in the y-direction identified in Figure 6-6 are illustrated in Figure 6-7 and listed in Table 6-5. The data listed in the last column in Table 6-5 represent fluence rate differences between with and without shadow calculations in the MCRT model. The negative values of the fluence rate differences suggested that fluence rates with shadow were consistently lower than those without shadow in the area outside that between the lamps. As illustrated in Figure 6-7, the shape of the fluence rate distributions in both cases follow closely with each other with slight

differences in fluence rates as discussed above. The case with shadow effects is considered more representative of real conditions of the UV system, and the MCRT model is the first model capable of simulating such effects. On the contrary, none of the existing UV fluence models can describe such effects.

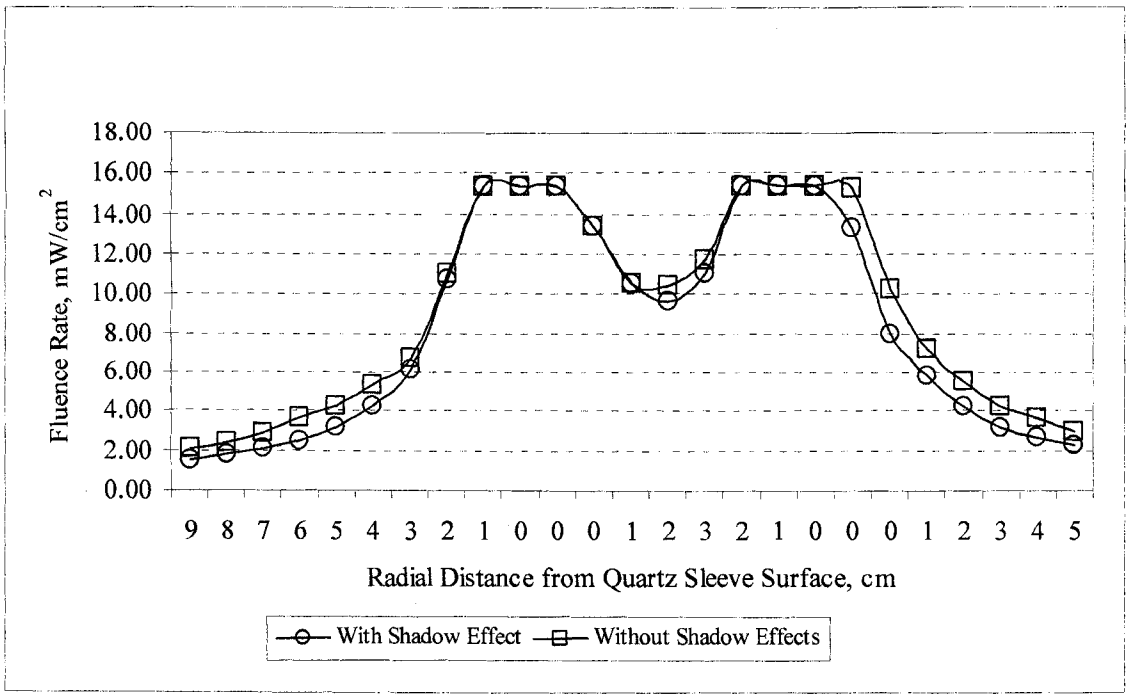

Figure 6-7. Estimated Fluence Rates for Cases With vs. Without Shadow Effects for Two-Lamp System

Table 6-5. Comparison of MCRT Estimated Fluence Rates for Cases With and Without Lamp Shadow for Two-Lamp System

y-Coordinate cm	Distance from Quartz Sleeve, cm	Fluence Rate (*), mW/cm^2		Difference mW/cm^2
		With Shadow	Without Shadow	
1	9	1.46	2.09	-0.63
2	8	1.73	2.39	-0.65
3	7	2.09	2.87	-0.78
4	6	2.48	3.67	-1.19
5	5	3.11	4.22	-1.11
6	4	4.22	5.32	-1.09
7	3	6.10	6.66	-0.56
8	2	10.70	10.99	-0.28
9 (Lamp 1)	1	15.31	15.31	0.00
10 (Lamp 1)	0	15.31	15.31	0.00
11 (Lamp 1)	0	15.31	15.31	0.00
12	0	13.33	13.40	-0.07
13	1	10.49	10.50	-0.01
14	2	9.68	10.45	-0.77
15 (Lamp 2)	3	11.01	11.70	-0.69
16 (Lamp 2)	2	15.31	15.31	0.00
17 (Lamp 2)	1	15.31	15.31	0.00
18 (Lamp 2)	0	15.31	15.31	0.00
19	0	13.31	15.20	-1.90
20	0	7.94	10.19	-2.25
21	1	5.78	7.17	-1.39
22	2	4.26	5.51	-1.26
23	3	3.18	4.27	-1.09
24	4	2.69	3.60	-0.90
25	5	2.24	2.99	-0.76

(*) 1.5 Million Bundles per Lamp.

6.3 FOUR-LAMP SYSTEMS

Fluence rates in a four-lamp system with lamps in an in-line arrangement and a staggered arrangement were evaluated. The in-line arrangement is typically found in horizontal UV systems in which lamps are oriented horizontally, and the staggered

arrangement is typically found in vertical UV systems in lamps oriented vertically. Such arrangement would not affect the coordinate system used in the MCRT model.

A schematic of these systems is shown in Figure 6-8 with the original lamp coordinates. Figure 6-7 also illustrates approximated sampling locations along the y-direction (across the center of Lamps 1 and 2) and x-direction (on both sides of Lamps 1 and 3). These four MCRT sampling locations were chosen to evaluate the effects of quartz surface reflection and spacing evaluated in this section.

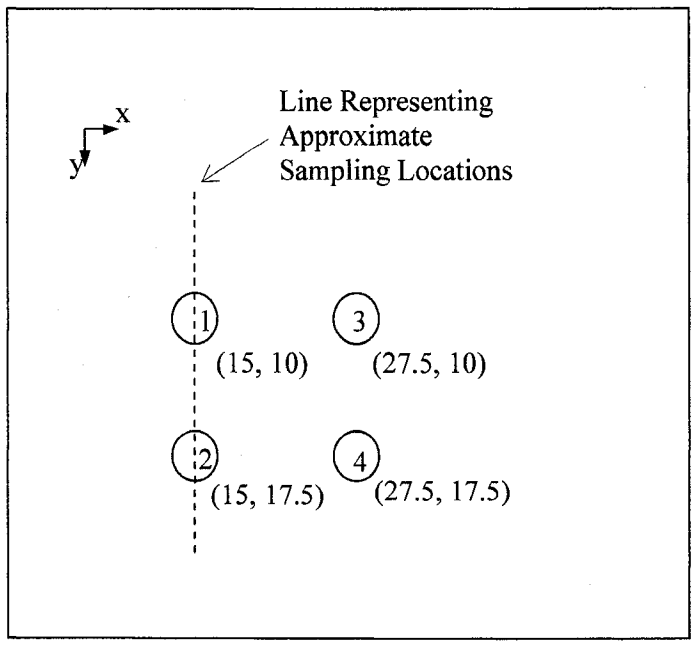

Figure 6-8. Lamp and Sampling Locations in Four-Lamp Systems

6.3.1 Effects of Quartz Reflection in Four-Lamp System

Potential effects of quartz reflection in the four-lamp system were evaluated by estimating fluence rates for the cases with and without reflection calculations in the MCRT model. Estimated fluence rates in the y-direction along sampling line 1 across the center of Lamp 1 and Lamp 2 as shown in Figure 6-8 are listed in Table 6-6 and illustrated in Figure 6-9. The data listed in the last column in Table 6-6 represent fluence rate differences between without and with reflection in the MCRT model. There are slight increases in fluence rates in the area between Lamp 1 and Lamp 2, represented by positive values in the last column of Table 6-6. These increases ranged from 0.1 mW/cm^2 (0.8 percent) at the y-coordinate and 15 cm to 1.16 mW/cm^2 (9 percent) at y-coordinate 14 cm. Such increases are illustrated in Figure 6-9. As also indicated in Figure 6-6, fluence rates in other radial distances were essentially the same for both cases.

Table 6-6. Comparison of MCRT Estimated Fluence Rates With and Without Reflection for Four-Lamp System

y-Coordinate cm	Distance from Quartz Sleeve cm	Fluence Rate, $mW/cm^{2(*)}$		
		With Reflection	Without Reflection	Difference
0	9	1.06	1.21	-0.15
1	8	2.84	2.87	-0.03
2	7	3.36	3.29	0.07
3	6	3.77	3.79	-0.02
4	5	4.91	4.54	0.37
5	4	5.48	5.53	-0.05
6	3	6.83	6.79	0.04
7	2	8.35	8.92	-0.56
8	1	11.90	12.01	-0.11
9 (Lamp 1)	0	15.45	15.10	--
10 (Lamp 1)	0	15.45	15.10	--
11 (Lamp 1)	0	15.45	15.10	--
12	1	14.85	14.24	0.61
13	2	12.43	12.13	0.30
14	3	12.60	11.44	1.16
15	2	12.77	12.67	0.10
16	1	14.11	13.89	0.22
17 (Lamp 2)	0	15.45	15.10	--
18 (Lamp 2)	0	15.45	15.10	--
19 (Lamp 2)	0	15.45	15.10	--
20	1	8.38	10.60	-2.22
21	2	6.81	7.92	-1.11
22	3	5.35	6.45	-1.10
23	4	4.86	5.29	-0.44
24	5	4.27	4.79	-0.52
25	6	3.87	3.84	0.03

(*) 1.0 Million Bundle Simulations per Lamp.

Compared with that in the two-lamp system, a significant reduction in the difference between the minimum fluence rates (at the mid-point of the radial distance between the lamps) and maximum fluence rates (at quartz tube surfaces) was found in the

case of the four-lamp system. The difference between maximum and minimum in the four-lamp system was approximately 1.5 mW/cm^2 (Figure 6-9), whereas the difference between maximum and minimum in the two-lamp system was 5.5 mW/cm^2 (Figure 6-5). Thus, reduction of the difference in fluence rates made by the four-lamp system was 4.0 mW/cm^2. Such reduction in difference in fluence rates and the increased fluence rates were attributed to the contribution of four lamps.

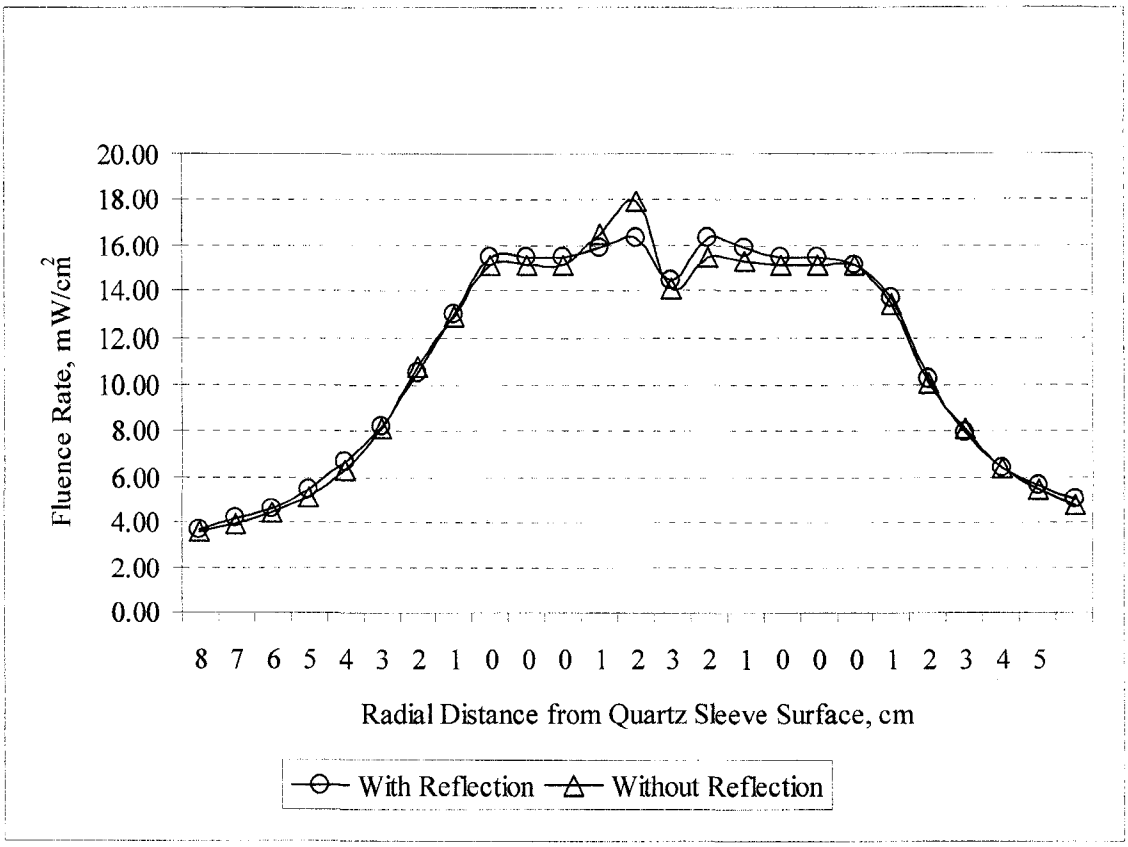

Figure 6-9. MCRT Estimated Fluence Rates for Cases With vs. Without Reflection for Four-Lamp System

6.3.2 Effects of Lamp Spacing in Four-Lamp System

Three lamp spacings of 6.5 cm, 7.5 cm. and 8.5 cm between the centers of Lamp 1 and Lamp 2 were used in the MCRT program to estimate fluence rates for the in-line four-lamp system. In adjusting the lamp spacing, the location of Lamps 1 and 3 were kept unchanged while the center coordinates of Lamps 2 and 4 were changed along the y direction based on the spacing specifications of 6.5 cm and 8.5 cm.

Estimated fluence rate data are listed in Table 6-7 and illustrated in Figure 6-10 for the radial distance in the y direction identified by Line 1 in Figure 6-8 through the centers of Lamps 1 and 2. In Table 6-7, distance zero from the quartz sleeve corresponded to the location of the lamps and quartz tube, for which fluence rates were those on the quartz sleeve surface, as estimated by the MCRT model. As illustrated in Figure 6-10, an increase of approximately 2 mW/cm^2 was found at the mid-point of the radial distance between the lamps as a result of changing the lamp spacing from 8.5 cm to 6.5 cm. This increase was less than that in the two-lamp system because fluence rates in the locations between the lamps in the four-lamp system were already higher than the corresponding fluence rates observed in the two-lamp system. As the number of lamps increases, the effect of lamp spacing may become less prominent (or a contributing factor toward resulting fluence rates).

Table 6-7. MCRT Estimated Fluence Rates for Different Lamp Spacings for Four-Lamp System

y Coordinate cm	Distance from Quartz Sleeve cm	Lamp Spacing (*)		
		6.5 cm	7.5 cm	8.5 cm
0	9	0.40	0.37	0.42
1	8	2.06	2.02	1.75
2	7	2.34	2.21	2.12
3	6	2.91	2.76	2.60
4	5	3.38	3.32	3.13
5	4	4.23	4.08	4.08
6	3	5.57	5.44	5.00
7	2	7.32	7.02	7.09
8	1	11.36	11.22	11.25
9 (Lamp 1)	0	15.41	15.41	15.41
10 (Lamp 1)	0	15.41	15.41	15.41
11 (Lamp 1)	0	15.41	15.41	15.41
12	1	14.37	12.88	12.02
13	2	12.04	10.28	9.45
14	3	12.55	9.84	8.82
15 (Lamp 2)	2	15.32	10.91	8.83
16 (Lamp 2)	1	15.32	15.32	10.24
17 (Lamp 2)	0	15.32	15.32	15.32
18 (Lamp 2)	0	15.25	15.32	15.32
19 (Lamp 2)	0	9.98	14.42	15.32
20	1	7.10	9.74	14.55
21	2	5.10	7.05	9.67
22	3	4.26	5.39	6.66
23	4	3.63	4.49	5.27
24	5	3.06	3.66	4.37
25	6	2.82	2.97	3.71

(*) 1.0 Million Bundle Simulations per Lamp.

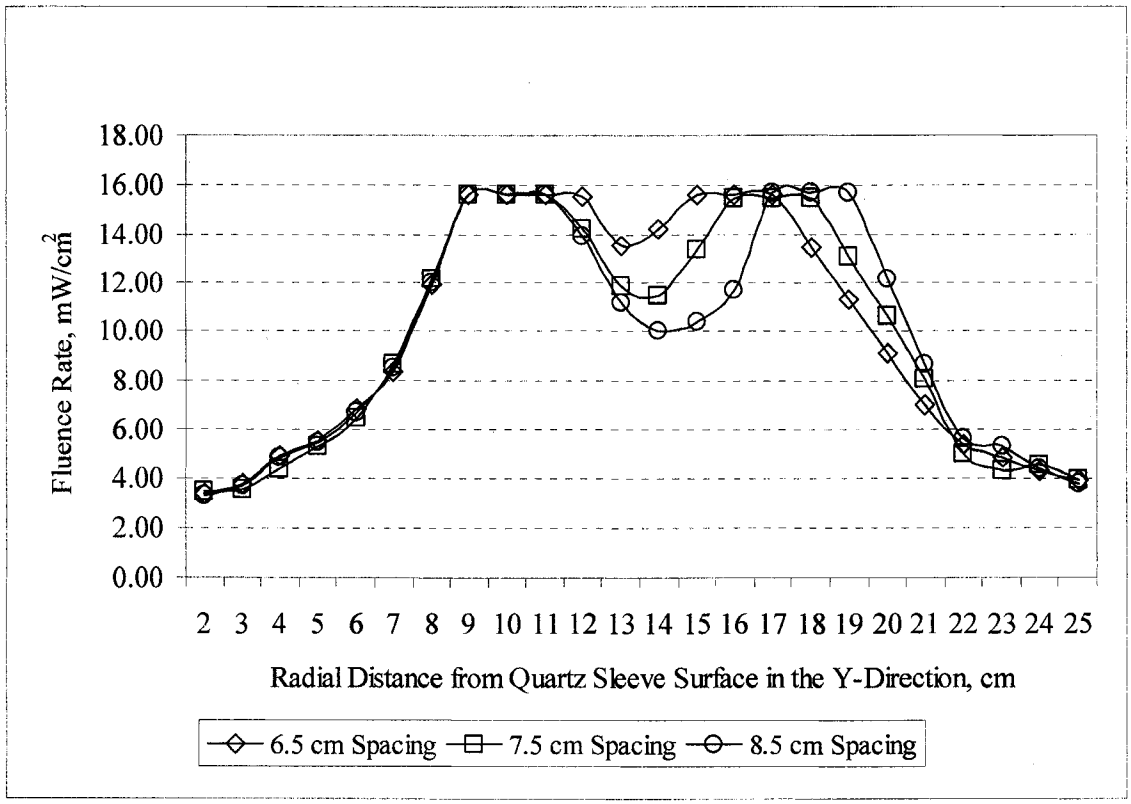

Figure 6-10 Comparison of MCRT Estimated Fluence Rates at Difference Lamp Spacings for Four-Lamp System

6.4 MULTIPLE-ROW SYSTEMS

In this section, effects of quartz surface reflection on fluence rates of a system with five rows with five lamps in each row were evaluated. A schematic of the five-row system is provided in Figure 6-11 including lamp locations, row locations, and MCRT sampling locations. This section evaluates the potential effects of quartz surface reflection on fluence rates and distributions of fluence rate with reflections at the sampling locations along dotted lines 1 through 6 as identified in Figure 6-11.

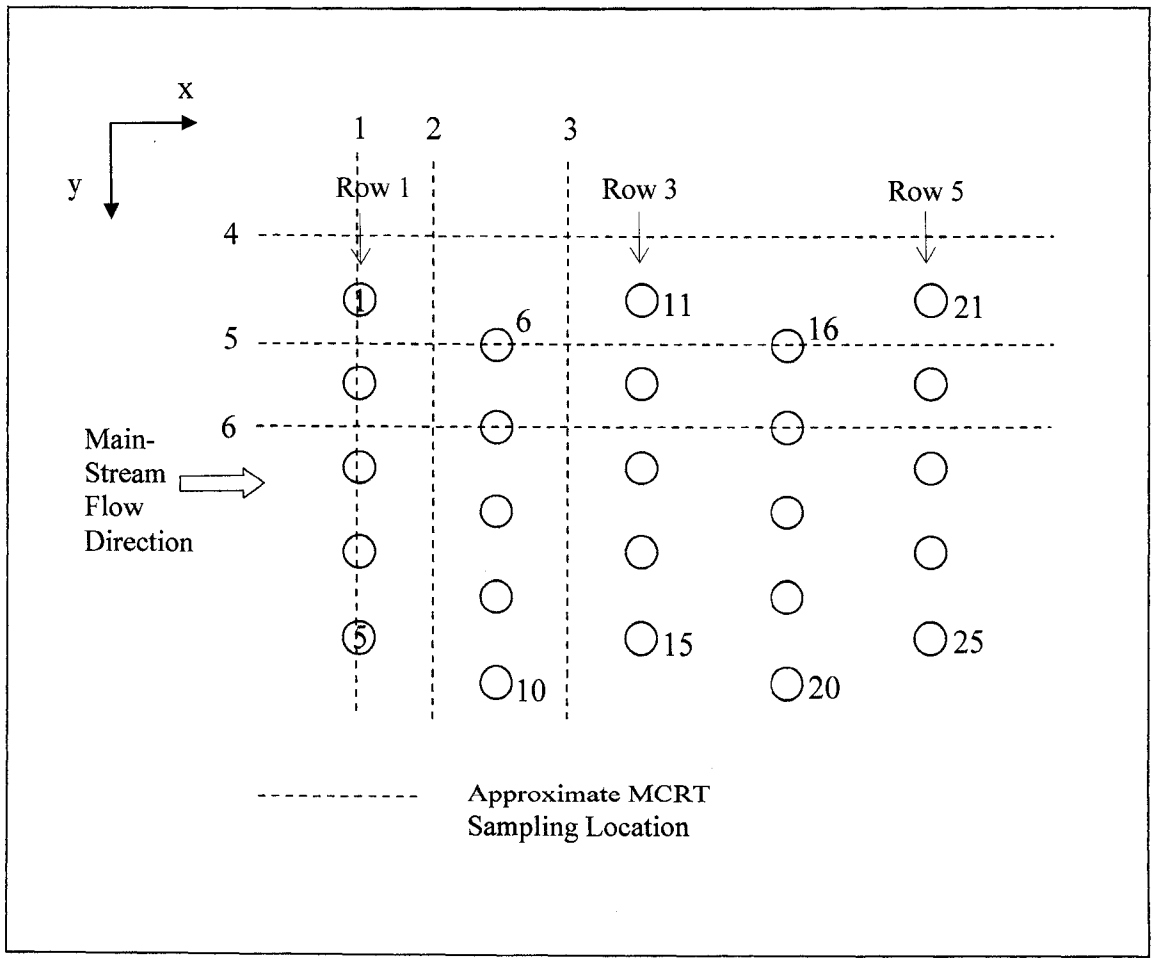

Figure 6-11. Lamp and MCRT Sampling Location of Multiple Row System

6.4.1 Effects of Quartz Surface Reflection on Fluence Rates in Five-Row System

The potential effects of quartz surface reflection on fluence rates in the five-row system were evaluated using the MCRT model to estimate fluence rates in the three dimensional space of the system for the cases with and without reflection. One million bundles per lamp, a total of twenty five million bundles, were simulated for each of the simulations. Estimated fluence rates for both cases are listed in Table 6-8 for radial distance in the y-direction along Line 1 across Row 1 (Lamp 1 (L1) to Lamp 5 (L5)) in Figure 6-12.

In Table 6-8, the data in the fifth column represent the difference in fluence rate data between non-reflection and reflection cases. The last column in Table 6-8 lists the percent difference relative to the fluence rates for the non-reflection case, except for the lamp locations where no comparison was necessary. A positive percent difference indicates an increase in fluence rates potentially due to the contribution of reflection from a quartz surface. The data indicate that there were slight increases in fluence rates at radial distances between Lamps 2 and 3 and Lamps 3 and 4, ranging from 0.1 percent to 5 percent. Such increases are considered insignificant and do not provide clear evidence of the contribution of reflection effects in increasing fluence rates in the radial area between two adjacent lamps in this system.

The profiles of fluence rate in the y-direction across the center line of Row 1 for both cases are illustrated in Figure 6-12. The profiles again indicate that there was no significant contribution of reflection effects on quartz surface on fluence rates for this system setup.

Table 6-8. Comparison of MCRT Estimated Fluence Rates With and Without Reflection for Five-Row System

y-Coordinate cm	Distance from Quartz Sleeve cm	Fluence Rate(*), mW/cm^2			
		With Reflection	Without Reflection	Difference	Perc. Difference
1	8	4.2	4.1	0.14	3.52
2	7	4.9	4.5	0.44	9.89
3	6	5.4	5.3	0.10	1.96
4	5	6.2	5.6	0.60	10.73
5	4	7.3	7.2	0.11	1.48
6	3	8.3	8.4	-0.04	-0.43
7	2	10.4	10.8	-0.42	-3.93
8	1	13.0	13.2	-0.21	-1.60
9 (Lamp 1)	0	15.6	15.6	0.00	0.00
10 (Lamp 1)	0	15.6	15.6	0.00	0.00
11 (Lamp 1)	0	15.6	15.6	0.00	0.00
12	1	17.6	17.4	0.27	1.57
13	2	15.2	15.4	-0.17	-1.13
14	3	15.0	15.4	-0.40	-2.61
15	2	16.5	16.6	-0.07	-0.45
16	1	18.6	18.6	-0.03	-0.15
17 (Lamp 2)	0	15.7	15.7	0.00	0.00
18 (Lamp 2)	0	15.7	15.7	0.00	0.00
19 (Lamp 2)	0	15.7	15.7	0.00	0.00

Table 6-8 (Continued)

y-Coordinate cm	Distance from Quartz Sleeve, cm	Fluence Rate, mW/cm^2			
		With Reflection	Without Reflection	Difference	Perc. Difference
17 (Lamp 2)	0	15.7	15.7	0.00	0.00
18 (Lamp 2)	0	15.7	15.7	0.00	0.00
19 (Lamp 2)	0	15.7	15.7	0.00	0.00
20	1	18.2	18.4	-0.22	-1.20
21	2	17.2	16.6	0.62	3.73
22	2	17.7	16.9	0.86	5.07
23	1	16.7	16.3	0.43	2.63
24 (Lamp 3)	0	15.7	15.7	0.00	--
25 (Lamp 3)	0	15.7	15.7	0.00	--
26 (Lamp 3)	0	15.7	15.7	0.00	--
27	1	20.7	20.7	0.02	0.08
28	2	18.0	17.7	0.29	1.61
29	3	16.9	16.8	0.12	0.71
30	2	18.3	18.6	-0.22	-1.19
31	1	17.1	17.2	-0.11	-0.64
32 (Lamp 4)	0	15.8	15.8	0.00	--
33 (Lamp 4)	0	15.8	15.8	0.00	--
34 (Lamp 4)	0	15.8	15.8	0.00	--
35	1	18.1	17.9	0.24	1.34
36	2	16.4	16.5	-0.09	-0.52
37	2	16.0	16.1	-0.11	-0.67
38	1	15.9	15.9	-0.05	-0.34
39 (Lamp 5)	0	15.7	15.7	0.00	--
40 (Lamp 5)	0	15.7	15.7	0.00	--
41 (Lamp 5)	0	15.7	15.7	0.00	--
42	1	15.9	16.2	-0.26	-1.62
43	2	12.6	12.6	0.02	0.15
44	3	9.9	9.9	-0.04	-0.45
45	4	8.3	8.3	-0.01	-0.08
46	5	7.2	7.5	-0.26	-3.47
47	6	6.2	6.4	-0.21	-3.22
48	7	6.1	5.8	0.34	5.79
49	8	5.4	5.5	-0.12	-2.25

(*) 1 Million Bundle Simulations per Lamp.

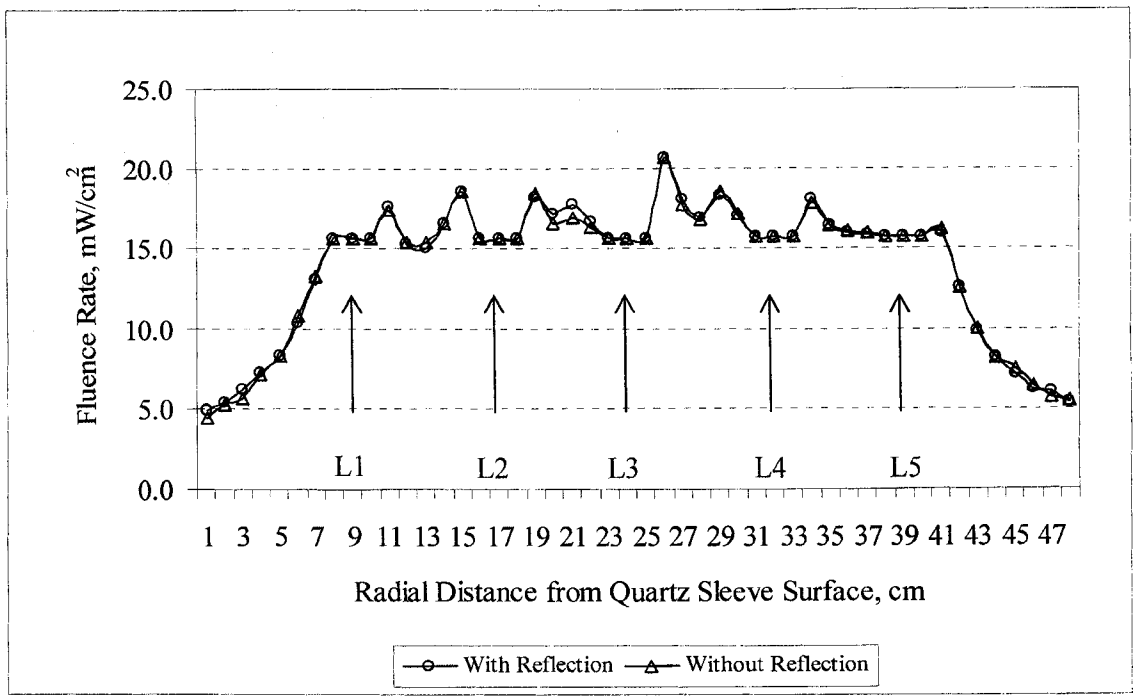

Figure 6-12. MCRT Estimated Fluence Rates for Cases With vs. Without Reflection for Five-Row System

6.4.2 Fluence Rate Distributions Between Rows of Lamps

Fluence rate profiles across the channel width in the y-direction (i.e., perpendicular to the direction of the channel) between Rows 1, 2, and 3 were estimated using MCRT model, and these fluence rate profiles, as represented by sampling lines 2 and 3 in Figure 6-11, are illustrated in Figure 6-13. The profile associated with Line x = 21 cm represents the fluence rate distribution between Rows 1 and 2, and that associated with Line x = 34 cm represents the fluence rate distribution between Rows 2 and 3. On average, the x = 21 cm profile exhibited fluence rates of 1 to 2 mW/cm^2 smaller than that of the x = 34 cm profile.

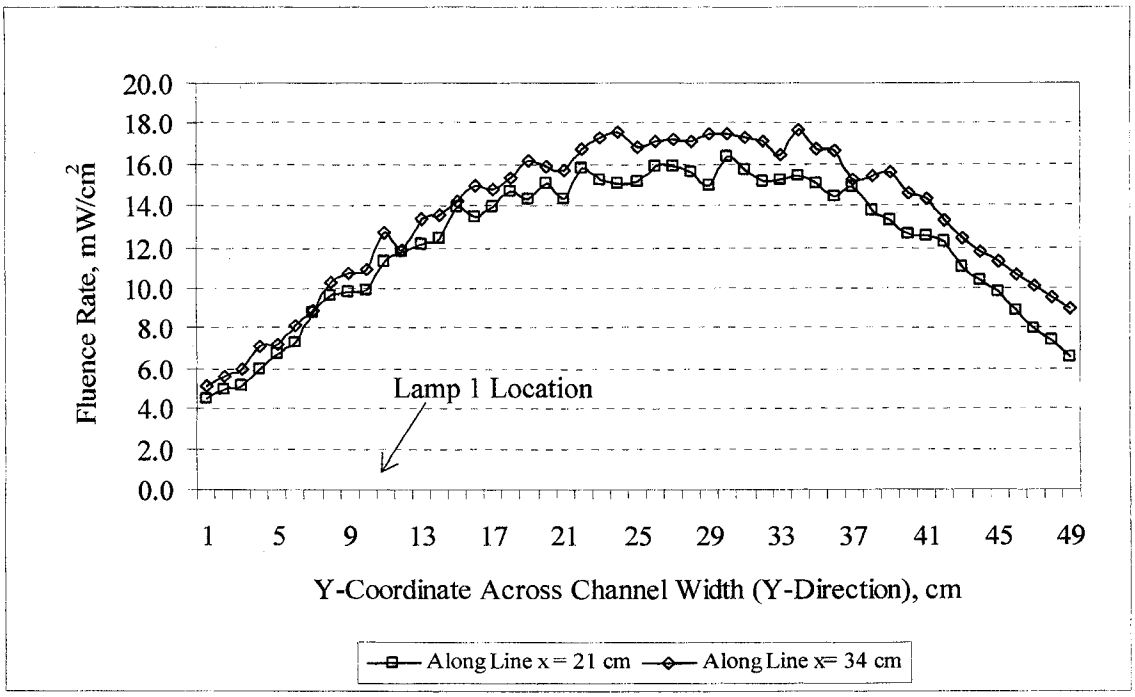

Figure 6-13. Fluence Rate Distribution Across Channel Width (Y-Direction) Between Three Rows of Lamps

Specifically, it was observed that fluence rates are highest near the center of the lamp bank in each row and steadily decrease on both sides of the lamp bank. The difference between the highest fluence rate in the center of the bank and those on one side of the bank (within a few centimeters from a quartz tube located on the side), such as Lamp 1's location shown in Figure 6-13, could be as much as 10 mW/cm^2. This is a significant difference in terms of the fluence rate.

Estimated fluence rate data shown in Figure 6-13 are listed in Table 6-9. Corresponding y-coordinates of nearby lamps are shown in the same table. The last two columns of the table list differences and percent difference relative to the lower distribution (along Line x= 21 cm between Rows 1 and 2). Negative values throughout

the columns confirmed that that fluence rates near the center area of the lamp bank are higher than those at other locations of the lamp bank. A maximum difference of 16 percent was found between the two fluence rate distributions estimated between Rows 1 and 2 and between Rows 2 and 3.

6.4.3 Fluence Rate Distributions Along the Channel Length

MCRT estimated fluence rates along the channel length (identified by Lines 4, 5, and 6 in Figure 6-11 are plotted in Figure 6-14 for the sampling lines with y-coordinates of 6 cm, 13-14 cm, and 21-22 cm, respectively. Line 4 corresponds to the profile outside the lamp bank along the sidewall of the channel and is approximately 3 cm from the quartz tube of Lamps 1, 11, and 21. Lines 5 and 6 correspond to the profile inside the lamp bank in the typically main-stream flow direction. Line 5 intersects Lamps 6 and 16, and Line 6 intersects Lamps 7 and 17.

As shown in Figure 6-14, the fluence rate profile associated with Line y = 6 cm (Line 4) exhibits the lowest fluence rates since sampling locations were outside the lamp bank, and the fluence rate profile associated with Line y = 21 - 22 cm (Sampling Line 6) exhibits the highest fluence rates.

Table 6-9. MCRT Estimated Fluence Rate Data Across Lamp Bank in Five-Row System

y-Coordinate cm	Fluence Rate (*), mW/cm^2			
	x= 21 cm	x= 34 cm	Difference	Percent Difference
1	4.47	5.12	-0.6	-12.7
2	4.95	5.60	-0.6	-11.5
3	5.19	5.94	-0.8	-12.6
4	5.98	7.10	-1.1	-15.9
5	6.69	7.18	-0.5	-6.8
6	7.29	8.10	-0.8	-10.0
7	8.79	8.86	-0.1	-0.8
8	9.62	10.27	-0.7	-6.3
9 (Lamp 1)	9.79	10.74	-1.0	-8.9
10 (Lamp 1)	9.90	10.94	-1.0	-9.5
11 (Lamp 1)	11.28	12.69	-1.4	-11.1
12 (Lamp 6)	11.82	11.84	-0.02	-0.1
13 (Lamp 6)	12.16	13.38	-1.2	-9.1
14 (Lamp 6)	12.42	13.58	-1.2	-8.6
15	13.94	14.21	-0.3	-1.9
16	13.49	14.92	-1.4	-9.6
17 (Lamp 2)	13.89	14.77	-0.9	-5.9
18 (Lamp 2)	14.69	15.28	-0.6	-3.9
19 (Lamp 2)	14.32	16.14	-1.8	-11.3
20 (Lamp 7)	15.01	15.85	-0.8	-5.3
21 (Lamp 7)	14.33	15.74	-1.4	-8.9
22 (Lamp 7)	15.79	16.75	-1.0	-5.7
23	15.26	17.25	-2.0	-11.5

(*) One Million Bundles per Lamp.

Table 6-9 (Continued)

y-Coordinate cm	Fluence Rate, mW/cm^2			
	x= 21 cm	x= 34 cm	Difference	Percent Difference
24 (Lamp 3)	15.07	17.54	-2.5	-14.1
25 (Lamp 3)	15.10	16.84	-1.7	-10.4
26 (Lamp 3)	15.87	17.12	-1.2	-7.3
27 (Lamp 8)	15.89	17.20	-1.3	-7.6
28 (Lamp 8)	15.65	17.08	-1.4	-8.4
29 (Lamp 8)	14.96	17.51	-2.6	-14.6
30	16.32	17.46	-1.1	-6.5
31	15.71	17.29	-1.6	-9.1
32 (Lamp 4)	15.09	17.12	-2.0	-11.8
33 (Lamp 4)	15.27	16.45	-1.2	-7.2
34 (Lamp 4)	15.44	17.63	-2.2	-12.4
35 (Lamp 9)	15.06	16.76	-1.7	-10.1
36 (Lamp 9)	14.41	16.63	-2.2	-13.3
37 (Lamp 9)	14.87	15.21	-0.3	-2.2
38	13.70	15.42	-1.7	-11.2
39 (Lamp 5)	13.25	15.58	-2.3	-14.9
40 (Lamp 5)	12.57	14.55	-2.0	-13.6
41 (Lamp 5)	12.53	14.32	-1.8	-12.5
42 (Lamp 10)	12.21	13.27	-1.1	-8.0
43 (Lamp 10)	11.03	12.39	-1.4	-10.9
44 (Lamp 10)	10.40	11.80	-1.4	-11.9
45	9.85	11.31	-1.5	-12.9
46	8.92	10.62	-1.7	-16.0

The fluence rate profile associated with Line y= 21-22 cm (Sampling Line 4 in Figure 6-14 exhibited a moderate range of fluence rates compared with the first two profiles, i.e., Sampling Lines 5 and 6. Both of the internal profiles show increased fluence rates near the center of the bank compared with those on the side of the bank. These results again

confirm the observations discussed in Section 6.4.2 that fluence rates are highest near the center of the lamp bank and drop steadily toward the sides of the bank.

In addition, an MCRT estimated average fluence rate of approximately 15.7 mW/cm^2 on the quartz tube surfaces associated with Lamps 6, 7, 16, and 17 was used in the Figure 6-14. The two highest lines represent the fluence rate profiles along Sampling Lines 5 and 6 across the interior space of the lamp bank. These profiles are herein referred to as the interior profiles. The highest profile (Line 6) was consistently higher than the average quartz surface fluence rate of 15.7 mW/cm^2, and the peak values in this profile at x coordinates 30 cm and 54 cm were approximately 7 mW/cm^2 to 12 mW/cm^2, respectively. This is higher than the quartz surface fluence rate. The next lowest profile associated with Line 5 showed fluence values fluctuating approximately 2 mW/cm^2 below and above the quartz tube surface fluence rate of 15.7 mW/cm^2. Peak fluence rates at x coordinates 29 cm and 54 cm were approximately 7 mW/cm^2 higher than the average quartz tube surface fluence rate. These results indicate that a higher density of bundle passes was found at the center of the lamp bank, and the density decreases toward the sides of the bank. Thus, the cummulative effects of energy contribution from the number of lamps surrounding a point in the system played a crucial role in the total fluence rate level at that point in the system.

Furthermore, unlike a single lamp system where the highest fluence rate was expected at the quartz sleeve surface, the highest fluence rate was found at locations other than the quartz sleeve surface in multiple-lamp systems (such as those at x coordinates 29 and 53 shown in Figure 6-14). It was postulated that the peaks found in the interior area

of the lamp bank might result in part from compounded reflections on the quartz surface. Further investigation of this phenomenon would be helpful in confirming such effects.

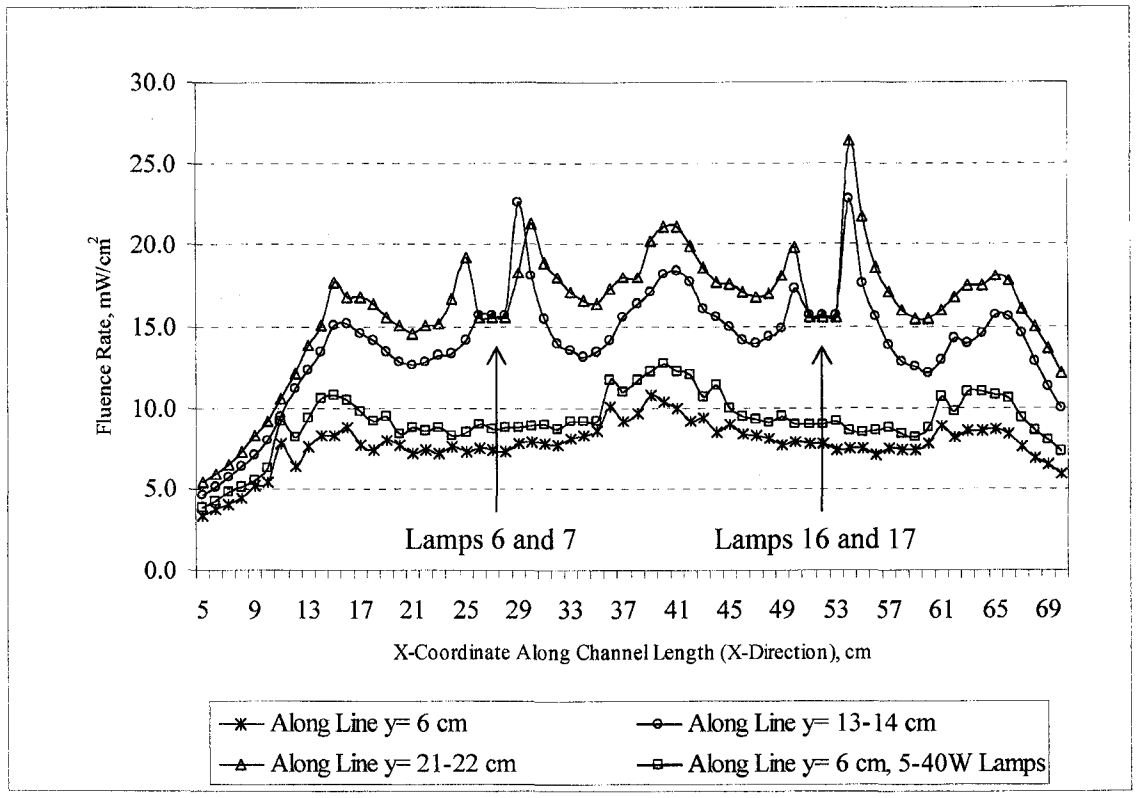

Figure 6-14. Fluence Rate Distribution Across Lamp Bank Along Channel Length (X-Direction)

Furthermore, a fluence rate profile along Line y = 6 cm in Figure 6-14 for the same five-row system in which five 26.7 W lamps on one side of the lamp bank were replaced with 40 W lamps (Lamps 1, 5, 11, 16, and 21 identified in Figure 6-11). These simulations were conducted to evaluate the potential improvement of fluence rate distribution along the sampling area of Line 4, where water travels at higher velocities compared to those inside the lamp bank; thus, UV exposure time and dose are reduced. Hence, Line 4 corresponds to the profile outside the lamp bank along the sidewall of the

channel and is approximately 3 cm from the quartz tube of Lamps 1, 11, and 21. Results of estimated fluence rates contributed by the five higher capacity ratings shown in Figure 6-14 indicate a general increase of approximately 2 mW/cm^2 in that area. Using even higher lamps along the side of the bank would result in increased fluence rates that are closer to those corresponding to the interior profiles, and it would possibly synchronize fluence rates across the channel width in the y-direction (i.e., perpendicular to the direction of the channel).

6.5 SUMMARY

Based on the results discussed in this chapter, the effect of quartz surface reflection on fluence rate distribution is considered insignificant for the two-lamp system. In the four-lamp and multiple-lamp systems, such effects potentially increase; however, further investigation and field sample measurements would be necessary in order to confirm such predictions on a proportional scale The effects of lamp shadowing in a two- lamp system were confirmed in the analysis for the two-lamp system. The effects of lamp spacing on the fluence rate distribution in the area between two adjacent lamps were significant in the two-lamp system. As the number of lamps increases, as in the four-lamp system, the lamp spacing effects decrease because fluence rates in the areas between two adjacent lamps in the four-lamp system were approximately 25 percent higher than those in the two-lamp system. Neglecting such effects in fluence rate calculations would result in an overestimate of fluence rate by 1 to 2 mW/cm^2 in the radial areas and may result in an under-design. In the multiple-row system, fluence rates were found toward the center of the lamp bank and lower toward the sides of the bank.

The difference between the higher and lower fluence rate could be significant, particularly across the width of the bank (typically orthogonal to the flow direction). In such systems, areas along the walls on both sides of the lamp bank experience the lowest fluence rates, and application of lamps with higher rated output along both sides of the lamp bank would increase fluence rates in these areas.

CHAPTER 7

SUMMARY

7.1 CONCLUSIONS

The objectives of this study were achieved by successful developing and validating the Monte Carlo Ray-Trace (MCRT) algorithm and corresponding computer codes to determine the distribution of fluence rates and related effects of reflections and lamp spacing in UV disinfection systems consist of low pressure lamps. This study was an attempt to apply the principles of radiation and the stochastic Monte Carlo method for the first time to describe overall fluence budget in various UV disinfection systems in a three-dimensional setting. The MCRT method developed in this study depends on the generation of millions of random number for each simulation. Each simulation is an independent event, and the data it generates are independent outcomes. Computer programs were developed with the ability to model distribution of fluence rates in various UV systems with lamps to a bank with multiple lamps as well as rows oriented vertically or horizontally in water, wastewater or air.

The Monte Carlo method was successfully implemented in simulating, tracing and estimating realistic multi-dimensional, multi-directional UV rays in unit of millions of light bundles. Simulated model estimates consistently indicated that meaningful fluence rate data were obtained by using the mathematical relationship and computer codes developed in this study. A large amount of simulated fluence data for the three dimensional space of the various UV system setups and designs can now be obtained

within a short period of time in a matter of minutes compared to days and weeks required by the conventional procedure that is consist of expensive, inflexible and lengthy setups and tedious yet not so accurate measurements of fluence rates. Such simulation data obtained from the MCRT model potentially provide insight into the three-dimensional distribution of fluence rates in UV systems. Moreover, such fluence rate data were not easily or technically feasible to obtain by experimental methods due to inherent limitations in reactor space and capacities of UV sensors.

According to the Ultraviolet Disinfection Guidance Manual for Final Long Term 2 Enhanced Surface Water Treatment Rule, typically, only a few UV sensors are recommended for monitoring fluence rates in actual UV systems (USEPA, 2006). Monitoring results obtained from such measurements do not represent fluence rates of the systems in actuality because sensors measure UV energies from their limited scopes of lenses and apertures. In reality UV energies are emitted and distributed in all directions in three-dimensional space. In that regard, it would be advantageous to use a simulation model such as the MCRT algorithms developed in this study to gain a better understanding of the realistic distributions of fluence rates within the system in a cost-effective way.

The MCRT model and simulation results were successfully validated using three sets of observed, experimental data provided by two independent sources. The observed experimental results were based on actinometric testing using iodide/iodate solutions to determined fluence rate in water and wastewater based on the use of a UV sensor to measure irradiance in the air. In particular, estimated MCRT fluence rates were very close to the observed experimental fluence rate data, particularly within the first few

centimeters from the quartz sleeve surface. Estimated MCRT fluence rates in the air system were slightly higher than measured irradiance data. Such estimated results for the air system were considered reasonable due to the fact the UV sensor measured UV energies within the limited scope of the lense and aperture of the device and limited direction of incoming energies, whereas the MCRT model estimated UV energies from all directions available based on the dimension of the lamp.

The MCRT model is uniquely different from all other existing UV fluence computational models. First, the current models are deterministric single-equation transfer function models that produce the same results for a set of input values, whereas the MCRT model produces slightly different results for different simulations. As described in Chapter 3, several system equations were used in developing the MCRT model. In spite of the variation in the MCRT estimated results, consistent results describing the realistic system were obtained, as demonstrated in detail in Chapters 4 and 5. It is believed that uncertainties of fluence rates exist in real UV systems; therefore, performing stochastic sampling of such systems would result in more realistic assessment of fluence rate distributions in the systems, compared with deterministic results. Second, the current existing computational models are highly limited in their ability to calculate fluence rates in three-dimensional space while simultaneously taking into account of the inherent phenomena such as reflection, refraction, and absorption. These models are also designed to handle only single lamp condition, and highly limited in their capabilities in calculating fluence rates in complex geometries involving multiple lamps and rows of lamps. The MCRT model, on the other hand, is fully capable of incorporating various systems with complex geometries effectively and efficiently. The MCRT model can be

used in a wide variety of shapes, sizes, and configuration of UV systems, thus it potentially provides the flexibility in modeling and design. In this regard, the MCRT computer programs developed in this study are able to determine fluence rates contributed by all lamps in the system from all directions; therefore provide data closer to real system conditions.

One of the objectives of this study was to use the MCRT model to evaluate potential effects of reflections from quartz sleeve surfaces and effects of lamp spacing on the distribution of fluence rates in UV systems. Representative conceptual modeled UV systems with two lamps, four lamps, and 25 lamps arranged in five rows were evaluated by the MCRT model to estimate fluence rates. Results of the evaluation indicated that effects of quartz sleeve reflection on fluence rate distributions were considered insignificant for the two-lamp system. In the four-lamp systems and multiple-lamp systems, such effects potentially increase; however, further investigation would be necessary in order to confirm such proportional relationship in quartz sleeve reflection effects. Effects of lamp shadow in a two-lamp system were confirmed in the analysis of the two-lamp system. The effects of lamp spacing on the fluence rate distribution in the area between two adjacent lamps were significant in the two-lamp system. As the number of lamps increases, as in the four-lamp system, the lamp spacing effects decrease because fluence rates in the areas between two adjacent lamps in the four-lamp system were approximately 25 percent higher than those in the two-lamp system. Neglecting such effects in fluence rate calculations would result in an overestimate of fluence rate MCRT model is a probabilistic model that describes the likelihood of system characteristic and its response with random variability in initial conditions, and that 2

mW/cm2, which is a significant difference for any analysis and design, in the radial areas under study. In the multiple-row system, higher fluence rates were found toward the center of the lamp bank and lower toward the sides of the bank. The difference between the higher and lower fluence rate could be significant, particularly across the width of the bank (and typically in the cross-flow direction). In such a system, areas along the walls on both sides of the lamp bank experience the lowest fluence rates, and application of lamps with higher rated output along both sides of the lamp bank would increase fluence rates in these areas.

7.2 RECOMMENDATIONS FOR FURTHER STUDY

As a result of this study, the following future study areas are identified. First, the MCRT model developed in this study are capable of generating useful three-dimensional data for modeled UV systems. Such data are not only related to fluence rates but also optical properties of the systems, such as transmissivities, reflectivities, and absortivities. Thus, the data could be used further to develop multicolinearities and correlations among fluence rates and optical specifications, lamps specifications, lamp orientation, and system geometries. Such correlations would be useful in developing a number of related nomographs for fluence rates without having to use the computer model.

Second, effects of the reflections may play a role in increasing fluence rates in systems with reflective surfaces such as stainless steel walls. Such a study may yield different results from those for the nonreflecting walls used in the current study and is therefore recommended.

Third, the method developed in this study can be developed for use in systems with medium pressure lamps, which emit lower percentage of UV energies in the 254 nm wavelength and energies in other wavelengths. The MCRT method is a potentially powerful tool in stochastically determining fluence rate distribution with difference wavelengths and more realistically modeling actual UV systems. Therefore, a follow up study focusing on such development is recommended.

Finally, application of the MCRT method developed in this study is potentially useful in studying fluence rate distributions in the UV disinfection of air. Current studies of such air disinfection system have been based on a radial model in which UV energies are assumed to emit in radial direction only (Kawalski, 2001). Applying the MCRT model in such systems would be helpful in providing more realistic and insightful data related to air disinfection systems in a full three-dimensional space.

REFERENCES

Blatchey III, E. R.; Wood, W. L. ; and Shuerch, P. (1995) UV Pilot Testing: Intensity Distribution and Hydrodynamics. *J. Environmental Engineering*, Vol. 121, No. 3, March 1995.

Blatchey III, Ernest R. (1997) Numerical Modeling of UV Intensity: Aplication to Collimated-Beam Reactors and Continuous-Flow Systems. *J, Water Research*, Vol. 31, No. 9, pp 2205-2218.

Bolton, J. R. (1999) Bolton Photosciences, Inc.'s Ultraviolet Applications Handbook.

Bolton, J. R. (2000) Calculation of Ultraviolet Fluence Rate Distributions in a UV Reactor. *J. Water Research*, November 1999.

Cairns, W. L. and MacDougall. (1995) Advances in UV Disinfection Technology for Treatment of Low Quality Wastewater. Paper presented at 16th Federal Convention of Australian Water & Wastewater Association, April 2 – 6, 1995, Sydney, Australia.

Chiu, K. P. (1998) Process Behavior of Vertical Ultraviolet Disinfection Systems. Ph. D. thesis, Purdue University.

Chiu, K. P.; Lyn, D. A; Savoye, P.; and Blatchey III, E. R. (1999) Integrated UV Disinfection Model Based on Particle Tracking. *J. Environmental Engineering*, Vol. 125, No. 1, January 1999.

Chiu, K. P.; Lyn, D. A; Savoye, P.; and Blatchey III, E. R. (1999) Effect of UV System Modifications on Disinfection Performance. *J. of Environmental Engineering*, Vol. 125, No. 5, May 1999.

Clancy, J. L.; Bukhari, Zia; Hargy, T. M.; Bolton, J. R.; and Dussert, Bertrand. (1998) Inactivation of Cryptosporidium parvum Oocysts Using Medium-Pressure UV Light in Bench and Pilot Scale Studies. Water Quality Technology Conference, Nov. 1 – 4, 1998, San Diego, CA.

Craik, S. A.; Amoah, K.; Smith, D. W. The Impact of Turbidity of Cryptosporidium and Giardia Inactivation by Ultraviolet Light. Proceeding of the Water Quality Technology Conference, Seattle, WA, American Water Works Association

Danielson, R.E.; Philips, J.; Soroushian, F. (2001) Inactivation of *Giadia muris*, *Bacillus subtilis* spores and MS2 coliphage by ultraviolet light. Proc. First International Congress of Ultraviolet Technologies, Washington, D. C.

Hayes, S. L.; Rice, E. W.; Ware, M. W.; Schafer, F. W. (2003) Low Pressure Ultraviolet Studies for Inactivation of *Giadia muris* cysts. *J. Applied Microbiology*, V. 94, No. 1

Hunter, G. L. *et al.* (1998) Medium-Pressure Ultraviolet Lamps and Other Systems Are Considered for Wastewater Application. Water Environment and Technology, V. 10, No. 6, p. 41.

Iranpour, R.; Garnas, G.; Moghaddam, O.; and Taebi, A. (1999) Hydraulic Effects on Ultraviolet Disinfection: Modification of Reactor Design. *J. Water Environment Research*, Vol. 71, No. 1, January/February 1999.

Irazoqui H. A., Cerda J; and Cassano, A. E. (1973) Radiation Profiles in an Empty Annular Photoreactor with a Source of Finite Spatial Dimension, *J. American Institute of Chemical Engineers*, Vol. 19, p. 460-468.

Jacob, S. M. and Franoff, J. S. (1970) Light Intensity Profiles in a Perfectly Mixed Photoreactor. *J. American Institute of Chemical Engineers*, Vol. 16, No. 3, May 1970.

Jagger, J. (1967) Introduction to Research in Ultraviolet Photobiology. Prentice-Hall, Inc., New Jersey.

Kowalski, W. J. (2001). Design and Optimization of UVGI Air Disinfection Systems, Ph. D. thesis, The Pennsylvania State University.

Loge, F. J.; Emerick, R. W.; Heath, M.; Jacangelo, J.; Tchobanoglous G.; and Darby, J. (1996) Ultraviolet Disinfection of Secondary Wastewater Effluents: Prediction of Performance and Design. *J. Water Environmet Research*, Vol. 68, No. 5, July/August 1996.

Lyn, D. A.; Chiu, K.; and Blatchey, E. R. (1999) Numerical Modeling of Flow and Disinfection in UV Disinfection Channels. J. Environmetal Engineering, Vol. 125, No. 1, January 1999.

Mahan, R. J. (2002) *Radiation Heat Transfer A Statistical Approach.* John Wiley and Sons, New York.

Modest M. F. (1993) Radiative Heat Transfer. McGraw-Hill, Inc. New York.

Oppenheimer, J. A.; Jacangelo, J. G.; Laine, J. M.; Hoaglan, J. E. (1997) Testing the Equivalency of UV Light and Chlorine for Disinfection of Wastewater to Reclamation Standards. J. Water Environment Research, Vol. 69, No. 1, Jan./Feb. 1997

Qualls, R. G. and Johnson, J. D. (1983) Bioassay and Dose Measurement in UV Disinfection. J. Applied and Environmental Microbiology, march 1983, p. 872-877.

Qualls, R. G. and Johnson, J. D. (1985) Modeling and Efficiency of Ultraviolet Disinfection Systems. *J. of Water Research*, Vol. 19, No. 8, pp. 1039-1046.

Rahn, R. O.; Bolton, R. J.; and Stefan, M. I. (2000) The Iodide/Iodate Actinometer in UV Disinfection: Characteristics and Use in the Determination of the Fluence Rate Disinfection in UV Reactors. Proc Water Quality Technology Conference, 2000, Salt Lake City, UT, published by the American Water Works Association.

Sasges, M. R.; van der Pol, A.; Voronov, A.; and Robinson, J, (2007). A Standard Method for Quantifying the Output of UV Lamps. Proc. International Congress on Ultraviolet Technologies, August 2007, Los Angeles,CA.

Siegel, R. and Howell J. (2001) Thermal Radiation Heat Transfer. 4th Edition, Taylor and Francis, New York.

Schmelling, 2000) Proc. International Congress on Ultraviolet Technologies, August 2007, Los Angeles,CA.

Sererin, B. F.; Suidan, M. T.; and Engelbrecht, R. S. (1983) Kinetic Modeling of U. V. Disinfection of Water. *J. Water Research*, Vol. 17, No. 11, pp. 1669-1678, 1983.

Stefan, M. I, Bolton, J. R. (2001) Use of the Iodite/Iodate Actinometer Togethen with Spherical Cells for Determination of the Fluence Rate Dibution in UV reactors: Validation of the Mathematical Model. Proc. First International Congress on UV Technologies, June 2001, Washington, D. C.

USEPA/600/S2-86/005, March 1986. Ultraviolet Disinfection of Wastewaters from Secondary Effluent and Combined Sewer Overflows by Karl Scheible, Maureen C. Casey, and Angelika Forndran.

USEPA 832-R-92-004, September 1992. Ultraviolet Disinfection Technology Assessment.

USEPA Ultraviolet Disinfection Guidance Manual for Final Long Term 2 Enhanced Surface Water Treatment Rule (USEPA, 2006)

White, G. C. (1999) Handbook of Chlorination and Alternative Disinfectants. Fourth Edition. John Wiley & Sons, Inc. New York, 1999.

Wolfe, R. L. (1990) Ultraviolet Disinfection of Potable Water. J. Environmental Science and Technology, Vol. 24, No. 6, 1990.

APPENDIX A

TYPICAL MONTE CARLO RAY-TRACE PROGRAM OUTPUT DATA

The following MCRT program output data were from the simulations discussed in Section 6.4.3 for the case with five 40 W lamps on one side of the lamp bank. The data represented fluence rate distribution along line y= 6 cm.

FIVE ROWS-12_06.out
WITH REFLECTION

lamp_power= 26,700.00 mW/cm2
ps_bundle= 0.02670 mW/cm2
No. of bundbles=1,000,000

row no = 1

lamp no= 1 xc(lamp)= 15.00 cm yc(lamp)= 10.00 cm

lamp no= 2 xc(lamp)= 15.00 cm yc(lamp)= 18.50 cm

lamp no= 3 xc(lamp)= 15.00 cm yc(lamp)= 27.00 cm

lamp no= 4 xc(lamp)= 15.00 cm yc(lamp)= 35.50 cm

lamp no= 5 xc(lamp)= 15.00 cm yc(lamp)= 44.00 cm

row no = 2

lamp no= 6 xc(lamp)= 27.50 cm yc(lamp)= 14.25 cm

lamp no= 7 xc(lamp)= 27.50 cm yc(lamp)= 22.75 cm

lamp no= 8 xc(lamp)= 27.50 cm yc(lamp)= 31.25 cm

lamp no= 9 xc(lamp)= 27.50 cm yc(lamp)= 39.75 cm

lamp no=10 xc(lamp)= 27.50 cm yc(lamp)= 48.25 cm

row no = 3

lamp no=11 xc(lamp)= 40.00 cm yc(lamp)= 10.00 cm

lamp no=12 xc(lamp)= 40.00 cm yc(lamp)= 18.50 cm

lamp no=13 xc(lamp)= 40.00 cm yc(lamp)= 27.00 cm

lamp no=14 xc(lamp)= 40.00cm yc(lamp)= 35.50 cm

lamp no=15 xc(lamp)= 40.00 cm yc(lamp)= 44.00 cm

row no = 4

lamp no=16 xc(lamp)= 52.50 cm yc(lamp)= 14.25 cm

lamp no=17 xc(lamp)= 52.50 cm yc(lamp)= 22.75 cm

lamp no=18 xc(lamp)= 52.50 cm yc(lamp)= 31.25 cm

lamp no=19 xc(lamp)= 52.50 cm yc(lamp)= 39.75 cm

lamp no=20 xc(lamp)= 52.50 cm yc(lamp)= 48.25 cm

row no = 5

lamp no=21 xc(lamp)= 65.00 cm yc(lamp)= 10.00 m

lamp no=22 xc(lamp)= 65.00 cm yc(lamp)= 18.50 cm

lamp no=23 xc(lamp)= 65.00 cm yc(lamp)= 27.00 cm

lamp no=24 xc(lamp)= 65.00 cm yc(lamp)= 35.50 m

lamp no=25 xc(lamp)= 65.00 cm yc(lamp)= 44.00 cm

ps 0.0400
ps 0.0267
ps 0.0267
ps 0.0267
ps 0.0267
ps 0.0400
ps 0.0267
ps 0.0267
ps 0.0267
ps 0.0267
ps 0.0400
ps 0.0267
ps 0.0267
ps 0.0267
ps 0.0267
ps 0.0400
ps 0.0267
ps 0.0267
ps 0.0267
ps 0.0267
ps 0.0400
ps 0.0267
ps 0.0267
ps 0.0267
ps 0.0267
nlamp 1
fr_avg on each quartz= 23.62 mW/cm2
fr_avg among the lamps= 23.62 mW/cm2

nlamp 2
fr_avg on each quartz= 15.66 mW/cm2
fr_avg among the lamps= 19.64 mW/cm2

nlamp 3
fr_avg on each quartz= 15.39 mW/cm2
fr_avg among the lamps= 18.22 mW/cm2

nlamp 4
fr_avg on each quartz= 16.08 mW/cm2
fr_avg among the lamps= 17.69 mW/cm2

nlamp 5
fr_avg on each quartz= 16.31 mW/cm2
fr_avg among the lamps= 17.41 mW/cm2

nlamp 6
fr_avg on each quartz= 23.27 mW/cm2
fr_avg among the lamps= 18.39 mW/cm2

nlamp 7
fr_avg on each quartz= 16.01 mW/cm2
fr_avg among the lamps= 18.05 mW/cm2

nlamp 8
fr_avg on each quartz= 16.26 mW/cm2
fr_avg among the lamps= 17.83 mW/cm2

nlamp 9
fr_avg on each quartz= 15.47 mW/cm2
fr_avg among the lamps= 17.56 mW/cm2

nlamp 10
fr_avg on each quartz= 15.30 mW/cm2
fr_avg among the lamps= 17.34 mW/cm2

nlamp 11
fr_avg on each quartz= 23.77 mW/cm2
fr_avg among the lamps= 17.92 mW/cm2

nlamp 12
fr_avg on each quartz= 15.87 mW/cm2
fr_avg among the lamps= 17.75 mW/cm2

nlamp 13
fr_avg on each quartz= 15.49 mW/cm2
fr_avg among the lamps= 17.58 mW/cm2

nlamp 14
fr_avg on each quartz= 15.78 mW/cm2
fr_avg among the lamps= 17.45 mW/cm2

nlamp 15
fr_avg on each quartz= 15.54 mW/cm2
fr_avg among the lamps= 17.32 mW/cm2

nlamp 16
fr_avg on each quartz= 24.48 mW/cm2
fr_avg among the lamps= 17.77 mW/cm2

nlamp 17
fr_avg on each quartz= 16.03 mW/cm2
fr_avg among the lamps= 17.67 mW/cm2

nlamp 18
fr_avg on each quartz= 16.32 mW/cm2
fr_avg among the lamps= 17.59 mW/cm2

nlamp 19
fr_avg on each quartz= 15.50 mW/cm2
fr_avg among the lamps= 17.48 mW/cm2

nlamp 20
fr_avg on each quartz= 15.46 mW/cm2
fr_avg among the lamps= 17.38 mW/cm2

nlamp 21
fr_avg on each quartz= 22.80 mW/cm2
fr_avg among the lamps= 17.64 mW/cm2

nlamp 22
fr_avg on each quartz= 15.24 mW/cm2
fr_avg among the lamps= 17.53 mW/cm2

nlamp 23
fr_avg on each quartz= 15.70 mW/cm2
fr_avg among the lamps= 17.45 mW/cm2

nlamp 24
fr_avg on each quartz= 15.73 mW/cm2
fr_avg among the lamps= 17.38 mW/cm2

nlamp 25
fr_avg on each quartz= 15.22 mW/cm2
fr_avg among the lamps= 17.29 mW/cm2

Fluence Rate Data, mW/cm2 (i= x, j = y, k= z)

i	5	j	6	k	50	3.783
i	6	j	6	k	50	4.288
i	7	j	6	k	50	4.647
i	8	j	6	k	50	4.912
i	9	j	6	k	50	5.567
i	10	j	6	k	50	6.357
i	11	j	6	k	50	9.405
i	12	j	6	k	50	7.804
i	13	j	6	k	50	8.809

i	14	j	6	k	50	10.697
i	15	j	6	k	50	10.668
i	16	j	6	k	50	10.819
i	17	j	6	k	50	9.853
i	18	j	6	k	50	9.484
i	19	j	6	k	50	9.607
i	20	j	6	k	50	8.467
i	21	j	6	k	50	8.850
i	22	j	6	k	50	8.773
i	23	j	6	k	50	8.897
i	24	j	6	k	50	8.450
i	25	j	6	k	50	8.176
i	26	j	6	k	50	8.773
i	27	j	6	k	50	8.452
i	28	j	6	k	50	8.421
i	29	j	6	k	50	8.944
i	30	j	6	k	50	8.981
i	31	j	6	k	50	9.402
i	32	j	6	k	50	8.763
i	33	j	6	k	50	9.191
i	34	j	6	k	50	9.594
i	35	j	6	k	50	9.195
i	36	j	6	k	50	11.725
i	37	j	6	k	50	11.475
i	38	j	6	k	50	11.960
i	39	j	6	k	50	12.504
i	40	j	6	k	50	12.732
i	41	j	6	k	50	12.159
i	42	j	6	k	50	12.245
i	43	j	6	k	50	10.998
i	44	j	6	k	50	11.445
i	45	j	6	k	50	9.958
i	46	j	6	k	50	9.394
i	47	j	6	k	50	9.220
i	48	j	6	k	50	8.870
i	49	j	6	k	50	9.327
i	50	j	6	k	50	8.897
i	51	j	6	k	50	8.965
i	52	j	6	k	50	9.252
i	53	j	6	k	50	8.948
i	54	j	6	k	50	8.988
i	55	j	6	k	50	8.409
i	56	j	6	k	50	8.758
i	57	j	6	k	50	9.012
i	58	j	6	k	50	8.537
i	59	j	6	k	50	8.041

i	60	j	6	k	50	8.411
i	61	j	6	k	50	10.689
i	62	j	6	k	50	9.954
i	63	j	6	k	50	11.026
i	64	j	6	k	50	10.677
i	65	j	6	k	50	10.806
i	66	j	6	k	50	10.331
i	67	j	6	k	50	9.013
i	68	j	6	k	50	8.551
i	69	j	6	k	50	7.864
i	70	j	6	k	50	7.390

VITA

For

Khoi Trung Nguyen

DEGREES:

Doctor of Philosophy (Environmental Engineering), Old Dominion University, Norfolk, Virginia, December 2007.

Master of Engineering (Civil Engineering), Old Dominion University, Norfolk, Virginia, May 1995.

Bachelor of Science (Chemical and Civil Engineering), Virginia Polytechnic Institute and State University, Blacksburg, Virginia, May 1990.

REGISTRATION:

Professional engineer with the State of Virginia, since 1995.

PROFESSIONAL EXPERIENCE:

Over 17 years of experience as an environmental and civil engineer with different consulting firms and government agencies.